Smartphone-based solutions for continuous and accessible healthcare

Firmin Kateu

THÈSE

En vue de l'obtention du

DOCTORAT DE L'UNIVERSITÉ DE TOULOUSE

Délivré par :

Institut National Polytechnique de Toulouse (Toulouse INP)

Discipline ou spécialité :

Informatique et Télécommunication

Présentée et soutenue par :

M. FIRMIN KATEU

le jeudi 23 novembre 2023

Titre :

Des solutions basées sur les smartphones pour des soins de santé accessibles et en continus

---

Ecole doctorale :

Mathématiques, Informatique, Télécommunications de Toulouse (MITT)

Unité de recherche :

Institut de Recherche en Informatique de Toulouse (IRIT)

Directeurs de Thèse :

M. GENTIAN JAKLLARI

M. EMMANUEL CHAPUT

Rapporteurs :

M. HERVE RIVANO, INSA LYON

MME VALERIA LOSCRI, INRIA VILLENEUVE D'ASCQ

Membres du jury :

MME ISABELLE GUERIN LASSOUS, UNIVERSITE LYON 1, Présidente

M. ANDRZEJ DUDA, INP GRENOBLE, Membre

M. EMMANUEL CHAPUT, TOULOUSE INP, Membre

M. GENTIAN JAKLLARI, TOULOUSE INP, Membre

A ma famille

Remerciements

Je tiens à exprimer ma profonde gratitude envers mon directeur de thèse, Gentian Jakllari, et mon co-directeur, Emmanuel Chaput, pour leur mentorat inestimable. Travailler à leurs côtés a été une expérience enrichissante, tant sur le plan personnel que professionnel. Mes remerciements les plus sincères vont également à Bernabé Batchakui, Alain Tchana, Thomas Djotio et Thomas Bouetou de l'École Nationale Supérieure Polytechnique de Yaoundé, dont le soutien a été déterminant pour cette thèse.

Je souhaite adresser un remerciement particulier aux membres du jury pour leur expertise lors de la soutenance. Ma reconnaissance va à Valéria Loscri, Hervé Rivano, Isabelle Guérin Lassous et Andrzej Duda pour leurs remarques et échanges précieux, contribuant ainsi à l'amélioration de cette version finale du manuscrit.

À tous les membres de l'équipe RMESS, permanents et doctorants, je suis reconnaissant pour votre accueil chaleureux, votre implication dans ces travaux, nos échanges constructifs et vos précieux conseils.

Un hommage tout particulier à ceux qui m'ont accueilli en France et m'ont aidé dans mon intégration à la recherche et à la vie toulousaine, notamment Kevin Jiokeng, Boris Wembe, Boris Teabe et Djob Mvondo.

Je tiens également à remercier les étudiants de l'ENSEEIHT qui ont joué un rôle essentiel dans les expérimentations de ce travail.

Enfin, un immense merci à mes amis de la promotion Génie Informatique 2019 de l'École Nationale Supérieure Polytechnique de Yaoundé. Votre soutien moral et vos partages d'expériences ont été inestimables. À la GI 2019, je vous adresse toute ma gratitude.

Abstract

Vital to human life, healthcare remains costly, administered by a complex and insular apparatus, and often out of reach for many. However, the omnipresent and technologically advanced smartphones offer a transformative opportunity. They can now place advanced diagnosing and health monitoring capabilities in people's hands, marking a paradigm shift in healthcare. By leveraging the capabilities and widespread use of smartphones, we envision two disruptive roles for the healthcare system. First, smartphone-based solutions can enable continuous health monitoring, reducing the reliance on individual subjective experiences to detect anomalies. Second, the smartphone provides an ideal platform for developing low-cost medical technologies, making healthcare more accessible, especially in regions with limited infrastructure.

The field of research known as "mobile health" (mHealth) comes closest to our vision. It involves using connected mobile devices to provide health-related services, such as measuring vital signs, conducting screening exams, and performing tests on samples, previously carried out only in laboratories settings. However, despite significant enthusiasm from the community over the past decade, existing solutions fall short of realizing our aspirations. Many rely on expensive hardware, intricate configurations and protocols, or demand specialized expertise, hindering widespread adoption, especially by untrained individuals with limited resources outside laboratory settings.

Against this background, in this thesis we introduce a methodology that combines well-established mathematical principles describing natural phenomena, signal and image processing techniques, and machine learning algorithms within a data-driven design framework. The objective is to foster the development of mobile health (mHealth) systems that can deliver on our vision. We demonstrate this methodology through three smartphone-based solutions – SmartPhOx, BandS-Spi, Droplets– each enabling either the measurement of a vital sign (blood oxygen level), the performance of a medical examination (spirometry), or the easy testing of a liquid sample.

Specifically, SmartPhOx introduces a pure camera-and-flashlight smartphone-based pulse oximetry oximetry system, founded on the principles of the Beer-Lambert law, meeting the accuracy threshold required for FDA clearance. BandS-Spi builds upon the Boyle–Mariotte law and enables a user to conduct spirometry tests using a smartphone and an inflatable balloon. The accuracy achieved is comparable to that of tests performed in the presence of a clinician equipped with specialized equipment. Lastly, Droplets, drawing on the Young-Laplace equation, offers a solution for analyzing a liquid using a single droplet. Its accuracy allows for the detection of protein level variations in urine enabling the identification of suspected cases of proteinuria using the camera of any smartphone.

Keywords : Mobile Health, mHealth, Pervasive Healthcare, Continuous Healthcare, Humane-Centered Computing, Mobile Computing.

Résumé

Les avancées de la médecine au cours de ces dernières décennies ont conduit à un système de santé toujours plus spécialisé et cloisonné. L'accès aux soins, quoi que fondamental pour la vie humaine, est souvent complexe voire hors de portée pour de nombreuses personnes. Paradoxalement, l'utilisation de smartphones aux technologies de plus en plus avancées s'est au contraire très largement démocratisée. Leurs capteurs toujours plus variés et leur puissance nous incitent à imaginer deux changements de paradigme dans le suivi médical. D'une part des solutions fondées sur les smartphones peuvent permettre une surveillance continue de la santé, réduisant les biais induits par le caractère subjectif de l'expérience individuelle dans la détection des symptômes. D'autre part le smartphone constitue une plateforme idéale pour développer des technologies médicales à faible coût, rendant les soins plus accessibles, en particulier dans les régions où les infrastructures sont limitées.

Cette vision s'insère dans le domaine de recherche de la "santé mobile" (mHealth) qui vise à utiliser des appareils mobiles connectés pour fournir des services liés à la santé tels que la mesure des signes vitaux, des examens de dépistage ou des analyses d'échantillons, auparavant effectués uniquement en laboratoire. Pourtant, malgré l'enthousiasme de la communauté scientifique, les résultats ne sont pas à la hauteur des attentes. De nombreuses solutions reposent en effet sur du matériel coûteux ou des protocoles complexes, ou encore exigent une expertise spécialisée, ce qui entrave leur adoption à grande échelle.

Dans ce contexte, nous introduisons dans cette thèse une méthodologie qui combine des principes mathématiques bien établis décrivant des phénomènes naturels, des techniques de traitement des signaux et des images, et des algorithmes d'apprentissage automatique. Notre objectif est de développer des systèmes de santé mobile (mHealth) conformes à notre vision. Nous appliquons cette méthodologie au travers de la conception de trois applications pour smartphone : SmartPhOx, BandS-Spi et Droplets. Elles permettent respectivement la mesure d'un signal vital (le niveau d'oxygène dans le sang), la réalisation d'un examen (spirométrie) et l'analyse simple d'un échantillon de liquide.

Plus précisément, SmartPhOx propose un système d'oxymétrie fondé sur l'appareil photo et le flash du téléphone, en s'appuyant sur la loi de Beer-Lambert. Ce système atteint le seuil de précision requis pour obtenir l'autorisation de la FDA. BandS-Spi s'appuie sur la loi de Boyle-Mariotte et permet à un utilisateur de réaliser des tests de spirométrie à l'aide d'un smartphone et d'un ballon gonflable. La précision obtenue est comparable à celle des tests effectués sous le contrôle d'un clinicien, équipé d'un matériel spécialisé.Enfin, Droplets, s'appuyant sur l'équation de Young-Laplace, offre une solution pour analyser un liquide à partir d'une seule gouttelette. Sa précision permet de détecter les variations du taux de protéines dans l'urine, rendant possible l'identification de cas suspects de protéinurie à l'aide de l'appareil photo de n'importe quel smartphone.

Mots clés : Santé Mobile, Informatique Ubiquitaire, Informatique Centrée sur l'Homme, Soins de Santé en Continue, Santé ubiquitaire.

Table of contents

List of Figures

List of Tables

Introduction

"... A vast majority of Covid pneumonia patients I met had remarkably low oxygen saturations at triage — seemingly incompatible with life — but they were using their cellphones as we put them on monitors." [1]

What if their cellphones could have measured their oxygen saturation, how many of these patients would have avoided intubation ?

...more broadly, what if the very cellphone already owned could serve as medical device, how easily human being would have access to healthcare ?

1.1 Evolution of the health care system

The healthcare system has greatly evolved over time in many ways. We have come a long way from trial-and-error medicine in the Middle Ages to a well-organized journey in our current era, ***starting with*** the patient feelling ill, visiting the doctor. With the aid of scientific knowledge and technical tools at their disposal, the doctor examines the patient, makes a diagnosis, and provides treatment using appropriate equipments. Almost every phase of the healthcare process has seen significant improvements thanks to technology.

— Previously, diagnoses were mainly based on the doctor's observation and interpretation of symptoms. Nowadays, diagnoses rely on advanced technologies such as magnetic resonance imaging, computed tomography scans, or genetic tests.

— In the past, patient monitoring required the doctor to visit the patient's home. Today, we are witnessing the rise of remote monitoring, based on portable medical devices designed for home use and the democratization of communication technologies.

— The same goes for medical equipment. Before the 18th century, surgeons used stone knives for incisions during surgery and a hot iron to burn tissues to seal blood vessels or remove tumors. Nowadays, we use more modern tools such as stainless steel scalpels and electric scalpels.

*Nevertheless, **the starting point** of the healthcare system is the only aspect that has not witnessed any improvement ever.* In simpler terms, patients are still responsible for detecting any health anomalies to kickstart their healthcare journey.

Unfortunately, patients may not always realize they are ill or may notice it late. A notable example is the cases of silent hypoxia during the COVID-19 pandemic [1]. Some patients with COVID-19 were found to have severe hypoxia – abnormally low blood oxygen levels – when they arrived at the hospital. Unlike other respiratory distress situations where the drop in blood oxygen levels alarms the patient and triggers healthcare intervention, COVID-19-induced hypoxia often goes unnoticed. As a result, patients arrive at the

1. https ://www.nytimes.com/2020/04/20/opinion/sunday/coronavirus-testing-pneumonia.html

emergency unit much later and in a more severe state, requiring intensive care. This issue is illustrated in anecdotal comments reported by a doctor in a New York Times article[1]. From a bigger perspective, tardy disease detection is estimated to be one of the leading causes of death worldwide [2-5], presenting a significant challenge in our society.

The question that naturally arises, when reading this doctor's comment, is *what would have happened to this patient if the very smartphone she was using was capable of detecting the deterioration of her health condition ?*

1.2 The Evolution of Smartphones : Shaping Our Everyday Lives

The smartphone is an advanced and innovative instrument that has transformed our lifestyles. It has come a long way, assuming increasingly pivotal roles in our lives and showing no signs of slowing down.

1.2.1 From phone to mobile phone

It all began with the invention of the telephone by Graham Bell in 1876, revolutionizing long-distance communication. In 1973, Motorola took a step further towards accessibility by introducing the first portable phone, the Motorola DynaTAC 8000X. Weighing nearly 800 grams, measuring 25 cm, and priced around 4000 USD, it was initially reserved for cars and professionals. However, advancements in technology led to its miniaturization and subsequent democratization, with ownership rates skyrocketing from 4% to 47% among the French population between 1997 and 2000. By 2019, an astonishing 95% of the population owned a mobile phone [6], marking the beginning of the democratization of telecommunications in our contemporary era.

1.2.2 From Mobile Phone to Smartphones : A Revolutionary Leap

« Today Apple is going to reinvent the phone... » [2]

Thanks to the great technological advances of the last few decades, notably the invention of computers and the development of networks, mobile phones are becoming multitasking. Functions such as messaging, media handling introduced in 2003 with the BlackBerry Quark [7], and even photography, initiated in 1999 with the introduction of the camera in the device for the first time, are appearing. What marked a major turning point in the explosion of services offered by the device was the re-introduction [3] of the touchscreen and the first sensors (Gyroscope sensor), launched by Apple in 2007 with the IPhone[2]. Since then, more and more sensors have been integrated by manufacturers, around which algorithms are designed to offer various services. Their appellation has changed to "smart phone" or a smartphone for simplicity [4]. They combine the functions

2. Steve Jobs, introducing iPhone in 2007.
3. The first mobile phone with a touchscreen was the IBM SImons, appeared in 1992.
4. We will use both terms interchangeably throughout the document.

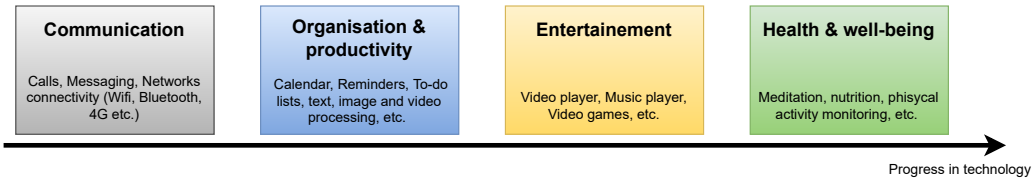

FIGURE 1.1 – An overview of smartphone use today.

of a computer, by embedding computing power and providing internet access, and that of a phone, with calls and messaging, which explains their widespread adoption among world population. For instance, in 2019, there is 6.25 billion smartphone users, which is 79.34% of the world's population [6]. The observation is the same when we focus on developing countries. In Africa, for example, the penetration rate was 30% in 2016 and was predicted to almost double in 2020 [8]. Thanks to their network connectivity, they allow users easy access to information. Through their computing power, they make diverse applications requiring complex calculations accessible to the user. It can be said that today, thanks to the smartphone, we are witnessing to both democratization of information and processing capability.

Based on its hardware, the services offered by the smartphone nowadays can be grouped as follows :

1. ***Communication :*** *Applications facilitating messaging, calls, and internet connectivity have transformed how we access information, use social networks, and stay connected with friends, family, and colleagues.*

2. ***Organization and Productivity :*** *Equipped with calendars, alarms, reminders, and productivity applications like office suites and project management tools, smartphones assist users in planning and optimizing their daily activities.*

3. ***Entertainment :*** *Gaming, music, video streaming, and reading applications offer diverse sources of entertainment on smartphones.*

Health and well-being More recently, there has been particular enthusiasm for the use of smartphones for health-related purposes. While the earliest of these applications focused on wellness (meditation, nutrition, physical activity monitoring, etc.), a lot of work is being done today in the scientific community, on the development of purely medical solutions based on the sensors and computing power of the smartphone, once again expanding the types of services offered by the device[9-13]. This trend is also expressed by smartphone manufacturers, since some early smartphones already incorporate sensors for purely medical purposes, such as the Galaxy S9, released by Samsung in 2018, equipped with a blood oxygen level sensor. Figure 1.1 presents an overview of the uses of the smartphone.

1.3 Toward continuous and accessible healthcare

After the democratization of communication, processing capabilities, and information, we believe that the next major evolution in smartphone usage will be centered around the democratization of healthcare. Our vision is that, being owned by a large majority of the global population [6, 8], smartphones can play a dual disruptive role in healthcare systems. In developed countries, smartphone-based solutions can enable continuous health monitoring and shift the burden of anomaly detection away from subjective individual feelings. In developing countries, smartphones provide an ideal platform for the development of medical technologies, making them more accessible to the population, especially in areas where infrastructure may be limited [14].

The research area that comes closest to this vision is mHealth or mobile health. This refers to the use of connected mobile devices to deliver health-related services. While it includes smartphones, tablets and other wearables, we will restrict the usage of this term around the smartphone throughout this document.

Specifically, existing mHealth systems in the literature can be organized into three main categories based on their objectives.

— ***Vital sign monitoring*** Smartphone-based systems have been developed to measure physiological information, providing real-time data on vital signs for disease monitoring and early anomaly detection. These systems encompass a wide range of measurements, including heart rate [15], blood oxygen level [9], blood pressure [13], glucose level [16], hemoglobin level [11], and more. Such monitoring is particularly valuable for patients with chronic diseases, facilitating remote patient care and continuous monitoring even within the comfort of their homes.

— ***Disease screening*** The focus of this category is to develop solutions for testing and monitoring specific health conditions using smartphones. Examples include assessing sleep apnea [17], atrial fibrillation [18], depression [19], traumatic brain injuries [20], Parkinson's disease [21], and other conditions. By leveraging smartphones, these solutions aim to democratize medical screening, making it more affordable and accessible. This has the potential to significantly impact healthcare in low income areas, where access to specialized screening facilities may be limited.

— ***Home testing*** This category involves the development of smartphone-based solutions that enable testing on samples traditionally processed in laboratory settings. Systems have been designed to analyze blood [22], urine [23], beverages [24], and even meals [25]. By bringing testing capabilities into the home, these solutions offer convenience and accessibility, eliminating the need for specialized laboratory equipment and reducing the time and cost associated with traditional testing methods.

Although there is growing interest in this area of research, we are still a long way from achieving our vision, for three main reasons :

— *Limited accessibility :* Existing systems often rely on specialized hardware, which makes them less accessible. Especially, some solutions require modifications to the

device itself to remove physical limitations [9], while others involve expensive external sensors that many people cannot afford [26]. This restricts their accessibility to a large part of the population, especially those with low-end devices and limited resources.

— *Lack of autonomy :* Many studies, particularly in the fields of disease screening and home testing, simply provide the test tool on a smartphone, but still require the expertise of a clinician to use it on the patient [27]. As a result, they fail to empower the user and limit the system's impact on the democratization of healthcare on a larger scale.

— *Prohibitive usage protocol :* Ideally, for a significant impact on the initial stage of the healthcare journey (as mentioned in Section 1.1), systems should work passively or with minimal user interaction. However, most existing systems require active user participation, or worse, complex and impractical operating protocols, which compromise user comfort [28]. This discourages users and hampers widespread adoption.

Given theses limitations, our objective in this thesis is to provide a method for building mHealth system in line with our vision for continuous and accessible healthcare. To accomplish this, we focus on solutions that can **fully operate on a standard smartphone**, making use of widely available sensors. We prioritize the development of a **user-friendly operating protocol** and providing comprehensive guidance to ensure **correct and reliable usage** for **the average user** within **their daily surroundings**.

1.4 Contributions and Plan

Throughout this manuscript, we present several contributions at various levels. First, we present a high-level overview of mHealth sensing (Chapter 2). Specifically, we describe the smartphone and its capabilities (Section 2.1), the challenges associated with designing a mHealth system (Section 2.2), and the architectures suited to face theses challenges (Section 2.2). We also briefly discuss existing mHealth sensing approaches (Section 2.4) and relevant data processing methods (Section 2.5).

Based on this introduction, we then present a methodology for designing an mHealth system tailored to a specific problem (Chapter 3). This methodology is designed to align with our vision by highlighting the steps and important selection criteria to consider throughout the process, aiming to achieve a system that meets our objectives as much as possible. Lastly, we illustrate the methodology with three use cases, each focusing on one of the previously mentioned categories of mHealth solutions :

— **Problem 1 :** ***Measuring oxygen levels in the blood,*** crucial for remote monitoring of cardiovascular and respiratory disease, both being part of the top three leading cause of death [6].

— **Problem 2 :** ***Estimating lung function through spirometry test,*** crucial for the handling of respiratory disease, the third world leading cause of death [6].

— **Problem 3 : *Enabling ubiquitous liquid testing,*** offering wide range of application such as body fluid testing like urine, and food liquid product testing.

Each time, we build a complete system that enables anyone, even without technical expertise, to use their smartphone for the specific task. To accomplish this, we simplify the protocols as much as possible and minimize the need for additional hardware, which may not be readily accessible. Additionally, we develop algorithms to overcome hardware limitations and address challenges related to non-expert users and unpredictable testing environments.

We present each of these illustrative applications in the following three chapters :

In chapter 3, we address the first problem, related to vital signs measurement. Following our methodology, we adopt a proven approach based on the device's camera, combining Photoplethysmography [5] with the Beer-Lambertlaw model [29] to measure SpO2. After implementing, conducting meticulous experiments, and carefully analyzing the results obtained from this approach, we uncover significant limitations. These limitations serve as the catalyst for the design of our solution : SmartPhOx. Evaluating SmartPhOx with 34 volunteers demonstrates its accuracy in measuring SpO2 using a standard smartphone's camera and flash, meeting FDA standards [30].

In chapter 4, we delve into the second problem, belonging to the category of disease screening. When developing a home-based medical examination tool, it is crucial to ensure robustness against user's inexperience and the noise associated with the testing environment. Due to these constraints, our thorough literature review does not identify any relevant existing approaches. As a result, we embark on designing a novel mHealth sensing approach, leveraging a sensor that has been seldom used. Specifically, we propose utilizing the smartphone's pressure sensor and a cheap inflatable balloon to create a setup that enables users to estimate the volume and velocity of exhaled gas during a forced expiration. Based on the insights gained from our experiments, we construct a processing pipeline and a virtual coach. These components ensure control over the user's effort quality during the maneuver and provide accurate results. Through the evaluation of our system BandS-Spi, we demonstrate its precision equivalent to clinical spirometers [6].

In chapter 5 We focus on the third problem, which involves home medical testing. To design our liquid analysis solution, we once again adopt a novel approach, based on the camera. Our system, called Droplet, distinguishes liquid droplets based on their shape. To implement this solution, we develop a setup and leverage the theory of the shape of a

5. Photoplethysmography is a computer vision technique used to measure changes in blood volume in human skin by analyzing color variations. We discuss it in details in Chapter 2.4.3

6. A spirometer is the most commonly used pulmonary function testing clinical device.

sessile droplet [31, 32]. Additionally, we create a virtual assistant to guide users in capturing reliable pictures of the droplets. These pictures are then processed using customized algorithms to estimate the capillary length and contact angle of the droplet with the surface, ultimately enabling their classification. Through this system, we demonstrate the feasibility of monitoring protein levels in urine as they transition from a healthy range to a dangerous level.

Chapter 2

An Overview of Mobile Health Sensing

In this chapter, we start by discussing the technical capabilities of regular smartphones, which are essential for mHealth (Section 2.1). Then, we introduce the overall architecture of mHealth systems (Section 2.3) and talk about the challenges involved in designing such systems (Section 2.2). We also explore the sensing techniques (Section 2.4) and data processing methods (Section 2.5) used in existing systems. This chapter lays the groundwork for introducing our methodology in Chapter 3.

2.1 Smartphone capabilities

As mentioned in Section 1.2, smartphones possess technical attributes that enable interaction, data collection, and processing of diverse information from the surroundings. In this section, we will delve into these particular capabilities of smartphones that serve as the fundamental basis for any mHealth system.

2.1.1 Sensing and acting in the physical world

The ability of smartphones to calculate a user's health information primarily stems from their sensors. Modern smartphones are equipped with a diverse sensors, each with a specific function. They can be broadly categorized as :

1. **Standard sensors :** These are the most commonly found sensors in smartphones, including motion sensors such as accelerometer and gyroscope, position sensors such as proximity and magnetic field sensors, environment sensors such as ambient light and temperature sensors, and location sensors like GPS and others.
2. **Multimedia sensors :** These are mainly the camera and microphone, which enable the device to record sound and images. mHealth systems can use them to measure such information in the environment.
3. **Radio sensors :** The phone has various sensors enabling it to communicate wirelessly with other devices. These include Wi-Fi, Bluetooth and 3G/4G/5G interfaces. Since these technologies rely on the transmission and reception of electromagnetic waves, they can be leveraged by mHealth systems to obtain an indirect measure of the environment, notably by looking at how the signal is modified. We discuss this sensing technique more in details in Section 2.4.4.
4. **Specialized sensors :** Some smartphones come equipped with specialized sensors like fingerprint, depth, heart rate and infrared sensors. Less common, theses sensors are often included to bring new features to the devices, for marketing differentiation.

In addition to its sensing capabilities, the smartphone is equipped with actuators that enable it to modify the environment. Actuators are components that convert electrical signals into physical actions or responses, allowing smartphones to interact with users and the surrounding world. These include :

- **Display :** The smartphone's display is primarily responsible for presenting visual information to the user. However, it can also be utilized as a light source by the mHealth system [33].
- **Vibration motor :** The vibration motor generates vibrations or haptic feedback in response to specific events or user interactions. It is commonly used for notifications, alerts, alarms, touch interactions, and gaming. In mHealth systems, the vibration motor can be leveraged to generate motion in the environment. For example, it has been employed to generate capillary waves on the surface of a liquid in a container, enabling the tracking of surface tension using computer vision techniques [23] (discussed in Section 2.4.3).

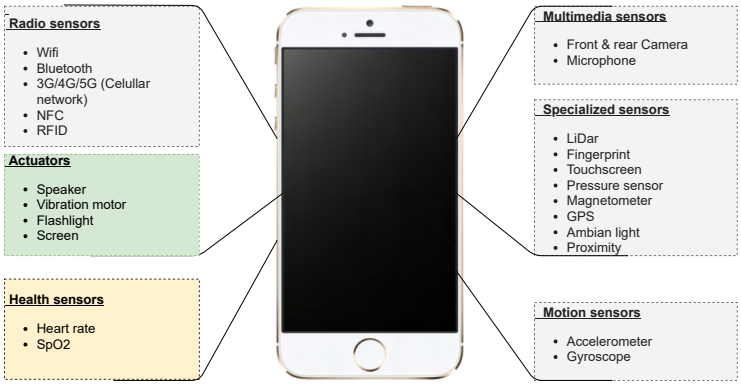

FIGURE 2.1 – Built-in sensors and actuators in a typical present-day smartphone. Note that those in yellow box are equipped in very few devices.

— **Speaker :** The smartphone's speaker produces sound output for various purposes, such as phone calls, media playback, and system sounds. It is often utilized in mHealth systems based on acoustic motion tracking, which involves analyzing echo wave sounds to track the displacement of an object. Further details on this technique can be found in Section 2.4.2.2.

— **LED flash :** Many smartphones have an LED flash located next to the camera, serving as a flashlight or providing additional lighting in low-light conditions for capturing photos or videos. In mHealth systems, the LED flash can be used as a light source, particularly for certain computer vision sensing techniques discussed in Section 2.4.3.

These smartphone actuators, in conjunction with the sensors, contribute to providing an immersive and interactive user experience. However, in the context of mHealth sensing, the objective is to repurpose these tools from their primary functions to measure specific medical information. The choice of sensor depends on the type of raw data required and the method of measurement, as discussed in Section 2.3. For example, to measure heart rate, one approach involves using motion sensors and placing the phone at the chest level (motion sensing, see Section 2.4.1). Another approach is to utilize the camera and flash of the device, requiring the user to place their finger on it to measure the variation of light intensity associated with changes in blood volume (photoplethysmography), see Section 2.4.3).

Figure 2.1 illustrates the typical sensors commonly found in smartphones. In the future, we can expect the emergence of novel sensors as manufacturers increasingly focus on integrating innovative functionalities into their devices. A notable example is the introduction of a thermometer sensor in Google's Pixel 8 [1][34], specifically designed to measure the user's body temperature. These advancements in sensor technology hold significant potential to enhance interaction between individuals and their environment, particularly in the field of mHealth.

1. https ://www.blog-nouvelles-technologies.fr/261992/google-pixel-8-pro-inclura-un-thermometre/

2.1.2 Computing power

In addition to its many sensors, which enable it to measure various properties of the environment, the smartphone is also equipped with computing power, making it capable of running programs and process collected data to extract medical information. The introduction of the IPhone in 2007 marked a significant turning point in smartphone computing power, with its powerful processor and multi-touch display setting a new standard for the market. Since then, the pace of advancement has been astonishing, with processors becoming more powerful and Graphics Processing Units (GPUs) enabling better graphics and smoother performance, especially designed to enhance gaming experience. Efficient manufacturing processes for components have enabled manufacturers to pack more processing power into smaller devices without sacrificing battery life, while mobile operating systems such as iOS and Android have been optimized to take full advantage of the latest hardware advancements.

Today, some smartphone models rival the processing power and memory of high-end laptops, capable of handling complex tasks like video editing and 3D gaming while running multiple apps simultaneously without slowing down. For example, the Galaxy Z Fold 3 [2], released in 2021 has 12 GB of RAM and 256 or 512 GB of storage, while the first Galaxy S smartphone released in 2010 had just 512 MB of RAM and 8 or 16 GB of total storage. Samsung's recent offering, the Samsung Dex [35], even allows smartphones to be used as a computer by connecting to an external display, such as a TV or monitor. Samsung is advocating for a "Mobile-only" paradigm, where the smartphone can be adapted to a laptop if necessary by connecting external devices. As this trend continues, the computing power of future smartphones is likely to increase, pushing the limits of what can be done by mHealth systems designed on top of them.

2.1.3 Radio communication capabilities

Smartphones are ideal for democratizing healthcare also due to their telecommunication capabilities. These capabilities have been made possible by the evolution of smartphone radio sensors. These sensors allow smartphones to connect to a wide range of wireless networks and communicate with other devices. The most common types of radio sensors found in smartphones include cellular radios, Wi-Fi radios, Bluetooth radios, Near Field Communication (NFC) radios, Global Positioning System (GPS) radios, and Radio Frequency Identification (RFID) sensors.

Cellular radios were the first radios to be equipped in smartphones. They allow smartphones to connect to mobile networks and make voice calls and send text messages. Over time, cellular radios have become more advanced with the introduction of 3G, 4G, and now 5G networks, providing faster data speeds and more reliable connectivity. Wi-Fi radios have also become a standard feature, allowing smartphones to connect to wireless networks and access the internet, reducing the need for cellular data plans. Bluetooth radios have enabled a wide range of new applications, such as wireless audio streaming and fitness tracking, by allowing smartphones to connect to other devices such as headphones,

2. https ://www.samsung.com/fr/smartphones/galaxy-z-fold3-5g/

speakers, and smartwatches. NFC radios allow for contactless payments, ticketing, and other secure communication applications at close range, typically within a few centimeters. GPS radios allow smartphones to determine their location using signals from GPS satellites, which is used for location-based services such as maps, directions, and location-based advertising. RFID sensors are used to identify and track objects using radio waves. Some smartphones are equipped with RFID sensors that are used for inventory management and other applications.

mHealth solutions can leverage these telecommunication capabilities to exchange data between the smartphone and third-party equipment. For example, an app can use this technology to send real-time information collected by the device to a healthcare provider. Some authors also use these radio sensors, especially Bluetooth, to connect external sensors to the smartphone (such as headphones, speakers, and ECG sensors) [36] in order to enhance the sensing capabilities of the device for their mHealth system. Finally, mHealth systems may use these sensors to communicate with remote computing servers to overcome the limited computing capability of the device or to conserve battery life [10, 37].

In addition to their telecommunication capabilities, these technologies can be utilized to collect data. As sensors, they capture electromagnetic waves that can be used to measure information in collaboration with the environment. An illustrative instance is the field of Wi-Fi sensing, which encompasses extensive research efforts to leverage existing wireless signals to detect and track the presence and movement of individuals or objects within a specific area. Since smartphones are equipped with Wi-Fi, this technique is often used in mHealth systems, as we discuss in Section 2.4.4.

With its diverse sensors, powerful computing capabilities, and telecommunication functionalities, the smartphone serves as a versatile platform for mHealth sensing systems. Building upon these foundational capabilities, the next section will delve into the challenges involved in designing mHealth systems.

2.2 Challenges of designing mHealth solutions

Designing mHealth systems comes with significant challenges. First, while smartphones are highly sophisticated, they are still pocket-sized devices with inherent technical limitations in terms of physical resources. Secondly, making this technology available to a lay user in an uncontrolled environment poses additional challenges that must be considered. Finally, the sensitivity of the data measured raises a privacy concern. In the following sections, we will discuss each of these challenges in more detail.

2.2.1 Device limitations

The hardware limitations is one of the primary challenges faced by any mHealth system. This challenge can be broken down into several sub-challenges :

— **Limited resources :** Smartphones have a limited power and battery life, which

necessitates that the solution be as resource-efficient as possible, so as not to prevent the user from using the phone for its primary functions, by draining the battery.

— **Non-standardized hardware :** Unlike medical equipment, where the manufacturer has control over both hardware and software, adapting to the differences in smartphone hardware presents its own challenges. Sensors have varying levels of sensitivity and accuracy, which must be accounted for by the algorithmic part of the designed system. This is typically addressed during preprocessing stage, as explained in Section 2.3.2.2.

— **Sensor limitations :** As smartphone sensors are not designed for medical applications, adapting to their limitations poses a unique challenge. For example, commercial pulse oximeters [3] typically employ two different wavelength light sources (i.e., 660 and 940nm) to accurately measure oxygen saturation levels, whereas smartphones rely on a single white flash light that emits a broad spectrum of wavelengths (400 800 nm)[9]. This discrepancy in light sources can affect the accuracy and reliability of the measurements. Additionally, the relatively lower sampling rate of smartphone-based finger photoplethysmography (around 30 Hz) compared to commercial oximeters (up to 1000 Hz) results in lower data resolution, which can impact the precision of the measurements. To mitigate these challenges, state-of-the-art systems often involve adapting the models or employing preprocessing techniques to compensate for the limitations of smartphone sensors.

2.2.2 Context limitations

In addition to hardware limitations, user limitations are also important to consider in the development of a mHealth systems. The goal is to make these systems user-friendly and accessible to individuals without specialized training. Additionally, the test environment poses its own challenges, particularly when designed for home use. Factors such as limited control over the experimental environment, variations in lighting, temperature, and ambient noise can impact the accuracy of measurements. To address these challenges, three strategies may be employed :

— **Inform** : Previous work has focused on providing clear instructions and information to users regarding proper usage conditions. This can be achieved through descriptive messages or visual cues displayed on the application interface [10, 38, 39].

— **Control** : Another approach involves leveraging additional sensors and algorithms to verify whether users adhere to the designated usage protocol and if the external conditions are suitable. For example, in [9], the quality of finger placement over the camera for photoplethysmography measurements is verified by analyzing the image coarseness. Similarly, in contactless photoplethysmography (discussed in Section 2.4.3), algorithms are often employed to track the target face in recorded images [40].

— **Correct** : To mitigate potential human errors and enhance measurement reliability, another relevant approach consists in designing specific algorithms during the pre-

3. A pulse oxymeter is the portable clinical device used to measure one blood oxygen level.

processing stage. These algorithms can include filtering techniques or be integrated directly into the model itself, enabling predictions and compensations for expected errors introduced by the user or the experimental environment. For example, in a study on measuring the viscosity of a liquid in a container [41], researchers implemented a customized calibration scheme within their model to account for variations in the volume of the sample. By incorporating such correction algorithms, mHealth systems aim to improve the accuracy and consistency of collected data, providing more reliable insights for healthcare applications.

2.2.3 Data privacy

The sensitive medical data collected by smartphones in this field raises concerns about potential risks, including unauthorized access to the application's measurements and compromise of user privacy [42]. To address this, it is necessary to ensure that data can only be accessed by the legitimate user, and through the application. One solution is to encrypt the stored data using cryptographic tools, making it unreadable to unauthorized individuals [43]. Additionally, keeping the data processing solely within the smartphone itself, without transmitting it over the network, provides an extra layer of protection against unauthorized access. As digitalization advances, the security of sensitive data remains a universal concern, and advancements in other domains can contribute to improving the security of mobile health applications.

To meet all these challenges, mHealth systems exhibit a common architecture, which we describe in the next section.

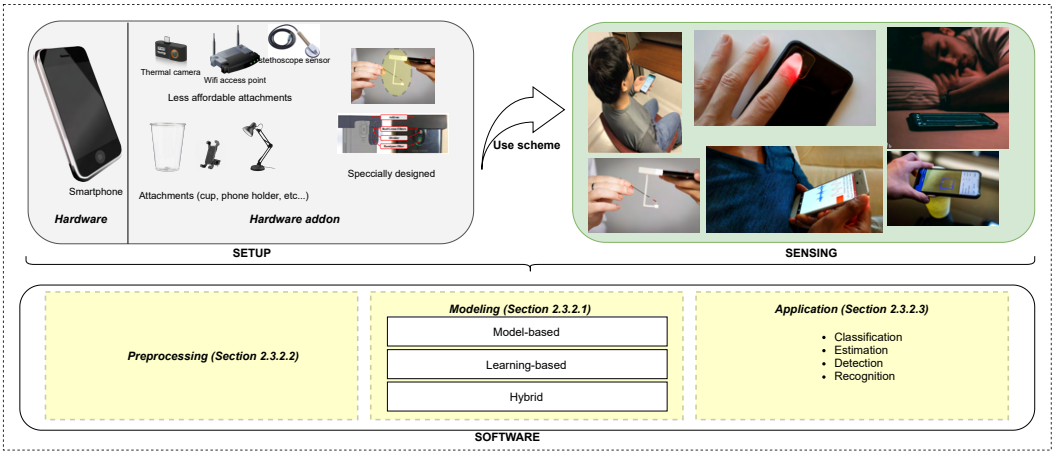

FIGURE 2.2 – Global architecture of state-of-the-art mHealth solutions.

2.3 Architecture of mHealth solutions

For all the diversity of state-of-the-art mHealth solutions, their underlying architecture comprises 2 main components : the setup, which includes the hardware and the use scenario, and the algorithms, usually implemented in software. The hardware component encompasses the sensors, computing power, and any other materials necessary to facilitate the data measurement process. These components are responsible for capturing the required data accurately and efficiently. The use scenario [4] provides instructions and guidance to users on how to effectively use the system. It outlines the proper usage of the hardware and specifies the actions needed to record the data. Following the use scenario correctly ensures that the system can collect the necessary data for further processing. The software component processes the recorded data to achieve the objectives of the mHealth system. It applies various techniques, calculations, and algorithms to extract valuable information and generate meaningful outputs from the collected data. Figure 2.2 represents an illustration of the proposed architecture, featuring illustrations issued from several works [23, 27, 44, 45]. In the following sections, we discuss in detail each component.

2.3.1 Setup

Starting with an intuition of which sensor to use to collect the data relevant to the problem, the first thing to clarify is the complete system setup. Specifically, this includes both the physical hardware, any additional external material required, and a description of the scenario in which it will be used, for the data to be collected reliably.

2.3.1.1 Hardware

The hardware relies mainly on the smartphone, which comprises sensors that measure the environment and the necessary computing power to process the data and extract

4. We also refer to it as a use scheme throughout the document.

valuable information. The selection of sensors and processing methods is a closely interrelated process. For instance, to measure cardiac activity, some approaches leverage camera and computer vision techniques [46], while others rely on inertial sensors and motion analysis techniques [15]. We delve into these techniques in detail in Section 2.5. We provide an insight to decide which sensor to investigate in our proposed methodology, in Section 3.

In some cases, however, it's not enough to rely on the sensors already present in a smartphone. In these situations, additional hardware may be needed. This can range from support equipment that may be readily available for the end user (such as a smartphone holder [27], a container for the substances [23, 25]), to an external sensor that can be connected to the phone via cable or wireless technology [36], or even a specially manufactured component (like a special light source [11]). In rare cases, modifications to the phone's hardware may be necessary [9, 22]. In general, adding additional hardware or customizing the smartphone hardware enhances the accuracy of the system but may reduce its accessibility for users. Considering the vision of this thesis, we prioritize using only the smartphone itself or widely accessible extra attachments, thereby shifting the complexity to the software part.

2.3.1.2 The usage scenario

The use scenario explains how the device captures health-related data from the environment. Different systems may utilize different sensors or employ the same sensor in different ways to measure the same health information. The design of the usage scenario is guided by the comfort and ease of use for the user and the quality of the input data required for the processing techniques envisaged.

For example, when measuring heart activity, some systems require placing the phone on the chest to record heart movement using inertial sensors [44], for maximized data quality. On the other hand, some systems require holding the phone in the hand [15] to enable opportunistic tracking of cardiac activity. Furthermore, certain systems employ the front camera and Transdermal optical imaging (TOI) for contactless blood sensing [47], while others use the rear camera and finger photoplethysmography, putting the emphasis on the quality of the measured blood flow data [28]. In both cases, the processing involves measuring changes in blood volume in the body part by tracking the color changes through the recorded images. We discuss these techniques in detail in Section 2.4.3.

The main purpose of the usage scenario is to ensure that the system is correctly employed. This is crucial because the quality of the system's final output depends on the quality of the measured data, which ultimately relies on how well the protocol is followed.

2.3.2 Algorithms

The software of the mHealth system is designed to extract information for medical purposes from the raw data collected using the setup, in order to provide the service the system is intended for. One way to depict its design is to consider it as three essential

parts : Modeling, Pre-Processing, and Application.

2.3.2.1 Modeling

The modeling stage of a mHealth system involves establishing the mathematical relationship, denoted as f, between the measured raw data X and the medical information of interest Y. There are two primary strategies in the literature to achieve this.

model-based approach

The first approach, called model-based, involves directly formulating the model f based on physical theories. This strategy is the most reliable but requires expertise in the system and the physical laws that govern it. For example, the Beer-Lambert law [29] is commonly used to model the mathematical relationship between the residual light intensity and the concentration of oxygenated blood, when using photoplethysmography to estimate oxygen level in blood[9, 46, 48], as we see in details in Chapter 4.3.1.

learning-based approach

The second approach, called learning-based, involves learning the model f from previously collected and labeled training data X', Y'. Once the model is learned, it can be used to estimate Y for new input data X. Different learning algorithms are used for this strategy, which is detailed in Section 2.5.3. Learning-based strategy is used when the scientific intuition between the measured data and the medical information is difficult to formulate analytically or involves unknown parameters. This approach has been used for example to estimate blood glucose level [49] and blood hemoglobin concentration [11] from Photoplethysmogram (PPG) signals.

hybrid approach

Finally, it is possible to use a mixed strategy, which combines both the model-based and learning-based approaches. In this hybrid approach, the link between the input data and medical information, f_{theta}, is theoretically modeled, where f_{theta} depends on some unknown parameters *theta*. These unknown parameters are then learned with labeled data, making this strategy useful when the model is not accurate enough. It has been widely used for instance, to estimate blood pressure from from PPG signals[44, 50-53].

2.3.2.2 Data preprocessing

Preprocessing is an essential step in the software aspect of the system, where the raw data captured by the sensors are prepared to align with the model. This involves applying various algorithms such as noise cleaning, data calibration, data standardization, and filtering. Additionally, specific calibration algorithms may be designed to address the limitations of the device mentioned earlier, which is one of the major challenges in building a mHealth system (see Section 2.2). A review of the most common pre-processing techniques used in mHealth is discussed in Section 2.5.2.1. The preprocessing stage plays

a crucial role in enhancing the quality and reliability of the collected data, ensuring accurate analysis and interpretation in subsequent stages.

2.3.2.3 Application

After pre-processing the data, they are passed through the model to obtain the information of interest, y, which may finally be interpreted in order for the system to provide its service. While works in vital sign monitoring focus solely on obtaining the medical information, in disease screening and home testing, the goal often involves measuring one or multiple pieces of health-related information, which are then combined and merged to provide the final result to the user. For example, to detect depression, some works measure both the frequency of social media interactions and the time spent using the smartphone [19]. Another example, is the system can measure the viscosity of a food product in order to determine if it is suitable for consumption by patients suffering from dysphagia, by comparing it to a threshold [25]. Furthermore, some systems are required to obtain cardiac activity signals both from the chest through the inertial sensor and finger through photoplethysmography in order to estimate blood pressure, by converting the time delay between both signals [44].

Once various pieces of information have been measured, the possible applications can be distinguished as classification, regression, detection, or recognition problems, depending on the ultimate goal of the mHealth system. For instance, the application may consist in *classifying* patients as healthy or not based on their measurements [54], *detecting* abnormal patterns in the heart rate activity [55], or *recognizing* melanoma on a photo of a spot on the skin [56, 57]. We discuss the types of algorithms used for this purpose in more detail in Section 2.5.3.

From this architecture representation, we have enough elements to understand the process of designing an mHealth solution. However, it is not uncommon to reuse proven data collection techniques when designing a new mHealth system. By reusing sensors, usage protocols, and preprocessing algorithms, we can focus our design efforts on modeling, managing specific constraints, and developing the final application. We refer to these reused data collection techniques as mHealth sensing approaches or techniques. In the following sections, we will present the most commonly reused approaches, as they serve as fundamental building blocks for designing any new system.

2.4 mHealth sensing techniques

The literature contains a range of techniques used in the design of mHealth solutions, which can be grouped according to the type of sensor used to collect data. Although there is a richer body of research on motion sensing, acoustic sensing, computer vision, and Wi-Fi sensing, some researchers are beginning to explore the use of sensors that are not typically included in those techniques in their systems. For example, some studies have utilized the screen [33], infrared sensor [22], or external sensors [12, 36]. As smartphones continue to advance and incorporate new sensors, we can expect the emergence of new

techniques in the future. This section will focus on the most common techniques used in the current literature.

2.4.1 Motion sensing

Motion sensing techniques primarily rely on using inertial sensors in smartphones to capture the displacement of the phone caused by external movements. The collected data is then processed based on its characteristics to extract medical information.

For example, when analyzing cardiac activity, there are two main techniques : ballistocardiography and seismocardiography, each measuring different aspects of heart movements.

Seismocardiography involves measuring the vibrations of the chest produced by heart movements. The smartphone, placed on the chest, is used to record these vibrations and convert them into a time series signal called a seismocardiogram. Seismocardiography is commonly used for detecting abnormalities in cardiac movement and monitoring heart function [58].

On the other hand, ballistocardiography measures the forces generated by cardiac movements. It utilizes the smartphone's motion sensors placed on an indirect measurement surface, such as a bed, chair [59], or even a hand [15], to record the forces exerted by the body during heartbeats. These forces are then converted into a temporal signal known as a ballistocardiogram.

Motion sensing-based techniques are also employed in collecting and analyzing respiratory motion. In some cases, the system requires the phone to be in contact with the human body, like in a pocket or during a call [60]. In other cases, the phone is placed on the bed [59] to track breathing during sleep and detect sleep apnea. Additionally, these techniques are used in liquid analysis, where inertial sensors record the vibration of a liquid. The obtained signal is further processed to estimate the viscosity of the liquid [25, 41].

In general, this type of technique is used when the system is in direct contact with the tested object, and when the movement being measured is relatively large or occurs regularly. Smartphone accelerometers are sensitive, but they may not provide a significant Signal to Noise Ratio (SNR) for subtle movements. However, when the motion is periodic, advanced signal processing techniques (see Section 2.5.2) can be used to extract the required information even when the SNR is low.

2.4.2 Acoustic Sensing

This family of techniques is based on the use of the microphone of the device. It consists in recovering medical information from sound data measured on the environment. The most used techniques here are audible sound analysis, acoustic motion tracking and acoustic impedance sensing.

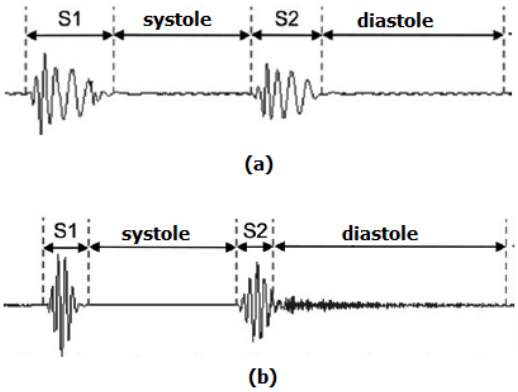

FIGURE 2.3 – Example of phonocardiogram, featured with Characteristics of heart sounds, for (a) normal and (b) abnormal heart sounds. Figure from [66].

2.4.2.1 Audible sound analysis

The analysis of audible sound involves processing the raw audio signal produced by the subject and coupling it with time-series signal processing algorithms. Such techniques are widely used in cough analysis to detect respiratory problems like Coronavirus (SARS-CoV-2)[61], asthma, and Chronic Obstructive Pulmonary Disease (COPD)[10]. They have also been used to diagnose Parkinson's disease based on abnormal body sounds [62].

Another specific application of this technique is phonocardiography, which is used to study cardiac activity. This involves recording and analyzing the sounds produced by the heart. The device's microphone is placed on the chest to record heartbeat sounds, which are then processed to diagnose various heart conditions such as heart valve problems [63], heart murmurs [64], and congenital heart defects [65]. Figure 2.3 shows an example of a healthy and unhealthy phonocardiogram.

2.4.2.2 Acoustic motion tracking

Acoustic motion tracking refers to the use of an audio signal to track small movements. Historically used to track human gestures [67, 68], it has recently been increasingly used in the mHealth community, particularly for breath sensing [27, 69, 70]. It works by emitting an acoustic signal - mostly an inaudible sound to avoid noise pollution - towards the target and recording the echo returned by it. By measuring the phase shift between the two signals, the time delay, and thus the distance between the smartphone and the target can be determined.

The phase shift of an echo sound wave can be mathematically expressed using the following equation :

$$\Delta\phi = 2\pi f \Delta t \tag{2.1}$$

Where $\Delta\phi$ is the phase shift of the sound wave, measured in radians, f is the frequency of the sound wave, measured in hertz, Δt is the time delay between the emission of the original sound wave and the reception of the reflected sound wave, measured in seconds.

This equation is derived from the fact that the phase of a sound wave is proportional to the product of its frequency and time. The 2π factor in the equation represents a complete cycle of the wave, as the phase of a sound wave completes a full cycle after traveling a distance equal to its wavelength.

Since the time delay between the emission of the original sound wave and the reception of the reflected sound wave corresponds to twice the distance between the sound source and the reflective surface, one can relate the phase shift of an echo sound wave to the distance between the sound source and the reflective surface using equation 2.2 :

$$d = v\Delta t/2 \tag{2.2}$$

Where v is the speed of the sound, and d is the distance between the sound source and the reflective surface, measured in meters.

This technique is sensitive enough to track movements on the order of a few millimeters in amplitude [27]. A major advantage is that it does not require direct contact between the device and the target.

2.4.2.3 Acoustic impedance sensing

Acoustic impedance is a measure of the opposition that a medium (such as air, water, or a solid material) presents to the propagation of sound waves. Acoustic impedance is a key property that determines how sound waves are transmitted and reflected at the boundary between different materials. When a sound wave encounters a change in acoustic impedance at a boundary, some of the energy is reflected and some is transmitted. The amount of reflection and transmission depends on the difference in acoustic impedance between the two materials.

Leveraging this technique for mHealth sensing consists on generating acoustic signals through the speaker and collecting the reflected signals from the surroundings using the microphone of the device. Using frequency based signal processing algorithms (see Section 2.5.2), one can analyse correlations between energy distribution and the nature of the reflecting object. This technique has been for example investigated for liquid testing [71], in the use case of urine testing.

2.4.3 Computer vision

This family of techniques concerns the use of the camera to record and process one or more images in order to retrieve the health related information. The difference between the different techniques of this category is the way of processing the image, and the property sought. Especially in smartphone-based liquid testing, computer vision techniques differ in the properties they seek. Some are based on the analysis of motion through video, such as capillary waves motion of the liquid surface to estimate its surface tension [23]. Others are more interested in the properties of light absorption of the liquid, and deal rather with the color [72]. For blood sensing, one of the majors technique of this kind is Photoplethysmography.

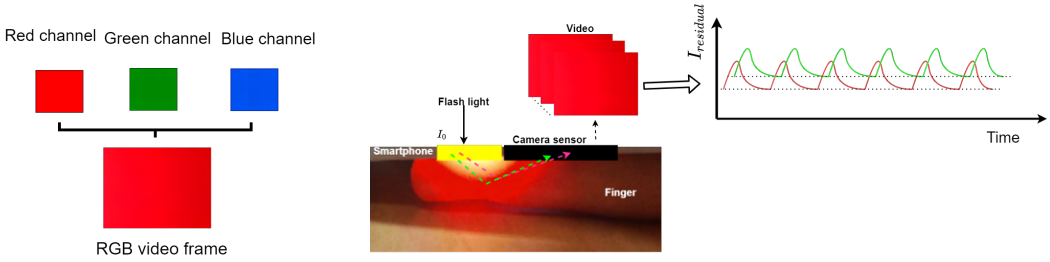

(a) A video frame, made up of three single-color channel images.

(b) Recording several video frames for the finger illuminated by the flash, and averaging each color channel to obtain the PPG signals

FIGURE 2.4 – Illustration of smartphone-based photoplethysmography.

Photoplethysmography

The principle of Photoplethysmography involves using a light source, usually the LED of the device, to emit light through the patient's skin, and record the residual light reflected back through the camera. When the heart beats, it causes variations in blood volume in the blood vessels beneath the skin, altering the amount of light absorbed by the blood. These fluctuations leads to change in the intensity of the recorded images, which can be extracted as a signal, called photoplethysmogram (PPG).

The PPG signal appears as a waveform with peaks and troughs (illustrated in Figure 2.4). Each peak corresponds to a period of heart contraction (systole), while each trough represents a period of heart relaxation (diastole). It has been used to measure many blood related vital parameters including heart rate[46], blood oxygen level[9, 73], blood pressure[51, 52, 74], blood glucose level[49], etc.

This technique is highly popular due to its ease of implementation and use. By focusing on the user's face, it allows for a contactless measurement of blood flow (also refers to as Transdermal Optical Imaging TOI, or contactless photoplethysmography). However, when focusing on the finger (refers to as finger photoplethysmography), a higher-quality PPG signal can be obtained. The choice of the body part depends on the specifics requirements of the system.

2.4.4 Wi-Fi sensing

Wi-Fi sensing is a technique that involves using Wi-Fi-enabled devices, such as smartphones or routers, to analyze wireless signals and extract information about the surrounding environment. It works by analyzing variations in Wi-Fi signals caused by the movement of people or objects. These variations can be used to detect the presence, location, and movement of individuals in a given space. In the context of mHealth, there are two main Wi-Fi sensing approaches, each based on different input data for their systems :

— ***CSI-Based*** : Channel State Information (CSI) refers to information about the wireless channel used to transmit data between a Wi-Fi access point and a client device. CSI includes details about signal strength, phase, and other parameters of the wi-

reless signal. mHealth systems can exploit this information to deduce details about the environment. For example, studies have shown that Wi-Fi CSI sensing can accurately detect changes in gait patterns, which may indicate Parkinson's disease or other neurological conditions [75, 76]. Additionally, CSI has been used to monitor vital signs such as heart rate and respiratory rate by analyzing changes in CSI caused by breathing and heartbeats [77-79]. Wi-Fi CSI has also proven successful in detecting falls or abnormalities in behavior, particularly for elderly care or individuals with mobility issues [80].

— ***RSSI-Based*** : Another approach to Wi-Fi sensing focuses on Signal Received Strengh Indicator (RSSI). This method involves analyzing how the RSS at a Wi-Fi-enabled device, held on a person's chest for instance, is affected by the breathing process. Some researchers have utilized these changes in Wi-Fi RSSI patterns to enable ubiquitous non-invasive respiratory rate estimation and apnea detection [81]. However, since RSS provides less information than CSI, fewer studies employ this method.

Wi-Fi sensing has the potential to provide continuous, non-invasive monitoring of patients in their homes. However, it always requires a wireless access point to operate, which is a trade-off for its ability to monitor human health without physical contact using a smartphone.

The data measured by all these techniques are often images or time series. Consequently, it is not uncommon to encounter the same mathematical tools in their processing. In the following section, we examine the most common processing techniques used to extract information from such data. In the following chapters, we will reuse some of these techniques to process the data for our specific applications.

2.5 mHealth data processing techniques

The data collected by the mHealth systems comes from the different sensors of the smartphone. They are mainly time series, image and video data. In this section we will first define the data structures used to manipulate them by the algorithms, and then present the existing processing techniques commonly used to process them.

2.5.1 Data structures

Smartphone sensors collect data at a sampling frequency Fs, which varies depending on the sensor and smartphone model. For instance, the microphone typically has a sampling rate of around 72 kHz, while the accelerometer has a rate of 100 Hz.

We can represent the obtained signal using a vector, $x = [x_{t_1} ... x_{t_n}], n \in \mathbb{N}^*$. On the other hand, the camera captures a 2D image encoded in three color channels (red, green, and blue). We can represent the image using a matrix, $x[i, j, k]_{i=1..W, j=1..H}^{k=1..3}$, where the first two dimensions represent the height and width, respectively, and the last dimension repre-

sents the color channel. If we are dealing with videos, we can add a fourth dimension to consider time.

2.5.2 Signal processing

Signal processing is the field of study which focuses on the manipulation, analysis, and transformation of signals, which are representations of physical phenomena such as sound, images, and data like a series of sensor readings. The goal of signal processing is to extract meaningful information from these signals, enhance their quality, or compress them for storage or transmission. Examples of signal processing techniques widely used in mHealth literature include smoothing, frequency analysis, and feature extraction.

2.5.2.1 Signal smoothing

Signal smoothing is a technique used in signal processing to reduce the amount of noise or other unwanted fluctuations in a signal. It involves applying a mathematical filter to the signal that eliminates or reduces the high-frequency components of the signal, which are typically associated with noise or other disturbances.

The basic idea of signal smoothing is to remove the rapid changes in a signal that are not of interest, while retaining the slower, more significant changes. The resulting smoothed signal is often easier to analyze and interpret than the raw signal, as it removes the effects of noise and other unwanted fluctuations.

There are several common signal smoothing algorithms used in mHealth literrature, including :

1. Moving average : This is a simple technique that involves computing the mean of a window of adjacent samples and using it as the smoothed value. Moving average is easy to implement and can effectively reduce high-frequency noise, but it can also introduce lag in the signal. The moving average of a signal x at time t is defined as :

$$x'(t) = \frac{1}{N} \sum_{i=t-N+1}^{t} x(i) \tag{2.3}$$

   where N is the number of data points used in the moving average.

2. Savitzky-Golay filter [82] : This filter is good at preserving the shape of the signal, but it can be computationally intensive. The Savitzky-Golay filter fits a polynomial of degree k to a window of $2m+1$ data points centered on each point in the signal. The filtered value at time t is given by :

$$x'(t) = \sum_{j=-m}^{m} c(j) \cdot x(t+j) \tag{2.4}$$

   where the coefficients $c(j)$ are determined by a least-squares fit of the polynomial to the window of data points.

3. Low-pass, high-pass, and band-pass [83] : These filters are three common types of frequency-selective filters used in signal processing. Each filter is designed to pass signals within a certain frequency range while attenuating signals outside that range.
4. Median filter : The median filter replaces each data point with the median of its neighboring points. For a window of $2m + 1$ data points centered on time t, the filtered value at time t is given by :

$$x'(t) = \text{median}(x(t-m), x(t-m+1), \ldots, x(t), \ldots, x(t+m-1), x(t+m)) \tag{2.5}$$

5. Gaussian filter [84] : A Gaussian filter applies a Gaussian function to each data point and its neighbors. For a window of $2m+1$ data points centered on time t, the filtered value at time t is given by :

$$x'(t) = \frac{1}{Z} \cdot \sum_{i=-m}^{m} x(t+i) \cdot e^{-\frac{i^2}{2\sigma^2}} \tag{2.6}$$

where Z is a normalization constant to ensure that the filter preserves the signal amplitude, and σ is a parameter that controls the width of the filter.

The important factor to consider when choosing the suitable smoothing technique is the specific characteristics of the desired signal and the requirements of the application. Factors such as the level of noise in the signal, the desired degree of smoothing, and the available processing power can also influence the choice of algorithm. For low-noise signals, simple techniques like moving average or Savitzky-Golay filters may be sufficient. However, for high-noise or non-linear signals, more advanced techniques like the Kalman filter [85] may be necessary. In some cases, using band-pass filters can be a good alternative, especially when we have prior knowledge of the frequency range that contains meaningful information in the data. By applying these filters, we can effectively eliminate noise by discarding frequencies outside of the desired range.

2.5.2.2 Signal frequency analysis

Signal frequency analysis is the process of studying the frequency content of a signal to extract relevant information or identify patterns. It involves analyzing the signal in the frequency domain, which provides insights into the different frequency components present in the signal. There are several major techniques used in signal frequency analysis, including Fourier transform, power spectrum analysis and wavelet transform.

Signal Fourier analysis

Signal Fourier analysis is a mathematical technique used in signal processing to analyze the frequency content of the signal. The technique is based on the Fourier transform, which is a mathematical operation that decomposes a signal into its constituent sinusoidal components. The Fourier transform allows to represent a signal in the frequency domain,

where it maybe easier to retrieve meaninglfull informations from it, especially if we are dealing with a periodic phenomena.

The Fourier transform of a continuous-time signal $x(t)$ is given by [86] :

$$X(f) = \int_{-\infty}^{+\infty} x(t)e^{-j2\pi ft}dt \tag{2.7}$$

where j is the imaginary unit, and f is the frequency. The Fourier transform expresses the signal $x(t)$ in terms of its frequency components, which are represented by the complex exponential $e^{j2\pi f}$. The magnitude of the Fourier transform $|X(f)|$ represents the amplitude of each frequency component, while the phase angle represents the phase shift of each component relative to a reference.

By analyzing the frequency content of a signal, we can identify important features such as dominant frequencies, harmonics, noise, and distortions. This information can be used to design filters, remove noise, compress data, extract features, and enhance signals as a preprocessing step for the mHealth application.

Signal Power Spectral Density (PSD)

The Power Spectral Density (PSD) of a signal is a mathematical function that describes how the power of the signal is distributed over the frequency domain. It is a measure of the power density of the signal per unit of frequency. In other words, the PSD gives us information about the strength of the signal at different frequencies.

The PSD of a continuous-time signal x(t) is computed as the squared magnitude of its Fourier transform X(f) [87] :

$$S_x(f) = ||X(f)||^2 \tag{2.8}$$

where $*$ denotes complex conjugation and f is the frequency.

The PSD can be used to extract useful information from a signal, such as its dominant frequencies, bandwidth, and noise level. An example of its common typical usage is illustrated in Figure 2.5, where we show how from the raw PPG signal we can estimate the heart rate of the user by identifying the dominant frequency.

Wavelet transform

The Continuous Wavelet Transform (CWT) [88] is a mathematical tool used for signal analysis, providing a localized representation of signals in both time and frequency domains. Unlike the Fourier transform that employs sinusoidal basis functions, the CWT utilizes wavelet functions that are localized in time and frequency. This localization property enables the CWT to capture transient events, analyze non-stationary signals, and extract features from signals with complex dynamics.

The CWT of a continuous-time signal $x(t)$ at scale a and translation b is obtained through the convolution of the signal with a scaled and translated wavelet function $\psi(t)$, also known as the analyzing wavelet or mother wavelet. The CWT equation is as follows :

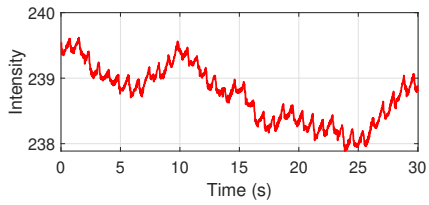

(a) Raw PPG signal.

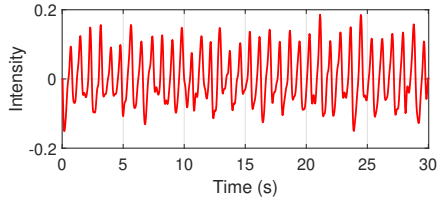

(b) Pass-band filtered with cutoff frequencies 0.5 and 4Hz.

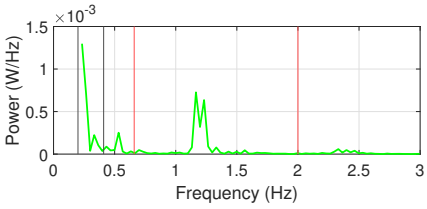

(c) PSD of the raw ppg signal

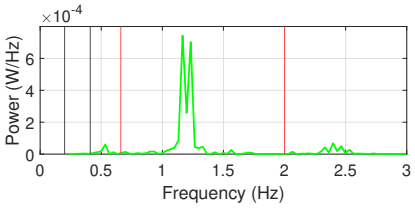

(d) PSD of the filtered signal.

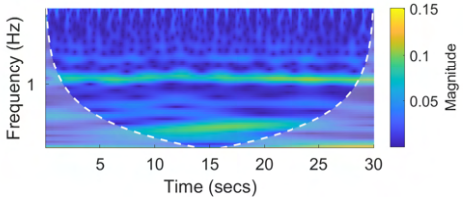

(e) Scalogram, representing the CWT of the raw ppg signal

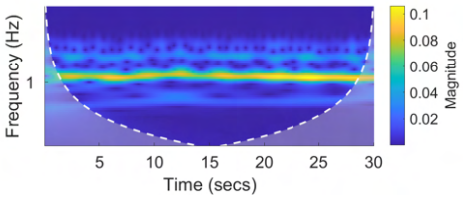

(f) Scalogram, representing the CWT of the filtered signal.

FIGURE 2.5 – A straightforward photoplethysmogram (PPG) signal processing pipeline allows for heart rate estimation. We obtain the Raw PPG signal (Fig. 2.5a) by averaging the red color channel of each frame and then filter it (Fig. 2.5b). The resulting PPG signals show peaks and valleys corresponding to the participant's blood flow in the finger. The Power Spectral Density (PSD) of the raw signal (Fig. 2.5a) displays two main peaks, indicating the breathing rate and heart rate. In Fig. 2.5d, the PSD of the filtered version only exhibits the heart rate peak. Additionally, the scalogram of the filtered version (Fig. 2.5f) shows a stronger intensity around 1.2Hz compared to the raw signal's scalogram (Fig. 2.5e), representing the heart rate once again.

$$CWT(a,b) = \int_{-\infty}^{+\infty} x(t)\frac{1}{a}\psi^*\left(\frac{t-b}{a}\right)dt \tag{2.9}$$

Here, the symbol $*$ represents complex conjugation, and $\psi^{\left(\frac{t-b}{a}\right)}$ represents the analyzing wavelet function ψ scaled by the factor a and translated by the amount b.

A common visualization of the wavelet transform is the scalogram, which displays the distribution of signal energy across different scales (or frequencies) and time. It is typically represented as a 2D plot, with the y-axis indicating scale or frequency, the x-axis representing time, and the color or intensity indicating the magnitude or strength of the frequency component. Examples of scalograms are shown in Figures 2.5e and 2.5f. Scalograms have been utilized in various applications, such as recognizing heartbeat events from noisy accelerometer recordings obtained while the phone is held by the user, using deep learning-based processing techniques [15].

2.5.2.3 Signal feature extraction

Signal feature extraction refers to the process of identifying and quantifying specific characteristics or patterns within a signal that are relevant for a particular application or analysis. These features capture essential information from the signal and are used to describe or represent the signal in a more compact and meaningful way.

The relevance of certain features varies depending on the type and origin of the signal. When it comes to mHealth applications, we typically rely on intuition and proceed by trial and error to identify the most appropriate features for the specific application targeted. The commonly considered feature types for time series signals are as follows :

- ***Time-domain features :*** These features are computed directly from the signal waveform in the time domain. They include statistical measures such as mean, standard deviation, skewness, auto-correlation coefficients, and kurtosis. Other time-domain features may include zero-crossing rate, energy, entropy, or various temporal characteristics [89].
- ***Frequency-domain features :*** These features are derived from the signal's frequency content. They are often obtained through signal frequency analysis techniques discussed earlier (Section 2.5.2). Common frequency-domain features include spectral centroid, spectral bandwidth, spectral roll-off, and spectral moments [89].
- ***Waveform shape features :*** These features focus on the shape or morphology of the signal waveform. They can include characteristics such as peaks, valleys, slopes, or other geometric properties. For instance, waveform features extracted from PPG signal is a common approach for estimating blood pressure [28, 51, 53, 90-92].

These features, once extracted, are typically used as input to machine learning algorithms (discussed in Section 2.5.3) or other analysis techniques for tasks such as classification, detection, recognition, and regression [93, 94].

2.5.2.4 Image processing

Image processing is a branch of signal processing that deals with the analysis and manipulation of digital images. It involves using mathematical and algorithmic techniques to enhance or modify images to improve their quality or extract useful information. In this section, we will focus on some widely used image smoothing and edge defections techniques.

Image smoothing

Image smoothing is a technique used to reduce noise or remove small details while preserving the overall structure of the image. The process involves replacing each pixel in the image with an average of its neighboring pixels. This helps to reduce the effect of small variations in the pixel values and produce a smoother version of the image. There are several methods for image smoothing, including :

- **Gaussian smoothing [95]** : This technique involves convolving the image with a Gaussian filter, which reduces high-frequency noise while preserving the edges of the image.
- **Median filtering [96] :** This technique replaces each pixel in the image with the median value of its neighboring pixels. This helps to remove isolated pixels and preserve the edges of the image.
- **Bilateral filtering [97] :** This technique takes into account both spatial and intensity information while smoothing the image. It uses a weighted average of neighboring pixels, where the weights depend on the distance between the pixels and the difference in their intensity values.
- **Mean filtering [98] :** This technique replaces each pixel in the image with the average value of its neighboring pixels. This method is simple but may result in loss of image details.

The choice of the smoothing technique depends on the specific application and the characteristics of the image, and may be figured out after several trials.

Edge detection

Image edge detection is a technique used to identify and highlight the edges or boundaries of objects within an image, often used to focus on the object of interest inside the image. The edges in an image represent the abrupt changes in pixel intensity values and can be detected using various edge detection algorithms. One of the most commonly used edge detection technique is the Canny edge detection algorithm[99], which is computed by applying the following steps :

1. *Gaussian smoothing :* The image is first convolved with an image Gaussian filter to reduce noise. The Gaussian filter can be represented as :

$$G(x,y) = \frac{1}{2\pi\sigma^2} e^{-(x^2+y^2)/(2\sigma^2)} \tag{2.10}$$

where x and y are the spatial coordinates of the filter kernel, and σ is the standard deviation of the Gaussian filter.

2. *Gradient calculation :* The gradient magnitude and direction of each pixel in the smoothed image are calculated using the Sobel operator. The Sobel operator for calculating the gradient in the x direction is given by :

$$G_x = \begin{bmatrix} -1 & 0 & 1 \\ -2 & 0 & 2 \\ -1 & 0 & 1 \end{bmatrix} * A \tag{2.11}$$

where A is the image and $*$ denotes convolution. The Sobel operator for calculating the gradient in the y direction is given by :

$$G_y = \begin{bmatrix} -1 & -2 & -1 \\ 0 & 0 & 0 \\ 1 & 2 & 1 \end{bmatrix} * A \tag{2.12}$$

The gradient magnitude is then given by :

$$G = \sqrt{G_x^2 + G_y^2} \tag{2.13}$$

and the gradient direction is given by :

$$\theta = \arctan\left(\frac{G_y}{G_x}\right) \tag{2.14}$$

3. *Non-maximum suppression :* The gradient magnitude values are then checked in the direction of the gradient to find the local maxima. This results in thinning the edges.
4. *Hysteresis thresholding :* A double thresholding approach is used to identify the strong and weak edges. The strong edges are retained, while the weak edges that are not connected to the strong edges are removed.

There are several other edge detection techniques, including Laplacian of Gaussian (LOG) [100], Sobel [101] edge detection, and deep learning-based approaches [102, 103]. The selection of the most appropriate algorithm depends on the specific application, input image quality, and resource constraints.

2.5.3 Artificial intelligence

Artificial intelligence is a set of techniques that use the computing power of the computer to learn to extract information from large amounts of raw data without the need to explicitly know the relationship between the two. Artificial intelligence includes both machine learning and deep learning, but we can group the most used algorithms in mHealth into 3 overarching categories : supervised learning algorithms, unsupervised learning algorithms, and deep neural networks.

2.5.3.1 Supervised learning algorithms

Supervised learning is a machine learning technique where the algorithm learns from labeled data. This means that the data provided to the algorithm includes examples with class labels, and the algorithm learns from these examples by identifying features that distinguish each class. The goal is to predict the class of a new example using the features learned when training the data. The most commonly used algorithms for supervised learning are :

- **Neural Networks [104]** : Neural networks are a class of algorithms inspired by the structure and function of the human brain. They consist of multiple layers of interconnected nodes that process information and learn to recognize patterns in data. Neural networks are one of the most versatile of machine learning algorithms, but the computational cost increases hugely as the number of layers and node raises.
- **Decision Trees [105]** : Decision trees are a type of algorithm that use a series of questions to divide data into smaller and more homogeneous groups. Each question corresponds to a test on a feature of the data, and the answers to these questions determine the final classification of an example. Decision trees are often used for classification tasks and are simple to interpret, making them useful for explaining the reasoning behind a model's predictions.
- **Regression Methods** : Regression is a supervised machine learning method used for predicting continuous numerical values based on input variables. It involves building a model that establishes a relationship between the input features (independent variables) and the output variable (dependent variable). The goal of regression is to find a function that can accurately map the input features to the output variable, allowing predictions to be made for new, unseen data. This function is typically represented by a mathematical equation or a model with learned parameters. Regression models assume a specific form of relationship between the input features and the output variable (linear, polynomial, etc.). The choice of regression model depends on the nature of the problem and the assumptions made about the data.
- **Support Vector Machines (SVM) [106]** : SVM are a type of algorithm used for classification and regression tasks. They work by finding the optimal boundary between two classes of data, which is known as the maximum margin hyperplane. SVM are particularly useful for handling data that is not linearly separable, as they can use a technique known as kernel trick to project the data into a higher-dimensional space where it is easier to separate.
- **Random Forests [107]** : Random forests are an ensemble learning method that combines multiple decision trees to produce a more accurate prediction. Each tree in the forest is trained on a randomly selected subset of the training data, and the final prediction is made by averaging the predictions of all the trees. Random forests are often used for classification tasks and are less prone to overfitting than a single decision tree.

The choice of algorithm will depend on the specific problem, the characteristics of the data being analyzed and the resources constraints, since some algorithm need more data and time to learn than others.

2.5.3.2 Unsupervised learning algorithms

Unsupervised learning is a machine learning technique where the algorithm learns from unlabeled data. This means that the data provided to the algorithm does not contain class labels, and the algorithm learns from this data by identifying hidden structures and patterns. The goal is often to discover groups of similar data or patterns in the data. The most commonly used algorithms for unsupervised learning are :

- **Clustering [108]** : Clustering algorithms are used to group similar data together into clusters. Examples include k-means, k-medoids algorithm, and hierarchical clustering [109].
- **Dimensionality reduction** : Dimensionality reduction algorithms are used to reduce the complexity of data by finding a low-dimensional representation that preserves the most important information from the original data. Examples include Principal component Analysis (PCA) [110], matrix factorization [111], and feature selection methods. For instance, dimensionality reduction is often used to visualize high-dimensional data or to speed up the training of machine learning algorithms.

2.5.3.3 Deep learning

Deep Neural Network (DNN) are a type of artificial neural network (ANN) designed to mimic the human brain's neural structure. They are composed of multiple layers of interconnected nodes, called neurons, where each layer processes and transforms input data to generate more abstract and higher-level representations as it moves deeper into the network. The term "deep" in DNN refers to the presence of many hidden layers within the network. Deep neural networks require vast amounts of data and longer training times compared to simpler neural networks. However, the benefit is that they are capable of solving more complex problems and producing more accurate results.

Deep neural networks have revolutionized the field of artificial intelligence in recent years, allowing for breakthroughs in image, audio, and signal processing. The most popular deep neural network algorithms used in mHealth are Convolutional Neural Networks (CNN) and Recurrent Neural Networks (RNN).

Convolutional Neural Networks (CNN)

Convolution Neural Network (CNN) [112] is a type of DNN commonly used for image processing tasks. It is designed to automatically learn and extract features from images by using convolutional filters to identify local patterns and hierarchical structures within the image. CNNs utilize convolutional layers to extract features from an input image and then pass those features through fully connected layers to make a prediction. The convolutional layers are responsible for detecting the patterns, while the fully connected layers use those patterns to make a final prediction. The architecture of a CNN can be outlined as follows :

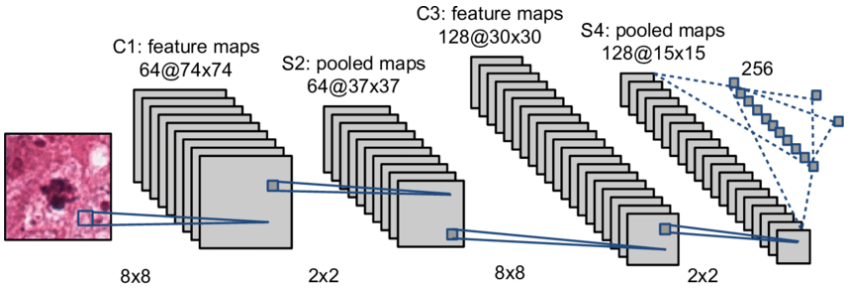

FIGURE 2.6 – An example of CNN, designed in [113] to detect misosis from breast cancer pathology images.

— **Convolutional layers :** In a convolutional layer, a set of filters (also called kernels or weights) are applied to the input image to extract features. The filters are typically small in size (e.g., 3x3 or 5x5), and each filter slides over the input image to perform a dot product at each location, resulting in a feature map. After each convolutional layer, an activation function (such as ReLU) is applied element-wise to the feature map to introduce non-linearity. The output of the activation function is then passed on to the next layer. The ReLU function is defined as $ReLU(x) = max(0, x)$.

— **Pooling Layer :** In a pooling layer, the feature map is downsampled by taking the maximum (max pooling) or average (average pooling) value within a small window (e.g., 2x2 or 3x3). This reduces the spatial dimensions of the feature map and helps to make the model more robust to variations in the input.

— **Fully Connected Layer :** After several convolutional and pooling layers, the feature map is flattened into a 1D vector and passed through one or more fully connected layers. These layers perform a dot product between the feature vector and a set of weights to make a final prediction.

Overall, CNN has been widely used in mHealth for various tasks, such as image classification for disease detection [113], object detection, and segmentation [114], as well as voice processing for Parkinson's disease identification [115], among others. Despite its power, this tool still requires a good understanding of the input data to guide the choice of network architecture design. Figure 2.6 presents an example of a CNN architecture.

Recurrent Neural Network (RNN)

A Recurrent Neural Network (RNN) [116] is a type of artificial neural network that are specially designed to processes sequential data. Unlike traditional feedforward neural networks that process input data in a single pass and forget previous inputs, RNN can remember past inputs, making them suitable for tasks that involve sequential data such as natural language processing, speech analysis, and time series prediction [117]. However, they can have difficulty training on long sequences due to the "vanishing gradient problem" [118] where gradients become increasingly small as they move through the network.

To solve this issue, advanced RNN architectures like Long Short-Term Memory

(LSTM) [119] and Gated Recurrent Unit (GRU) [120] have been developed. These architectures are able to selectively retain or discard information over time, allowing them to handle long sequences more effectively. In the context of mHealth, LSTM (Long Short-Term Memory) has been proven to achieve higher accuracy in detecting heartbeats from accelerometer readings taken by smartphones held by users, as compared to traditional methods of signal processing [15].

2.6 Conclusion

In this chapter, we have laid the groundwork for mobile health. Initially, we discussed the technical capabilities of smartphones (Section 2.1), which are fundamental to our proposed solutions. Subsequently, we highlighted the inherent challenges in health systems reliant on smartphones (Section 2.2). We also delved into the various components essential for designing such systems (Section 2.3). Finally, we explored some of the most commonly used techniques for data sensing and processing in mHealth, as outlined in Sections 2.4 and 2.5.

From this introduction, it becomes apparent that the field of mHealth is rich in contributions, both in the diversity of proposed systems and in addressing various health-related issues. Moreover, it encompasses a range of knowledge from orthogonal domains such as physical models, signal processing, advanced mathematical tools, and IoT systems. However, the methodology for designing these systems remains unclear. Specifically, what steps should be taken to transition from a well-defined health issue to a functional mHealth system that meets the constraints of user-friendliness and hardware availability ? In the next chapter, we will present a methodology addressing this question. Subsequently, we will leverage this methodology to develop solutions—SmartPhOx, Bands-Spi, and Droplets—to address the issues discussed in section 1.4.

Chapter 3

Methodology for Designing an Effective mHealth System

The previous chapter provides an overview of the mHealth field, and the various studies that have been carried out. However, most existing work in this field does not meet our vision for continuous and accessible healthcare. In fact, as presented in the architecture (Section 2.3), the developed systems often rely on additional hardware, which is often expensive or difficult to access, such as external sensors [36] or parts made by 3D printing [9]. In other cases, they rely on sensors found in high-end devices, such as LIDAR [22] or force touch sensors [121]. Moreover, the developed usage protocols are often complex, resembling true laboratory experiments, which can be prohibitive for home use[122, 123]. Either the patient must adopt a strictly defined posture, or the technologies, being mostly proof of concepts, prioritize system efficiency over protocol simplicity. This leads to tools that seem more suited for experts, considering the knowledge required for effective use.

In order to realize our vision, mHealth solutions should fulfill three criteria :

1. **Effectiveness :** First, beyond being a proof of concept, the system should be reliable enough to provide real added value to the user. In addition to comparable accuracy to clinical instruments, it should be able to guide an untrained user in obtaining such results, even in an uncontrolled testing environment.
2. **Accessibility :** Second, they should rely on the sensors present in a standard smartphone, limiting the use of additional hardware to objects readily or easily available for the user.
3. **Simplicity :** Thirdly, the operating protocol must be simple enough for an untrained user to use outside the laboratory. Ideally, it should not require the active participation of the user.

To design mHealth solutions meeting these criteria, the methodology we propose in this chapter combines well-established mathematical principles that describe natural phenomena, around which a basic model is built, signal and image processing techniques for dealing with sensing noise, and machine learning algorithms, all within a data-driven design framework. The systems presented later in chapters 4,5,6 are built following this methodology.

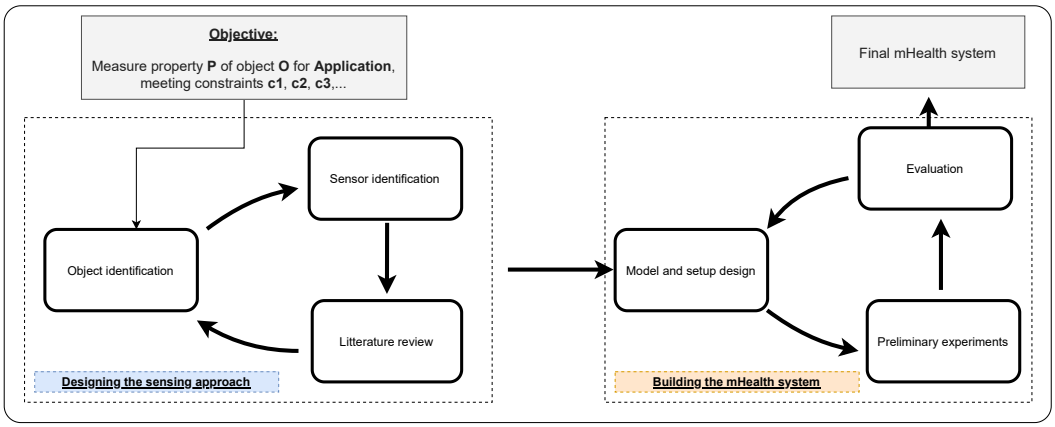

FIGURE 3.1 – **Methodology for building a mHealth system from a well formulated objective** Starting with the formulation of the objective, we identify the object of interest and the relevant sensor, then review the literature in search of relevant object's data sensing approach. Based on the determined approach, we then build the mHealth system using a data-driven iterative process.

3.1 Overview of the methodology

Let us define the purpose of an mHealth system as the calculation of medically relevant information, referred to as "information of interest," using a smartphone. This information can represent a property of an object related to the human body, such as blood oxygen levels or protein levels in urine. It can also pertain to an object outside the body but with an impact on health, such as the alcohol content in a beverage about to be consumed.

No matter the specific health issue (disease screening problem, sample testing, or vital parameter measurement), we assume that the objective can always be formulated in this manner. Thus, the goal is to create a comprehensive system, including setup, usage scheme, and algorithms, based on the appropriate physical law (referred to as the *model*) to estimate the "information of interest" from data collected by the smartphone sensors. We follow two main steps to achieve this.

First, we design the data collection approach. Second, through an iterative process of experimentation and analysis, we construct the mHealth system, addressing challenges that may arise along the way. The methodology is depicted in Figure 3.1.

3.2 Designing the sensing approach

First, we need to design the way to collect object-related data using the smartphone. This involves specifying the setup, even though it may be modified later, as the solution design progresses. To achieve this, the following steps can be taken :

1. **Identify the object and the property of interest :** The first step is to identify the object of interest, which is inherent in the definition of the information of interest as a property. Specifically, the object of interest is the smallest physical unit that can contain the information of interest. For example, it could be blood, lungs, or urine.

Additionally, it is important to clearly define the requirements of the final system as constraints to be fulfilled. By doing this, we can restate the objective as follows :
Objective : We want to measure the property p of object O for a specific *application*, while respecting the constraints $c_1, c_2, c_3, \ldots$
The term *"application"* here refers to what we do with the medical information. Recall from Section 2.3.2.3, it can be simply obtaining it, as in vital sign monitoring systems, or, in other types of systems, interpreting it to extract a clinical meaning.
The constraints represent the desired level of requirements, including the availability of the setup, the user comfort and system accuracy and convenience, as discussed in detail in Section 2.2.

2. **Identify the sensors :** The next step is to identify sensors, present in a smartphone, that can capture data *directly or indirectly* related to the object. We can consider how humans interact with the object through their senses to find suitable sensors. For example, we can detect an individual's heartbeat by either visually observing their chest movement or feeling the displacement when touching the chest. This suggests that the camera and the motion sensors of the smartphone could also capture heartbeat that way. Similarly, we can notice changes in blood flow by observing a person's face color [1], indicating that the camera can capture this information as well. This also give the intuition about the usage scenario, since the sensor has to be placed accordingly.
3. **Literature review :** Thirdly, we conduct a literature review related to the object, the sensor, and the desired property. The objective is to jointly identify a way to measure data related to the object using the selected sensor, as well as an appropriate model to deduce the property of interest from the collected data. To achieve this, the following approach is suggested :
(a) *Which data of the object can be measured with the sensor ?* This involves examining existing studies that enable object's data collection using the specific sensor, whether it is used through a smartphone, another device, or independently.
(b) *What is the relationship between these data and the desired property ?* For each considered data, the physical law that explain the relationship between the property of interest and the data is investigated. For instance, we build up on Beer-Lambert law [29] to build SmartPhOx (explained in Section 4.2.1). It is mathematical model widely used to determine the concentration of a solute in a solution by measuring its absorbance at a specific wavelength. Similarly, BandS-Spi and Droplets are built upon the Boyle-Mariotte law and the Young-Laplace equation, respectively.
(c) *Synthesis* The objective is to compare the identified approaches to select the most relevant one for constructing our system. The comparison criteria to be considered, in order of importance, are **the accessibility of the required setup**, **complexity of the usage scheme** and **expected accuracy of the model**.

1. We can notice a flushed or rosy appearance of the skin of a person's face when he is stressed, which is caused by increased blood flow

3.3 If there is no existing relevant sensing approach ?

If there is no existing approach relevant to the sensor and object being considered, an initial design effort is required to create a new approach. There are two strategies to consider : changing the sensor while keeping the object, or changing the object while keeping the sensor.

Changing the object : The idea is to find another object whose property is influenced by the property of the original object. For example, one could explore the correlation between glucose levels in saliva and glucose levels in the blood. The goal is to identify a more accessible object and then repeat the previous steps 3 of Section 3.2. It should be noted that this strategy requires additional effort in designing the model, as a connection needs to be established between the original property and the measured property of the new object. Learning based approaches are often well suitable for modeling such cases (discussed in 2.3.2.1).

Changing the sensor : Find a different sensor that can provide data more closely related to the object. The focus here is on prioritizing signal-to-noise ratio and being less concerned about additional hardware requirements and use scenario simplicity. Therefore, it is possible to consider external hardware, potentially connected to the device via a cable or wireless technologies.

3.4 Designing the mHealth system–A data-driven approach

After determining the sensing approach, the next step involves building the mHealth system based on a data-driven approach. This process includes refining the model and setup through iterative experimentation, as shown in Figure 3.2.

First, the setup of the chosen approach is customized to fit specific requirements related to the objective. Then, a series of initial on-field experiments is conducted to collect both ground truth data (using the clinical device) and data measured by smartphones. These collected data are preprocessed and input into the model to generate preliminary results. Any challenges or factors contributing to unsatisfactory outcomes are carefully analyzed at this stage. Based on these insights, proposed solutions are developed to refine the usage protocol, setup, and algorithms. This leads to further experimentation in an iterative process until the final system achieves optimal convergence. The challenges we may face include limitations of the model and low data quality.

3.4.1 Dealing with model limitations

The results may be unsatisfactory due to the model's imprecision, which can manifest in two main ways.

— Firstly, for the model to work effectively, it requires ideal experimental conditions, which are often not achievable in our context. The testing environment is uncontrolled, and user actions can introduce sources of error. For example, factors like temperature stability, lighting conditions, or user positioning can significantly impact the model's performance. To address these issues, we can consider two stra-

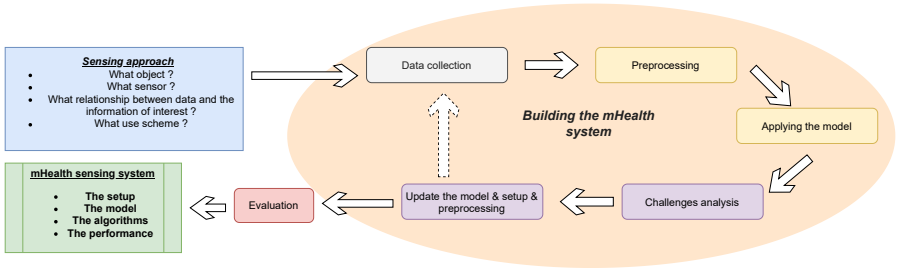

FIGURE 3.2 – Iterative data-driven process for designing the mHealth system.

tegies : using an additional sensor to measure external factors and adjusting the model accordingly, or guiding the user to improve experimental conditions. In the latter case, we aim to design a virtual assistant to help the user make necessary adjustments, ensuring more reliable data for the model.

— Secondly, the model itself may lack precision, leading to discrepancies between expected and observed outcomes. To tackle this problem, we can employ a hybrid approach to complement the model. As described in section 2.3.2.1, this involves using machine learning algorithms to compensate the differences between expected and observed results. The resulting hybrid model is then tested in new experiments to verify its effectiveness.

3.4.2 Dealing with insufficient data quality

Insufficient data quality can arise due to limitations of sensors, environmental noise, or user behavior. For example, when using contacless photoplethysmography (which involve using the front camera to sense blood flow from the face of the user, discussed in Section 2.4.3) to capture blood flow with a camera, factors like device resolution, unintended head movement, and ambient illumination can affect the accuracy of the results. While we can deal with user and environment noise as explained in Section 3.4.1, to address limitations from the sensors, we may design a suitable data preprocessing algorithm. This involves identifying the specific limitation of the sensor. For instance, in order to use the smartphone's camera to measure blood oxygen levels, the RR map introduced in Chapter 4.6.2 is designed to address the difference in light propagation between the larger camera sensor and the pinpoint photo receiver in a pulse oximeter.

3.5 Conclusion

In this chapter, we propose a methodology for designing an mHealth system to address a specific health problem. The process begins by defining the desired medical information. We then identify the object of interest and the sensors capable of measuring it. Next, we conduct a literature review of relevant data measurement techniques, comparing them based on signal-to-noise ratio (SNR), hardware and use requirements, and the presence of a model in the fundamental sciences that links the desired information and the measured data. Once the approach is determined, we proceed to adapt the setup, collect data in the

field, and analyze the initial results. This step helps identify any limitations of the model, setup, or experimental protocol. Based on these findings, we design and adjust the various system components, and repeat the experiments until we achieve a satisfactory system.

Following this methodology, we looked at three application cases, either for measuring a vital parameter, conducting a medical screening, or performing a sample test, all in an accessible manner for non-expert users, using common sensors. We provide detailed descriptions of these systems in the following chapters.

Chapter 4

Blood Oxygen Level Sensing With a Smartphone

"*... A vast majority of Covid pneumonia patients I met had remarkably low oxygen saturations at triage — seemingly incompatible with life — but they were using their cellphones as we put them on monitors.*"

What if their cellphones could have measured their oxygen saturation, how many of these patients would have avoided intubation ?

In this chapter, we present SmartPhOx, a smartphone-based pulse oximetry designed to provide a solution to this question. To design SmartPhOx, we build on the ratio-of-ratios (RR) method and linear regression, an elegant approach resting on the Beer-Lambert law and landing itself to efficient smartphone implementations. However, its implementations without specialized hardware have so far proved to be unsuitable for clinical use, in particular due to the instability of the RR measurements. We use an empirical study to shed light on the reasons why and propose using the very RR measurements to filter RR measurements – a new paradigm we call Meta-ROI. We design a complete-system architecture, including a novel data structure for storing and defining consistent RR values and an efficient algorithm for identifying Meta-ROI in real time. Results from an Android implementation of SmartPhOx with the participation of 18 participants with different skin pigmentation as classified by the Fitzpatrick phototyping scale show that it is the first solution to meet the FDA requirement for Root Mean Square Error (RMSE) without using custom hardware.

4.1 Introduction

As the world was gripped by the COVID-19 pandemic, terms like oxygen saturation (SpO2) and silent hypoxia– the condition in which a patient still feels well but their SpO2 is dangerously low [124] – entered the mainstream. The pulse oximeter, the once-obscure fingertip device allowing home monitoring of the blood oxygen levels, emerged as an important tool in fighting COVID-19, drawing attention to the science and technology behind it – and raising the question of whether it can be reinvented for the era of the smartphone.

The idea of pulse oximetry – the non-invasive monitoring of oxygen saturation using the so-called ratio-of-ratios (RR) method – dates back to 1935 [125]. Scientifically it rests on the Beer-Lambert law stating that light going through a thin body part, like a finger or earlobe, will be impacted by its thickness and concentration – the latter including oxygen saturation. Using two light beams of specific wavelengths and the fact that at different points of the cardiac cycles only oxygen saturation-related factors change, as we show in detail in Section 4.3, it is possible to manipulate the Beer-Lambert law through two consecutive ratios to remove non-oxygen saturation factors, like the medium thickness. The result is a relation between a *ratio-of-ratio (RR) of light measurements* and the SpO_2 – *the ratio-of-ratios (RR)* method [126]. The first pulse oximeter was developed in the '70s [127] and today a wide range of pulse oximeters can be found off-the-shelf [128-132]. Nevertheless, dedicated hardware adds extra burden and, as the silent hypoxia cases due to COVID-19 have revealed [124], often people are not aware their oxygen level needs monitoring.

Increasingly in people's hands and with advanced sensing, computing and communicating capabilities, the smartphone is seen as a building block of pervasive computing and key enabler of the digital healthcare [133-136]. Researchers have proposed smartphone-based pulse oximetry solutions predating the COVID-19 crisis. [137] was among the first to apply the RR method for estimating SpO2 using smartphones. A user places the finger over the flashlight – serving as the source of light – and the camera. Acquiring the photoplethysmogram (PPG) signal from processing the resulting video allows RR of light measurements and the estimation of SpO2. However, its accuracy is below the FDA clearance threshold [30]. The fundamental reason is that it uses linear regression for implementing the RR method. Unfortunately, the PPG signal, and thus the RR measurements, can be unstable due to finger movements and pressure changes [138]. To address this issue, [139, 140] integrate into the RR measurements the camera quantum efficiency. While improving accuracy, this is information to which only manufacturers have access. PhO2 [138] proposes attaching to the smartphone camera a custom-made device mounted with two chromatic filters, each allowing a precise wavelength to pass. The result is a system allowing SpO2 predictions with accuracy meeting the FDA clearance threshold. Nevertheless, the custom-built hardware add-on, while manufactured with the help of 3D printing, limits its large-scale application. Recently, dedicated oxygen monitoring sensors are being integrated in smartwatches [141], and some high-end smartphone models [142]. While accurate, such solutions leave out large sections of users with older smartphone models, particularly in developping countries.

In this chapter, we introduce SmartPhOx, a smartphone-based pulse oximetry system meeting the FDA clearance threshold [30] for accuracy while relying only on the standard smartphone camera and flashlight. Following the methodology presented in Chapter 3, we start by first designing and conducting an empirical study aimed at shedding light on the underlying reasons behind the inaccuracy of existing approach, based the Beer-Lambert law and finger photoplethysmography. The data shows that focusing on primary factors – the quality of the PPG signal [139, 140, 143] or identifying the right region on the video [137, 144], known as the region of interest (ROI) – is misleading.

We find that signals of excellent quality can still lead to unstable RR measurements. Focusing on a particular area of the video frame, such as the center, does not help either.

In light of these results, we argue for a shift in approach. We propose foregoing the primary factors and instead leveraging the RR measurement values themselves for identifying stable RR measurements.

Using RR measurements to essentially filter RR measurement leads to the idea of Meta-Region of Interest – Meta-ROI, the key innovation underpinning SmartPhOx. However, transforming the Meta-ROI idea into a complete system solution running on off-the-shelf smartphones raises several challenges. First, using RR measurements to filter RR measurements requires defining what is a good RR. Second, once the good RR defined, we need an approach for automatically identifying the good RR values using camera videos as input and the processing capabilities of off-the-shelf smartphones. In short, we address these challenges by introducing a new data structure for RR measurements, we refer to as the RR Map, and an efficient algorithm that can identify the Meta-ROI.

Throughout this work, we make the following contributions :

— We show that the primary factors for filtering ratio-of-ratios measurements are misleading. We shed light on the reasons why and introduce Meta-ROI – a new paradigm for identifying good RR measurements (Section 4.4).
— We design SmartPhOx, a complete-system architecture leveraging the concept of Meta-ROI for smartphone-base pulse oximetry (Section 4.5).
— We introduce a new data structure for RR measurements, the RR Map, that enables the definition of good RR values (time-and-space consistent) (Section 4.6.2). Leveraging it, we develop an efficient algorithm for identifying Meta-ROI (Section 4.7).
— We implement SmartPhOx as a standalone Android application and evaluate it with data collected from 37 volunteers. The results show that SmartPhOx is the first pure camera-and-flashlight smartphone-based solution to meet the FDA requirement for Root Mean Square Error (RMSE) [30] (Section 4.9).

4.2 Background on SpO2 sensing

Prior works on pulse oximetry can be grouped into two major categories : a) Works and systems using dedicated hardware dating back to the 1930s, b) More recent works built around the smartphone.

4.2.1 Dedicated hardware-based blood oxygen level sensing

A pulse oximeter is a small portable device for noninvasive monitoring of a person's oxygen saturation in the blood. The idea dates back to 1935 [125], with the first pulse oximeter based on the ratio of red and infrared light absorption developed in the '70s [127]. Today, pulse oximetry remains an active area of research and development, leading to a plethora of devices that can be attached to the fingertip [128-130], earlobe [131, 145], forehead [132, 146, 147], trachea [148] and ring type [149] products. Despite the easy access to pulse oximeters, dedicated hardware can be impractical in everyday life, not least because, as the COVID-19 pandemic revealed, often people are not aware their oxygen level needs monitoring.

4.2.2 Smartphone-based blood oxygen level sensing

Recognizing smartphones as powerful sensing devices already in people's hands, researchers have proposed harnessing their capabilities for vital signs monitoring [134-136]. In the particular case of oxygen saturation, [137] was among the first to apply the ratio-of-ratios method for estimating SpO2 using a smartphone. The RR values, a feature computed from the photoplethysmogram, are extracted over a 50x50px region of interest (ROI) at the center of the frame. However, as our experiments showed (Section 4.4.3.2), computing RR values off a particular physical frame area can lead to inaccurate SpO2 values. To address this issue, [139, 140] integrate into the RR calculation the camera quantum efficiency, which represents the sensitivity of each channel (red, green, blue) of the image produced by the camera to the different wavelengths of the input light. While accurate, these solutions require knowledge of the camera quantum efficiency – something to which only manufacturers have access. PhO2 [138] proposes to attach to the smartphone camera a custom-made device mounted with two chromatic filters, each allowing a precise wavelength to pass. The result is a system allowing SpO2 predictions with very good accuracy. Nevertheless, the custom-built hardware add-on, while manufactured with the help of 3D printing, limits its large-scale application. Recently, dedicated oxygen monitoring sensors have been integrated into smartwatches [141, 150, 151], and some high-end smartphone models [142, 152, 153]. While very accurate, such solutions leave out a large section of users who have older smartphone models, particularly in developing countries.

4.3 Primer on the ratio-of-ratios (RR) method

In this section, we introduce the ratio-of-ratios (RR) method widely used for smartphone-based pulse oximetry [137-140, 144, 154] and adopted by SmartPhOx.

4.3.1 Theoretical underpinning

The RR method for measuring SpO2 rests on the law of Beer-Lambert describing the attenuation of light as a function of the traversed material. Mathematically : $I(\lambda) = I_0(\lambda)\exp^{-\varepsilon(\lambda)\rho d}$, where $I_0(\lambda)$ is the incident light intensity, $\varepsilon(\lambda)$, the absorptivity for the wavelength λ, ρ, the medium concentration and, d, the path length through the medium. The equation can be expressed in a form landing itself to practical systems for estimating SpO2. Let us start by expressing it at the two extremes of the cardiac cycle : in diastole, where $d = d_{min}$, and systole, where $d = d_{max}$.Let $I_d(\lambda)$ and $I_s(\lambda)$ denote the corresponding $I(\lambda)$ values. Taking the logarithm of their ratio, we get :

$$L(\lambda) = ln(\frac{I_s(\lambda)}{I_d(\lambda)}) = (d_{min} - d_{max}).(\varepsilon_{O_2}(\lambda)\rho_{O_2} + \varepsilon_{H_b}(\lambda)\rho_{H_b}) \tag{4.1}$$

While more pratical, Eq. (4.1), requires measuring d_{min} and d_{max}. To relax this requirement, we can use the ratio of two values corresponding to two different wavelengths, λ_1 and λ_2 :

$$RR_{\lambda_1,\lambda_2} = \frac{L(\lambda_1)}{L(\lambda_2)} \tag{4.2}$$

– hence the name **ratio-of-ratios**. Recognizing that $Sp02 = \frac{\rho_{O_2}}{\rho_{O_2}+\rho_{H_b}}$, where ρ_{O_2} and ρ_{H_b} denote the oxygen-saturated and oxygen-unsaturated hemoglobin, respectively, and dividing the numerator and denominator of Eq. 4.2 by $\rho_{O_2} + \rho_{H_b}$, we get

$$SpO2 = \frac{\varepsilon_{H_b}(\lambda_1) - \varepsilon_{H_b}(\lambda_2)RR_{\lambda_1,\lambda_2}}{(\varepsilon_{O_2}(\lambda_2) - \varepsilon_{H_b}(\lambda_2))RR_{\lambda_1,\lambda_2} + \varepsilon_{H_b}(\lambda_1) - \varepsilon_{O_2}(\lambda_1)}. \tag{4.3}$$

4.3.2 Ratio-of-ratios on smartphones using linear regression

Equation (4.3) cannot be implemented on off-the-shelf smartphones without knowledge of all the coefficients. However, studies [137, 155] have shown that it can be approximated using a linear model as follows :

$$SpO2 = A \times RR(\lambda_1, \lambda_2) + B \tag{4.4}$$

This equation enables the implementation of the ratio-of-ratio method on any smartphone using linear regression. RR values are measured empirically and used to train a linear regression model for estimating the coefficients A and B.

4.3.2.1 Measuring RR values on smartphones

The RR expression, Eq. (4.2), can be simplified by introducing $\delta(\lambda) = I_s(\lambda) - I_d(\lambda)$. Indeed $\frac{\delta(\lambda)}{I_d(\lambda)}$ is small – the absorbance of the blood changes lightly from systole to diastole. As a result, $RR(\lambda_1, \lambda_2)$ measurements can be made using

$$RR(\lambda_1, \lambda_2) \approx \frac{\frac{\delta(\lambda_1)}{I_d(\lambda_1)}}{\frac{\delta(\lambda_2)}{I_d(\lambda_2)}}. \tag{4.5}$$

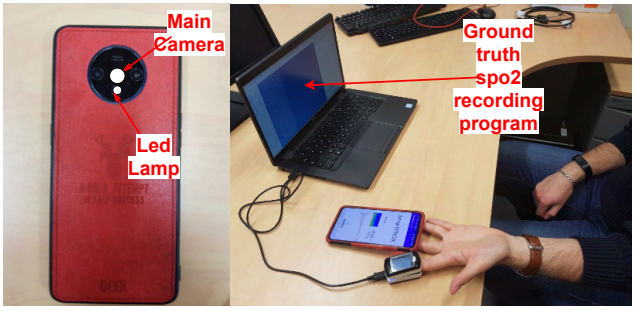

FIGURE 4.1 – Experimental setup

This approximation is significant since measuring systolic and diastolic intensities *per se* is not necessary anymore. We measure instead a base (constant) intensity $DC_{\lambda_1} = I_d(\lambda_1)$ and variations $AC_{\lambda_1} = \delta(\lambda_1)$ over this baseline, significantly simplifying the implementation.

4.4 Smartphone pulse oximetry : Challenges and opportunities

Unlike dedicated pulse oximeters, smartphones use a flashlight covering a wide spectrum (400-800nm [138]) and a high resolution three-channel bitmap camera. Measuring oxygen saturation using a smartphone requires carefully applying the ratio-of-ratios method introduced in Section 4.3.2 on a video sequence. It involves measuring RR [1] values using Equation 4.5, followed by linear regression for estimating the A and B coefficients of Equation 4.4. Therefore, the challenge in accurately estimating SpO2 using a smartphone lies in how the RR are measured, both during training and inference.

4.4.1 Baseline approach for measuring RR

The baseline approach for measuring RR, the basis of most works on this topic [137-139, 144], starts with a video of the subject's finger placed over the camera and flashlight. The average intensity of each channel for every video frame is collected resulting in three PPG signals, one for each channel. The AC/DC ratio is then calculated for each signal : taking as AC the amplitude of the oscillations of the PPG signal, and as DC the baseline of the signal. Taking as λ_1 the red channel and λ_2 the green (or blue) channel, the RR is finally obtained using Equation 4.5.

4.4.2 Analyzing the baseline approach

The objective of this section is not a thorough and large-scale analysis of the baseline approach for measuring RR. It is instead to introduce the simplest test case capable of shedding light on the complexities of the RR measurements on a smartphone and their underlying reasons.

1. For simplicity we write RR instead of $RR(\lambda_1, \lambda_2)$.

Experiment : We design and conduct a controlled experiment using the setup depicted in Fig. 4.1 with three different users exhibiting healthy and stable SpO2 levels (around 99%). Each user sits in a comfortable position and places their hand on a table with the palm facing up. The user's middle finger is placed on the camera of a OnePlus 7T smartphone running a custom application collecting video data, while the index finger is connected to a CMS-50E Pulse Oximeter[128] for establishing the ground truth (more details in Section 4.8.3). We train the linear regression model using the SpO2 variation protocol presented in Section 4.8.2, and test it while SpO2 is naturally constant.

Results : Fig. 4.2 plots the RR values, predicted SpO2 and the prediction errors for all three users. Fig. 4.2a shows that while the SpO2 levels are constant throughout the experiment the RR values are highly unstable. This results casts serious doubts on the feasibility of using Equation 4.4 for estimating SpO2 on smartphones – no values for the A and B coefficients could associate the RR values observed in Fig. 4.2a to the same SpO2 value. It is therefore no surprise that Fig. 4.2b and Fig. 4.2c show highly erroneous SpO2 predictions.

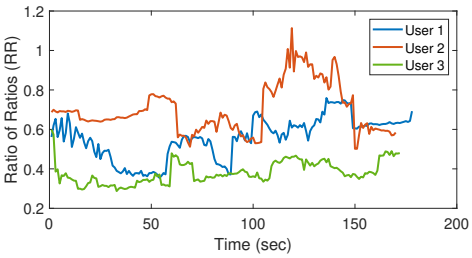

(a) Raw RR values

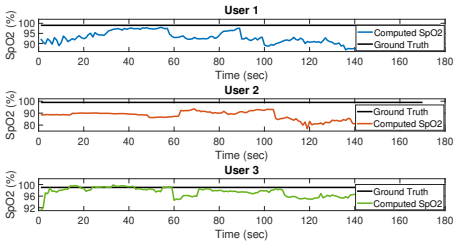

(b) Predicted SpO2

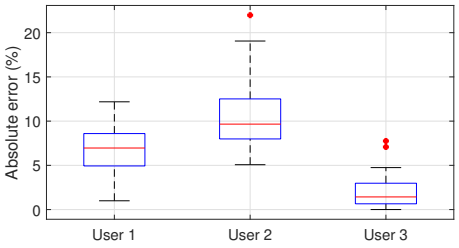

(c) SpO2 prediction errors

FIGURE 4.2 – SpO2 measurements using the ratio-of-ratio (RR) method on three different users exhibiting SpO2 around 99%. The RR values vary significantly (Fig.4.2a) even if the ground truth SpO2 remains constant throughout the experiment – making linear regression extremely challenging. The result is a significant amount of errors in the predicted SpO2 values (Fig.4.2b, Fig. 4.2c).

Implication or the case for consistent RR : This section's test study shows that the ratio-of-ratios method can be undermined by inconsistent RR measurements. Therefore, the smartphone-based pulse oximetry challenge reduces to the challenge of consistent RR measurements. Qualitatively, we refer to RR measurements as consistent if for a given SpO2 level the RR measured using a smartphone are similar.

4.4.3 The quest for consistent RR values

The baseline approach being highly inaccurate due to highly unstable RR values, different approaches have been proposed for acquiring better RR values. Certain approaches

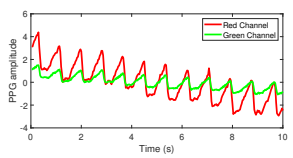

(a) PPG signals (RR = 0.7381)

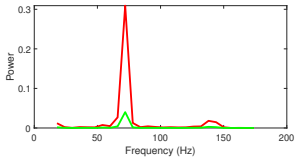

(b) PSD (RR = 0.7381)

Q_{kurt}		Absolute error
Red	Green	5 %
0.95	0.94	

(c) Signal quality and SpO2 error (RR = 0.7381)

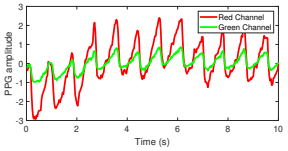

(d) PPG signals (RR = 0.7562)

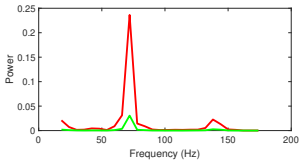

(e) PSD (RR = 0.7562)

Q_{kurt}		Absolute error
Red	Green	6.1 %
0.90	0.92	

(f) Signal quality and SpO2 error (RR = 0.7562)

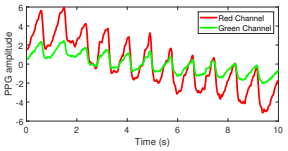

(g) PPG signals (RR = 0.6653)

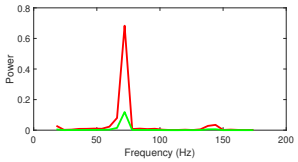

(h) PSD (RR = 0.6653)

Q_{kurt}		Absolute error
Red	Green	0.1 %
0.94	0.94	

(i) Signal quality and SpO2 error (RR = 0.6653)

FIGURE 4.3 – PPG signals off which three RR values of Fig. 4.2 are computed. The signals are very similar in terms of frequency and heart rate evaluation – highest peak around the actual heart rate frequency (72 bpm), with spectrum having very similar shape and Q_{Kurt} values. Nevertheless, the respective RR values are very different, as is the quality of the SpO2 prediction.

have proposed custom add-on hardware [138] filtering the flash light to allow only a precise wavelength. Aiming for solutions without hardware add-on, other approaches have focused on the primary factors behind the RR values. The RR being measured off the PPG signal, most focus has been on the PPG signal quality [139, 140, 143] while some focus on a particular region of the frame [137, 144]. In the following, we investigate the approaches requiring no hardware add-on.

4.4.3.1 The curious case of the PPG signal quality

With the RR a function of the PPG signal, a reasonable direction is to first acquire a good quality signal before applying the RR method. We investigate this approach empirically :

Methodology : To evaluate the relation between signal quality and RR consistency, we look back at the data of Fig. 4.2. We select three RR values – two among those leading to erroneous SpO2 predictions and one among those leading to the accurate SpO2– and analyze the respective PPG signals. Since the source of the PPG signal is the cardiac activity, we use Q_{kurt} in our analysis, a metric quantifying the purity of a signal related to cardiac activity [156]. Specifically, $Q_{Kurt}(s) = \frac{kurtosis(FFT(s))}{kurtosis(P_s)}$, where FFT is the Fast Fourier Transform and, P_s, the perfect sine wave with frequency corresponding to the heart rate.

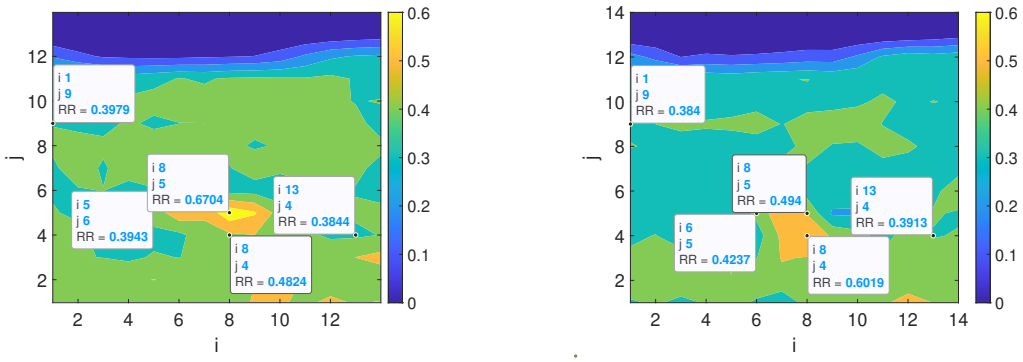

(a) t_1 (b) t_2

FIGURE 4.4 – RR Map at two time instances, t_1,t_2 of the same video collected while SpO2 is constant and equal to 98%. i, and j denote the image cell indices.

Results : Fig. 4.3 shows that the RR values under consideration are computed off excellent PPG signals. The respective red and green channel signals exhibit their highest peaks around the ground truth heart rate (72 bpm). The Q_{kurt} values of all signals are nearly perfect. Nevertheless, the RR values are highly different. More important, two of the RR values lead to erroneous SpO2 predictions.

Implication : While involving only three RR values, the data demonstrates that excellent PPG signals can lead to highly different RR and SpO2 prediction – even if the ground truth SpO2 is constant. As a result, the signal quality can be a poor proxy for consistent RR values. In Sec. 4.4.4, we provide an intuition as to the reasons behind this finding.

4.4.3.2 Location, location, location – and a new (RR) map

Instead of using PPG signal quality, an alternative approach is to simply use the central region of the image for all RR calculations and SpO2 predictions [137, 144]. The intuition being that lighting conditions should be more uniform in this area, leading to consistent RR values.

Methodology : To evaluate the physical location-based approaches, we introduce what we refer to as the *RR Map*. The input frame is divided into *cells* and for every cell a PPG signal and an RR value are computed – the set of all the cell RR values of a particular video input constitutes its RR Map.

Results : Fig. 4.4 shows the RR Map at two different time instances of the data of Fig. 4.2. The data leads to two main observations : First, RR values from a specific region (central or not) can be highly inconsistent – they vary significantly in time and space even if the ground truth SpO2 is constant. Focusing on cells from the central region – (6,5), (8,5) and (8,4) – shows that the respective RR values are very different. Furthermore, they vary significantly from one time instance to the other. A second observation is that RR values from physically-distant cells can be consistent. Zooming in on cells (1,9), (13,4) shows that their respective RR values are very similar and remain stable from one time instance to

the other.

Implications : The RR Map values of cells (6,5), (8,5) and (8,4) underline the difficulty of reliable SpO2 predictions using a fixed region of the frame in particular, and a physical region in general. On the other hand, the fact that the physically distant cells, (1,9), (13,4), have similar and stable RR values is leveraged in Section 4.4.5 for introducing a new way of selecting consistent RR values.

4.4.4 RR (in)consistency – the underlying reasons

The model based on Beer-Lambert's law has some limitations. It assumes that monochromatic light rays pass completely through the finger and are reflected specularly back to the camera, ignoring the complex phenomena of scattering and refraction. Light rays arriving at the camera sensor undergo an optical path that is subject to these phenomena, including intermediary reflections inside the finger, and whose impact can depend on the smoothness of the incidence region and the angle of incidence. It is as if each pixel of the camera is subject to rays following different virtual paths through the finger, producing different RR values for the same SpO2. Furthermore, the temporal volatility of the RRs can be explained by the fact that these virtual paths change, depending on the disturbance generated by the micro-movements of the finger. Some paths are however more stable than others : the paths for which the overall configuration of the finger surface, the camera and the flash do not change much, despite the micro movements. The Meta-Region of Interest introduced in the next section is aimed at identifying the more stable paths.

4.4.5 A way forward – the Meta-Region of Interest

The key observation of our work, paving the way for SmartPhOx's meta-region of interest, is informed by intuition and empirical evidence. Intuitively, while the finger is not perfectly flat and never applied with the same pressure, there must be regions of the fingers for which the light pathways are similar. These regions need not be contiguous in time and space. The intuition is supported empirically by the RR Map of Fig. 4.4 showing cells (1,9) and (13,4), non-contiguous in space, produce similar and stable RR values in an experiment involving a stable SpO2 level. The challenge, however, is automatically identifying the regions leading to consistent RR values. Primary factors, the focus of previous works are shown to fail : PPG signal quality is shown to be a poor proxy ; the areas with consistent RR values are not necessarily contiguous, excluding an approach based on a particular physical area.

We propose to forego using primary factors and to rely on the the RR values themselves to identify good RR values. Using RR values to essentially filter RR values leads to the idea of *Meta-Region of Interest – Meta-ROI*, the central element of SmartPhOx. Turning this idea into a robust smartphone-based solution raises several scientific and system challenges, which we detail and address in the following sections.

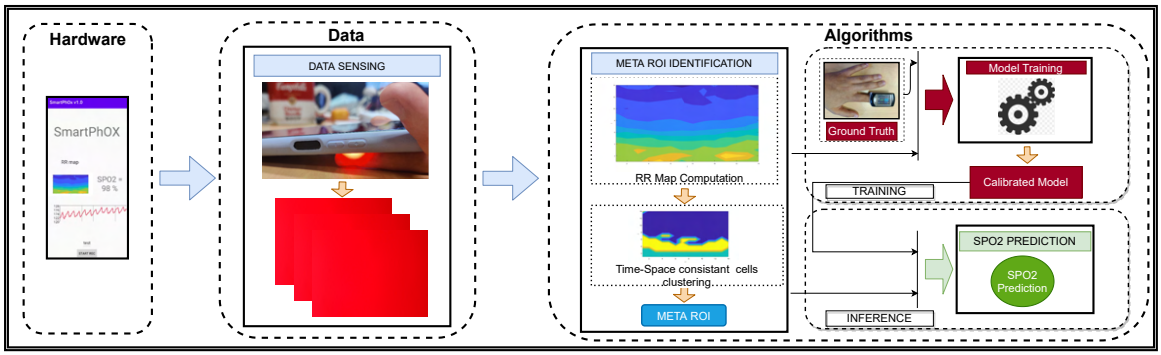

FIGURE 4.5 – SmartPhOx System Architecture

4.5 SmartPhOx system overview

Fig. 4.5 shows a high-level depiction of SmartPhOx 's architecture. It comprises three modules :

1. Hardware : The SpO2 measurement starts with the subject placing the finger on the smartphone flashlight and camera.
2. Data sensing : The smartphone camera generates a video during the measurement session. Section 4.6.2 introduces methods for customizing the video recording and transforming the data into the RR Map.
3. Algorithms : Section 4.7 formalizes the notion of consistent RR values and introduce an algorithm that take as input the RR Map and identifies the Meta-ROI. The latter is used for estimating SpO2 using the ratio-of-ratio method described in Section 4.3.2.

4.6 Data – RR Map Construction

4.6.1 Data sensing

The first step in SmartPhOx is recording a video session while the user places the finger on the smartphone flashlight and camera. Selecting its duration involves satisfying two constraints. It needs to be long enough to allow the calculation of several RR values for identifying time-consistent RR values. And, a single RR calculation requires a few seconds of PPG signal [137, 157]. Let w denote the PPG signal length for a single RR calculation and Z the number of consecutive RR values necessary for training and prediction. SmartPhOx calculates RR values using a sliding window of size w. Thus, the video session duration is $T = Z + w - 1$ seconds.

4.6.2 RR Map computation

Once a video consisting of $30 \times T$ 3-channel (Red, Green, Blue) frames is obtained, the frame surface is divided into $X \times Y$ *cells*. The choice of X and Y represents a tradeoff. Higher values translate to more cells and a finer the segmentation of the frame, enabling a more precise selection of the RR values. However, this leads to smaller individual cells

with less data on their surface, making their RR more sensitive to noise induced by the camera acquisition chain. We evaluate this trade-off in Section 4.9. To compute the RR of a cell from the PPG signal, recall from Sec. 4.3.2 that $RR \approx \frac{AC_{\lambda_1}/DC_{\lambda_1}}{AC_{\lambda_2}/DC_{\lambda_2}}$. Using the green and red PPG signals as λ_1 and λ_2 of each cell, we compute its RR by selecting as AC the standard deviation of the filtered signal, and as DC the average of the raw signal.

For every cell, (x,y), $x \in \{1,2,...,X\}$, $y \in \{1,2,...,Y\}$, we obtain a vector

$$RR^{(x,y)} = \left[rr_1^{(x,y)}, rr_2^{(x,y)}, ..., rr_Z^{(x,y)}\right] \tag{4.6}$$

where Z is the number of RR values computed over the window T. Therefore, the RR Map can be seen as a set of $X \times Y$, Z-dimension vectors, with $X \times Y$ denoting the space dimension and Z, the time dimension. For the rest of the paper, we use the terms *cell* and *Z-dimension vector* interchangeably.

4.7 Meta-ROI Algorithm

The basic premise of our work, as developed in Section 4.4, is that accurately estimating SpO2 requires consistent RR values. In this section, we formalize the notion of consistency and introduce an algorithm for identifying the most consistent RR values – the Meta-ROI.

4.7.1 Space-time consistency in the RR Map

To formalize the notion of RR consistency, first introduced qualitatively in Section 4.4.2, we draw on the empirical study of Section 4.4 and the cluster analysis. With the data showing RR values vary across frame regions and time, we define consistency in space and time. By construction, the RR Map includes the space and time dimension. Therefore, we consider RR cells to be consistent if they belong to the same cluster produced by a clustering algorithm applied on the RR Map. The clusters themselves are considered time-consistent regions. Formally :

Definition 1 (Space-time consistency) *Let $S = \{S_1, S_2, ..., S_k\}$ be a clustering of the RR Map cells. Two cells are considered consistent in space and time if they belong to the same cluster in S. The clusters $\{S_1, S_2, ..., S_k\}$ are referred to as space-time consistent regions.*

4.7.2 Meta-ROI algorithm

In this section, we address the challenge of identifying the *best* among the space-time consistent RR Map regions. Referred to as the the meta-region of interest (Meta-ROI), it includes the RR values SmartPhOx's linear regression model will eventually associate with a particular SpO2 value.

A straightforward solution could be to approach this challenge as fundamentally a clustering problem and simply use an efficient heuristic for k-means. However, owing to its origins as a quantization technique [158], there is no simple way to choose the k

Algorithm 1 Meta-ROI algorithm

Input : $RR\_MAP[X][Y][Z]$
Output : The meta region of interest, $Meta\_Roi$

```
for K := 2 to K_MAX do
    Centroids[K][Z] = k_means (RR_MAP, K)  Compute DB(Centroids[K]), using Eq.(4.8)
    if DB_k < minimum_DB then
        minimum_DB = DB  for i := 1 to K do
            Calculate cv(Centroids[i]) using Eq.(4.7)
        Meta_Roi = cluster with minimum cv
return Meta_Roi
```

parameter. More important, our objective is not to reduce the dimensionality of the RR Map but rather to identify the Meta-ROI.

Our solution to this two-pronged problem is a divide-and-conquer approach. We first address the challenge of identifying the best among the space-time consistent RR Map regions, assuming the k parameter is known. Subsequently, we focus on addressing the challenge of identifying the k parameter.

To identify the best space-time consistent region, we introduce a new consistency metric. The metric needs to satisfy two requirements. It needs to quantify the consistency of a given cell cluster. Moreover, it needs to allow a meaningful comparison of the k clusters with different numerical values so as to identify the Meta-ROI. To meet these requirements, we use the coefficient of variation. It measures the dispersion of a population, allowing to quantify the consistency of a given cluster. And it is normalized, enabling a fair comparison between different clusters. Specifically :

Definition 2 (Consistency metric) *Let $S = \{S_1, S_2, ..., S_k\}$ be a clustering of the RR Map cells and $C = \{C_1, C_2, ..., C_k\}$ the respective set of the Z-dimension centroids. The time-consistency metric of a cluster, S_i, is defined as the coefficient of variation of its centroid vector, $\sigma(C_i)$:*

$$cv_i = \frac{\sigma(S_i)}{\mu_i} = \sqrt{\frac{1}{Z}\sum_{z=1}^{Z}(C_{i,z} - \mu_i)^2} \times \frac{1}{\mu_i} \tag{4.7}$$

$$where\ \mu_i = \frac{1}{Z}\sum_{z=1}^{Z} C_{i,z}.$$

Identifying the best value of the parameter k is a decades-old problem [159, 160] with no simple solution. The naive approach of iterating over different values of k until the consistency metric of Definition 2 is minimized would not work as it could converge to trivial, single-cell clusters. To strike a balance between space-time consistency and region size, we couple the consistency metric with the Davies-Bouldin (DB) index [159], one of the classic validity indices for analyzing clustering. Unlike its main alternative, the

Table 4.1 – SmartPhOx implementation parameters.

w	10 s
T	15 s
RR Map Z-dimension	6
RR Map cell size	94×56 px
Video resolution	1260×720 px

Table 4.2 – SmartPhOx processing time on various phones.

	RR Map computation	**Meta-ROI algorithm**	**Linear Reg.**	**Total**
OnePlus 8t	*27 ms*	*30 ms*	*0.2 ms*	***57.2 ms***
Oneplus 7T	*30 ms*	*32 ms*	*0.2 ms*	***62.2 ms***
Huawei P30	*57 ms*	*86 ms*	*0.5 ms*	***143.5 ms***

silhouette [160] index, which is focused on the cluster density, largely addressed by the consistency metric, the DB index rewards the creation of distinct clusters. Mathematically,

$$DB = \frac{1}{k}\sum_{i=1}^{k} max_{j\neq i}\left(\frac{d_i + d_j}{d_{ij}}\right), \tag{4.8}$$

with k the number of clusters, $d_i(d_j)$, the average (Euclidean) distance of all cells in cluster $i(j)$ from its centroid, and d_{ij} the distance between the centroids of clusters i and j.

The consistency metric and the DB index pave the way for our algorithm for identifying the Meta-ROI (sketched in Algorithm 1). It proceeds by making consecutive calls to a k-means algorithm with increasing values of the parameter k (lines 1, 2) up to a limit of K_MAX. Since the DB index is smallest for well-distinct clusters, the algorithms look to minimize it (line 4). Every time a clustering with a smaller DB index is identified, the consistency metric is used for identifying the best cluster (line 5). The algorithm returns the most consistent cluster of the clustering with the smallest DB index as the Meta-ROI. A key parameter of Algorithm 1 is obviously the K_MAX. In our experiments, the smallest DB index was reached with k between 2 and 6, so we set the default value of K_MAX conservatively to 10.

4.8 Implementation and dataset

4.8.1 Implementation

We implemented SmartPhOx as a standalone Android application. The signal processing component is implemented using the IIRJ library[161]. The k–mean clustering is implemented in Java. Table 4.1 shows the default parameter values used in the implementation (we evaluate the impact of these values on the performance of SmartPhOx in Section 4.9.2). Table 4.2 shows the processing times on off-the-shelf smartphones of the SmartPhOx implementation when using the default parameter values of Table 4.1.

4.8.2 SpO2 variation protocol

Ideally, we would test SpO2 on subjects suffering from hypoxia, especially COVID-19 patients but in the current context it proved infeasible. Therefore, we have developed a protocol for inducing the oxygen level variation in healthy volunteers. The protocol starts with breathing normally for the first 30 s followed by a stop-n-go process of breathing/holding their breath, exhaling/holding their breath. The objective is to induce a gradual decrease and increase of SpO2, thus generating a richer set of values. In particular, the volunteer is asked to take a deep breath and then hold it until starting to feel discomfort, then (b) exhale, followed by holding the breath until feeling discomfort again. At this point the SpO2 reaches its low point, typically in the mid-to-high 80's (%). To raise SpO2 gradually, the volunteer is asked to take a few consecutive short breaths, each followed by holding until discomfort, returning gradually to a normal breathing pattern.

4.8.3 Data collection procedure

To collect the evaluation data, we followed the procedure illustrated in Fig. 4.1 [2]. The volunteer is asked to sit in a chair with their hand resting on the table. A pulse oximeter (CMS50E) is clipped on their index finger while the back camera of the smartphone is placed on the middle finger. The person is then asked to apply the SpO2 variation procotocol, described in Section 4.8.2. The average duration of each SpO2 measurement session is 3 min.

Ground truth To acquire the ground truth data, we use the off-the-shelf CMS50E pulse oximeter[128], which allows measurement of SpO2 in the range of 35%-99% with a resolution of 1% [163]. It is an FDA approved device, widely used in literature for heart rate or SpO2 monitoring [164].

As the oximeter is placed on the index finger while the smartphone on the middle finger, a question arising is whether it is valid to collect the ground truth on a different finger than the one SmartPhOx is using. To address it, we perform experiments with two oximeters placing one in each of the index and the middle finger. We then apply a T-test on the collected data to evaluate the null hypothesis that the pairwise difference between recordings of both fingers has a mean equal to zero at the 5% significance level. The test failed to reject the null hypothesis (p-value = 0.6669 > 0.05), providing support for using readings from index finger as ground truth while SmartPhOx is collecting measurements on the middle finger.

4.8.4 Data set

The data set is summarized in Table 5.1. We evaluate SmartPhOx on 37 participants and using three different smartphones, OnePlus 8T, OnePlus 7T and Huawei P30 Lite. Both Oneplus phones use a Sony IMX586 as main camera sensor, while the Huawei a Sony IMX600y. Their focal lengths are 26mm, 26mm and 28mm, and their apertures f/1.7mm,

2. Our experiments are in agreement with the ethics defined in the Helsinki Declaration [162].

TABLE 4.3 – Data set summary

Age	18 - 60 Average : 30.31 ; Std : 12.37
Gender	Male : 27, Female : 10
Fitzpatrick phototyping scale	I :3, II :20, III : 3, IV : 2, V : 2, VI : 7
Oxygen level	85% - 99% Average : 95.8% ; Std : 3%

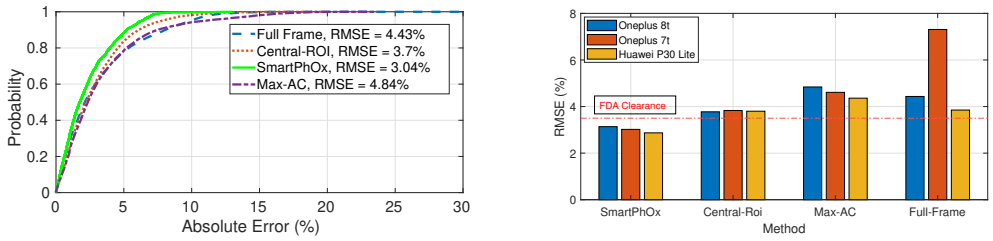

(a) CDF of the absolute prediction error.

(b) Root Mean Square Error (RMSE) by phone model.

FIGURE 4.6 – Overall SpO2 prediction results.

f/1.6mm and f/1.8mm, respectively. To address concerns regarding racial bias in SpO2 measurements, especially as it regards Black patients [165], our study includes volunteers with different skin pigmentation, as classified by the Fitzpatrick phototyping scale [166].

4.9 Evaluation results

In this section, we perform a careful evaluation of SpO2, aimed at understanding its overall performance, the impact of key system parameters and experimental settings, and finally its utilization of system resources.

4.9.1 Overall SpO2 prediction performance

Methodology : SmartPhOx is evaluated using leave-one-out cross validation, with data from 24, 12 and 1 users for train, validation and test sets, respectively. The ground truth is acquired as described in Section 4.8.3. We compare SmartPhOx's meta-ROI with the following approaches for selecting the RR values :

— **Full-frame** : Adopted by several works[138-140, 143], it uses the entire frame as the region of interest. The PPG signals are constructed by stacking in time the average value of every frame for the corresponding channel. The RR values are then computed from the resulting PPG signals.

— **Central-ROI** : It involves using the central 50x50 pixels of the frame [137, 144]. The intuition behind this approach is that the central part of the image should be least impacted by movement or ambient light, and therefore the most stable.

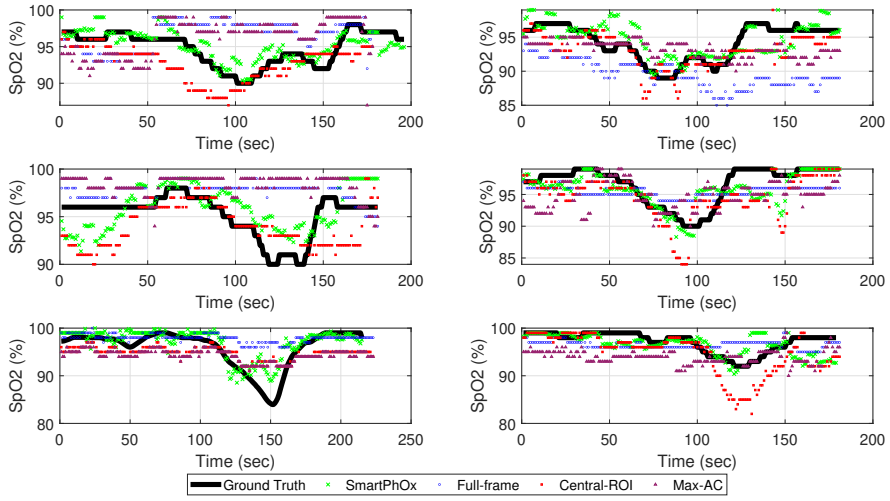

FIGURE 4.7 – Raw SpO2 results for 6 participants.

— **Max-AC** : It involves using the cell producing the largest value of the green channel *AC* [167]. The idea is that blood has a bigger impact on a PPG signal with a large pulse, making it, theoretically, of better quality.

Results : Fig. 4.6 plots the CDF (Fig. 4.6a) and the Root Mean Square Error (RMSE) (Fig. 4.6b) of the SpO2 prediction of all the considered approaches. To put the results into context, Fig. 4.6b includes the FDA RMSE clearance threshold for pulse oximeters [30]. The data shows SmartPhOx having the best performance. The median prediction error for SmartPhOx is 1.75% against 2.2% for the second-best method. The RMSE data paints a similar picture, with SmartPhOx delivering an RMSE of 3.04 % versus 3.77, 4.84, 4.43% for Central-ROI, Max-AC and Full-Frame, respectively. Most important, SmartPhOx is the only approach to meet the FDA RMSE requirement for pulse oximeters [3].

For a look into the raw data, Fig 4.7 shows the SpO2 values reported by all methods during a testing session. In the interest of clarity, we show the data for 6 users. As the subjects are following the SpO2 varying protocol, their levels drop from the healthy values of around 99% to under 90%. The data shows SmartPhOx is capable of predicting the ground truth the best, which is in line with the analysis of Fig. 4.6.

4.9.2 Statistical analysis of the SmartPhOx performance

We conduct a one-tailed T-test on SmartPhOx's prediction errors observed in the experiments of Section 4.9.1. In particular, the statistical test is aimed at answering the question of whether SmartPhOx's prediction error is on average lower than a given value, x. Towards this, we perform a one-tailed T-test over the set of SmartPhOx's prediction errors for various values of x. Fig. 4.8 shows the p-value for different values of x. The data shows that the probability of SmartPhOx's average prediction error being above a given x drops below 0.05 for $x = 2.39$, and below 0.005 for $x = 2.43$.

3. Obviously, this result does not imply FDA clearance, a process beyond the scope of this work.

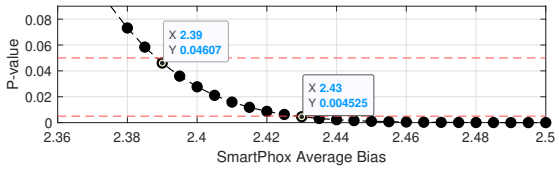

FIGURE 4.8 – SmartPhOx statistical analysis.

TABLE 4.4 – SmartPhOx vs PhO2. The data for PhO2 as reported in [138] .

	PhO2[138]	**SmartPhOx**
Number of Subjects	6	37
Skin pigmentation	Asian : 4, White : 2	Fitzpatrick I-VI
SpO2 range	81 % - 99 %	85 - 99 %
RMSE	N/A	3.04 %
Mean Absolute error, Std Absolute error	2.5 %, 1.62%	2.31%, 1.96%
Absolute error, 80th percentile	3.5 %	3.83 %
Hardware add-on	Yes	No

4.9.3 Comparison with a complete-system solution

In this section, we aim at contextualizing the performance of SmartPhOx by comparing it with PhO2 [138], a state-of-the-art system using the ratio-of-ratios (RR) method.

Methodology : With a full-fledged, in-house implementation of PhO2 being infeasible due to its using a custom-built hardware add-on, we compare with results reported in [138]. For SmartPhOx, we use the same data set and training/validation/testing protocol as in Section 4.9.1.

Results : Table 4.4 compares the performance evaluation of SmartPhOx with that of PhO2. It shows that SmartPhOx's 80th percentile of the absolute prediction error is very close to that reported for PhO2 (no RMSE values are reported in [138]).

Implication : The results show that the meta-ROI approach of identifying regions with consistent RR values introduced by SmartPhOx can relax the requirement for custom-built hardware.

4.9.4 Sensitivity analysis

In this section, we evaluate SmartPhOx's performance as function of its key parameters. The RR Map being fundamental to its functionality, we focus on the RR Map cell size – defining the map's X, Y dimensions – and the RR Map Z-dimension.

4.9.4.1 Sensitivity to RR Map cell size

We vary the RR Map cell size from 32×18 px to 256×144 px. For our implementation using a 1260×720 px video (Table 4.1), this corresponds to an X, Y dimension ranging from 5×5 to 40×40.

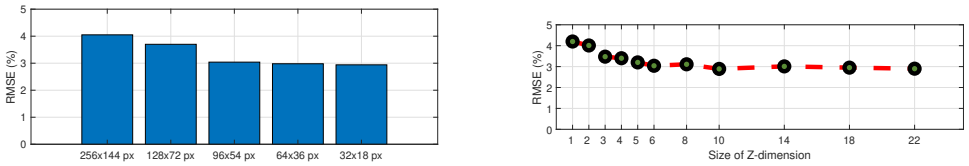

(a) Impact of cell size on SmartPhOx performance.

(b) Impact of Z dimension on the RMSE of SmartPhOx.

FIGURE 4.9 – SmartPhOx sensitivity analysis.

Results : Fig. 4.9a reveals a binary behaviour. For large cell sizes (256×144 px, 128×72 px), the X, Y dimension of the RR Map (5×5, 10×10) is too coarse grained for SmartPhOx's meta-ROI algorithm to identify highly consistent meta-region of interests. However, once the cell size is 96×54 px or smaller the RMSE drops below the FDA clearance threshold. Thus, SmartPhOx uses 96×54 px by default.

4.9.4.2 Sensitivity to the size of Z-dimension

Fig. 4.9b depicts the performance of SmartPhOx in terms of RMSE as function of the RR Map Z-dimension size. The data shows the importance of time consistency, embodied by the Z-dimension, in selecting the best meta-region of interest. When $Z = 1$, essentially eliminating the time dimension, the RMSE is well above the FDA clearance. As the Z-dimension increases, the performance of SmartPhOx improves significantly to meet the FDA requirement. Further, the data shows that once a time-consistent meta-region is identified, increasing the Z-dimension brings no additional gain. As a result, SmartPhOx uses $Z = 6$ as the default value.

4.9.5 Varying experimental settings

In this section, we evaluate the impact of two key experimental parameters in the performance of SmartPhOx : finger on which it measures SpO2, and ambient lightning.

Methodology : With the help of seven of our volunteers, we run SmartPhOx with the smartphone placed successively on the middle, ring and little finger. In a second step, we run SmartPhOx in a completely dark room, with the smartphone on the middle finger. We use two settings for the dark room conditions : in one – Dark room – we use the regressor fitted with the main data set, in the second – Dark room* – we use fit the regressor with data collected in dark room conditions.

Results : Figure 4.10a shows a similar error distribution for all fingers – median error of 1.8, 2.15 and 2.1%, respectively – suggesting that SmartPhOx is robust to the finger selection. We do observe a higher RMSE when using the pinky finger, which may be due to the fact that it is the smallest finger, making the light distribution over its surface more sensitive to random movements.

Fig. 4.10b shows that testing SmartPhOx in a completely dark room does not significantly alter its performance. The data shows that training the regressor with dark-room data (Dark room*) improves slightly the performance of SmartPhOx when compared to normal lighting conditions. This may be due to there being less RR variability in the dark.

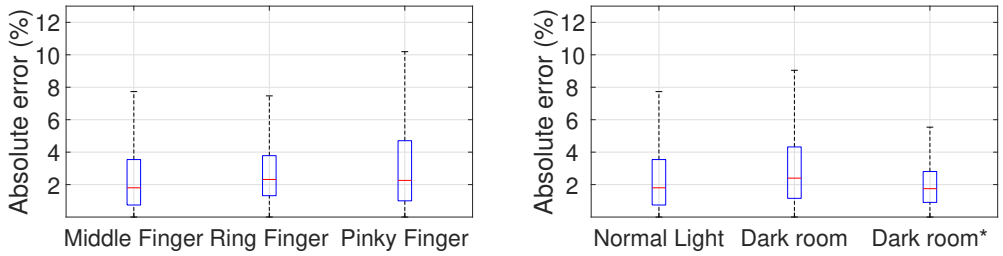

(a) Impact of finger

(b) Impact of ambient light

FIGURE 4.10 – Varying experimental conditions.

TABLE 4.5 – SmartPhOx's resource utilization.

Device	**CPU (%)**	**Memory (MB)**	**Energy (% of time) [L/M/H]**
Oneplus 7t	24	176.9	90/10/0
Oneplus 8t	23	189.3	87/13/0
Huawei P30 Lite	26	298.7	95/5/0

4.9.6 System resources utilization

We evaluate SmartPhOx's utilization of CPU, memory, and energy by using the Android Profiler [168] and report the results in Table 4.5. The intrinsic multiprocessing nature of the mobile phone operating systems makes it very challenging to measure the exact energy consumption of a given application. Thus, we show the percentage of time Android Profiler reports SmartPhOx's energy consumption as being Light (L), Medium (M), or Heavy (H). The data shows that SmartPhOx's utilization of resources is limited, especially in terms of energy consumption.

4.10 Conclusion

We presented SmartPhOx, a smartphone-based pulse oximetry solution requiring no custom hardware. Using a carefully designed empirical study to inform our work, we identified the limitations of current approaches and introduced the notion of Meta-ROI. We transformed the Meta-ROI concept into a complete-system solution capable of running on a smartphone A carefully performance evaluation using an Android implementation of SmartPhOx and involving 37 healthy volunteers showed that it is the first smartphone-base pulse oximetry solution to meet the FDA requirement for Root Mean Square Error (RMSE) without needing custom hardware.

With SmartPhOx, we have developed a SpO2 measurement system that works on any smartphone equipped with a camera and flash. It is designed to be easy and comfortable enough for users, aligning with our vision of accessible healthcare. This system can assist users in taking a first filter in case of doubt about their health state, potentially preventing unnecessary medical attention-seeking. By providing a convenient and reliable tool for measuring SpO2 levels, individuals can proactively monitor their health and make informed decisions about seeking further medical assistance when necessary. There is however many ways to improve this work :

— First, SmartPhOx was trained on a ground truth dataset with oxygen levels ranging from 85% to 99%. This limits the solution's accuracy in predicting oxygen levels below 85%. Obtaining a wider range of ground truth oxygen level data, such as conducting a study in a controlled environment where blood oxygen levels are manipulated by adjusting the oxygen level in the room[169], similar to the approach in [170], could be considered. That been said, SmartPhOx is capable of detecting hypoxia (oxygen levels below 92) and alerting the user to seek medical attention if necessary, which is satisfactory for home monitoring purposes.

— Second, to align perfectly SmartPhOx with this goal, we can explore a contactless and opportunistic approach that utilizes contactless photoplethysmography. As explained in Chapter 2.4.3, this method involves leveraging the front-facing camera of the user's smartphone to monitor changes in skin color caused by blood flow. The approach would intermittently function while the user employs their smartphone, remaining completely passive and transparent to the user. However, this approach presents a significant challenge due to the low SNR, particularly in poor ambient lighting conditions and with darker skin tones. To address this limitation, we can investigate deep learning-based computer vision techniques to enhance the SNR of the contactless PPG signal. Previous research has demonstrated the feasibility of reconstructing finger photoplethysmography from contactless photoplethysmography using a neural network architecture with supervised learning [171], highlighting a promising future research direction for SmartPhOx.

Chapter 5

Measuring Lung Functions with Smartphone and Balloon

"...more broadly, what if the very cellphone already owned could serve as medical device, how easily human being would have access to healthcare?"

In this chapter, we propose BandS-Spi, a solution using a smartphone and an inexpensive rubber balloon for measuring lung function using a spirometry test – a test usually performed in a clinical setting using a spirometer. BandS-Spi is the first smartphone-based system to explicitly measure the air exhaled during a spirometry maneuver by trapping it into a balloon. Its theoretical underpinning is Boyle's law, establishing the relationship between the pressure of the gas inside a balloon and its volume. To transform this theory into a practical system we introduce methods for computing the volume of the exhaled air based on pressure readings collected inside the balloon and introduce a virtual coach for spirometry maneuver quality assurance. We evaluate BandS-Spi on 78 volunteers showing that it can measure the most common spirometry parameters – FVC, FEV1, FEV1/FVC – with accuracy similar to or better than that of commercial handheld spirometers.

5.1 Introduction

Respiratory diseases, such as asthma, Chronic Obstrusive Pulmonary Disease (COPD) and Acute Respiratory Distress Syndrome (ARDS), constitute a significant public health challenge [172]. In 2019, respiratory diseases represented the third leading cause of death worldwide [173]. The most commonly used pulmonary function testing (PFT), Spirometry is recommended by the Global Initiative for Chronic Obstructive Lung Disease (GOLD) for the clinical diagnosis of COPD to avoid misdiagnosis [174]. It is a simple, non-invasive method that measures the volume and velocity of air that can be inhaled and exhaled by the patient.

Traditionally, a spirometry test is performed in a clinical setting using a medical device, a spirometer [175]. A spirometry maneuver involves the patient inhaling deeply and slowly and exhaling forcefully for as long as possible into the spirometer transducer. It is a maneuver described in inherently subjective terms. As a result, a spirometry test involves 2-3 maneuvers under the supervision of a trained technician to ensure repeatability [176, 177].

While the gold standard, clinic spirometry places a significant practical and financial burden on patients with chronic diseases, and can be entirely out of reach for many, especially in the developing world [178]. Against this background, home spirometry, using

portable spirometers, has emerged as a more practical and accessible alternative [179]. A very positive development towards making spirometry more accessible and affordable, it still requires special-purpose hardware, imposing financial and environmental costs. Furthermore, it is more challenging for patients to perform high-fidelity spirometery maneuvers without any coaching. Providing an easily accessible and efficient method of performing this test would help reduce mortality, as well as the costs associated with these conditions. To this end, this chapter investigates an mHealth system for home spirometry testing. We formulate the problem as follow :

Problem : *How to perform reliable spirometry test using a smartphone ?*

The spirometry test essentially involves measuring the volume of gas coming out of the lungs. Furthermore, to make spirometry at home truly possible with a smartphone-based solution, we have to make sure that the user will be able to get reliable results from the system on his own, regardless of its skills and the test environment. Hence, we formulate our objective as follows :

Objective : *We want to measure the volume of the expired content of* ***lungs*** *reliably even in an uncontrolled environment and with and untrained user.*

Following the methodology described in Chapter 3, we identify the object of interest as the lungs, and the property of interest as the volume of exhaled gas.

To identify the sensor to be used, our primary intuition is that we can sense the amount of gas exhaled by an individual by listening to the variation in the intensity of the sound of their exhalation. Based on this insight, we conduct a review of the literature on existing mHealth sensing approaches related to the lungs and the device's microphone.

Review of the state of the art

Gupta et al. [180] introduced one of the first smartphone-based spirometry solutions. While it relies on a custom hardware add-on, limiting its practicality, it showed the potential of the smartphone-based paradigm. Several works followed [10, 39, 181-183], introducing "pure software" smartphone-based spirometry solutions with accuracy comparable to special-purpose medical devices. The underlying principle of these systems is that a spirometry test can be performed by blowing out into the smartphone microphone and processing the audio recordings (See audible sound analysis in Section 2.4.2.1). Citing the sensitivity of these audio recordings to the ambient noise, however, [27] introduced a different approach, SpiroSonic, which measures the lung functions by measuring the chest wall motion of a person performing the spirometry maneuver, using acoustic motion tracking. The latter is performed by transmitting an ultrasound signal using the smartphone speaker and analyzing the signal reflected by the chest wall and received by the microphone (see details about Acoustic motion tracking in Section 2.4.2.2). However, the high level of precision required in the chest wall motion measurements makes SpiroSonic sen-

sitive to unintentional hand movements.

Existing approaches, are in essence either sensitive to the user's unintentional movements, or to ambient noise, which does not satisfy the constraints of our objective. Following our methodology described in Chapter 3.2, we decided to investigate a new approach, involving a more reliable sensor although requiring additional material.

Contribution and plan

Given the limitations of existing approach, we look for a different approach, by changing the sensor. To guide us, our intuition is that we can more faithfully measure a volume by measuring a pressure, since both are correlated. According to Boyle's law [184], the pressure of the gas inside an isolated container is inversely proportional to its volume.

Following this intuition, we propose BandS-Spi, a solution using a smartphone and an inexpensive rubber balloon for measuring lung function using a spirometry test. BandS-Spi is the first smartphone-based system to explicitly measure the air exhaled during a spirometry maneuver by trapping it into a balloon. Smartphones have pressure sensors, so, in theory, placing one inside a balloon to collect its internal pressure should allow computing the volume of the exhaled air trapped inside the balloon. Fig. 5.1 shows the results of a simple feasibility experiment. A smartphone is placed inside a rubber balloon and air is gradually inserted into the balloon using a 300 mL syringe. As we insert specific quantities of air into the balloon, the smartphone pressure readings are recorded to generate pressure-volume curves. The experiment is repeated 3 times, on 3 different days, producing near-identical pressure-volume curves. The repeatability of the results suggests that BandS-Spi's basic working principle is feasible in practice.

To transform this theory into a practical and reliable spirometry system raised several challenges. First, transforming pressure readings into the balloon volume is challenging for several reasons. The volume of the balloon depends not only on the internal pressure but also on other factors, including the number of polymer chains per unit volume (itself depending on the manufacturing process), the balloon thickness, temperature, etc. The volume of the balloon itself is not the same as the volume of the air exhaled into it due to the effect of the rubber's restoring force. Finally, performing a spirometry test without any coaching from a trained technician is challenging and can lead to erroneous results. This is a challenge faced by all home spirometry solutions but presents distinct difficulties for BandS-Spi due to its usage of a rubber balloon. In short, we address these challenges by introducing an approach for converting pressure readings into exhaled air volume that does not require knowledge of the balloon manufacturing process and needs only a single, one-time measurement from the user. To assure at-home spirometry fidelity with BandS-Spi, we introduce a virtual coach whose design is informed by a quantitative analysis. It is capable of automatically detecting the most common sources of errors during a smartphone-and-balloon spirometry maneuver. We evaluate BandS-Spi on 78 volunteers showing that it can measure the most common spirometry parameters – FVC, FEV1, FEV1/FVC – with accuracy similar to or better than that of commercial handheld spirometers.

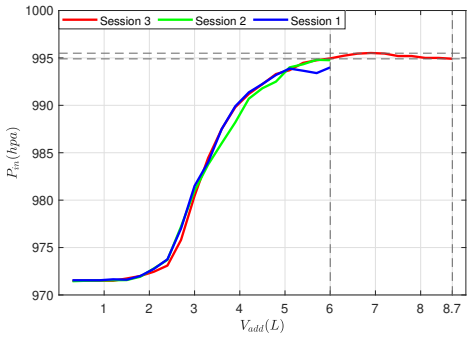

FIGURE 5.1 – Repeatability of pressure-volume curves generated using a smartphone and a balloon, paving the way for SmartPhOx.

The chapter is organized as follow :

— In Section 5.2.1 We present the spirometry test, and in Section 5.2.2 we briefly discuss about existing smartphone-based solutions.

— We present the overview of BandS-Spi in Section 5.3, and detail the procedure to convert volume to pressure (Section 5.4) .

— We describe the virtual coach designed for ensuring spirometry manoevur quality in Section 5.5. Its design is informed by a quantitative analysis discussed in Section 5.5.1.

— We present BandS-Spi implementation result of the evaluation with a cohort of 78 volunteers in Section 5.6

— Finally, we discuss about limitations of the proposed solution and conclude the chapter in Section 5.7.

5.2 Background

5.2.1 A primer on Spirometry

Spirometry measures the volume and flow of air a person can inhale and exhale. It can identify a reduction in respiratory capacity, leading to an early diagnosis of respiratory problems [176, 177].

A spirometry test is performed using a device called a spirometer (Fig. 5.3) and involves several maneuvers. During a spirometry maneuver, the patient places the spirometer transducer in the mouth and breaths in deeply and slowly, followed by a forced and rapid exhalation to expel as much air as possible from the lungs. The test usually includes at least three spirometry maneuvers to ensure results are repeatable [185]. At the end of each maneuver, the device outputs a set of lung function measures. The most common measures are [186] :

1. **Forced Vital Capacity (FVC)**, the total amount of gas exhaled by the patient. An abnormal FVC could be due to a restrictive or obstructive lung disease.
2. **Forced Expiratory Volume in one second (FEV1)**, the volume exhaled during the first second of the maneuver. A lower-than-normal FEV1 reading may be a sign of significant breathing obstruction. A clinician uses the FEV1 measurement to grade how severe any abnormalities are.
3. **FEV1/FVC** is simply the ratio of the first two measures and is also known as the Tiffeneau index. It represents the percentage of the lung capacity the patient is able to exhale in one second. A high percentage is a sign of good health while a low ratio suggests that something is blocking the airways.
4. **Peak Expiratory Flow (PEF)** is the highest exhalation flow during the maneuver. The Peak expiratory flow, if measured regularly, can be used to assess the progression of asthma, and even its response to treatments.

The most common lung function measures in clinical settings are FVC, FEV1, and FEV1/FVC [187].

Normal results for a spirometry test vary from person to person depending on age, height, sex, and sometimes race and weight [188]. Therefore, the clinician first calculates the predicted normal lung function measures values from the patient's demographic information and then compares them to the test results to draw conclusions. In general, a healthy user result is over 80% of the predicted value [188],[189].

5.2.2 Related works and limits

Smartphone-based lung function estimation

Gupta et al. [180] proposed one of the first smartphone-based spirometry solutions. It uses custom spirometer hardware that connects to an Android smartphone. While accurate and showing the potential of using a smartphone, the required hardware add-on limits its practicality.

Several works followed up, aimed at measuring lung functions using the smartphone solely, relying mainly on the exhalation sound [10, 39, 181-183]. In SpiroSmart [10] and SpiroCall[181], the authors process the audio recording of the exhalation sound of a user performing the spirometry maneuver to estimate lung function features. However, due to the complexity of the proposed algorithms, these systems require an external server to operate.

To address this issue, Exhalsense [182] proposes a simpler algorithm also based on the audio recording of the exhalation. They process the recording to detect the forced exhalation segment, distinguish high fidelity effort from poor effort, and apply a machine learning-based regressor to deduce the FEV1/FVC ratio with an accuracy of around 8%. In the same vein, Nazir et Al. proposed to predict FEV1/FVC using only the monosyllabic "Aaaaa.." sound of a user [190]. While these solutions based on audio recordings can be very efficient and accurate, they are inherently very sensitive to ambient noise [191].

To address this issue, Song et Al. proposed SpiroSonic [27], a smartphone-based solution that measures the chest wall motion of a patient performing the spirometry maneuver via acoustic sensing, and then converts the measured motion into the lung function parameters. Although robust to ambient noise, this solution is nevertheless sensitive to user clothes and hand movements. The latter is particularly challenging as it is difficult for a user to exhale vigorously and quickly – as required by the spirometry maneuver– while holding the phone steadily. Aware of this reality, we have chosen to include in BandS-Spi, a virtual coach algorithm, designed to check the quality of the maneuver made by the user, so as to provide him with feedback enabling him to make a reliable measurement.

Spirometry maneuver quality assurance

Few systems have addressed the quality of the spirometry maneuver with a smartphone. In Spiro-Confidence [39], the authors focus on the quality of a spirometry maneuver obtained as an audio recording. They show that their trained Gated-Convolutional Recurrent Neural Network can classify audio recordings representing a good quality maneuver against poor quality ones, with a recall of 88%. Exhalsense [182] also incorporates a classifier that distinguishes high quality from poor quality effort.

BandS-Spi is an environment-resistant solution. It is the first solution explicitly measure the volume of the gas exhaled and, therefore, is unaffected by outside factors, like the unstable movements of a child or a patient with Parkinson's disease. Furthermore, BandS-Spi is one of the few smartphone-based solutions to integrate into its design virtual coaching to ensure lung measures are computed based on properly executed spirometry maneuvers.

5.3 BandS-Spi System Overview

Fig. 5.2 shows a high-level depiction of BandS-Spi's architecture. It comprises three modules :

1. Spirometry hardware : It includes a smartphone running BandS-Spi inserted into a rubber balloon. A cardboard mouthpiece is inserted into the balloon's inflation

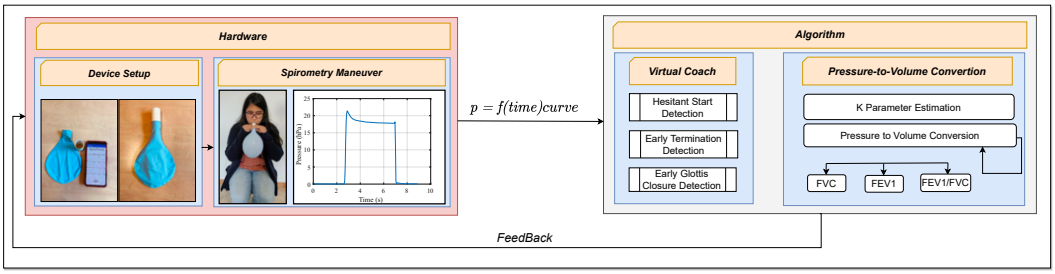

FIGURE 5.2 – BandS-Spi Overview.

FIGURE 5.3 – Medical Spirometer vs BandS-Spi

outlet. The user holds the hardware by the contact surface between the mouthpiece and the balloon, avoiding contact with the balloon body, and performs a spirometry maneuver. It involves the user taking a deep breath and forcefully exhaling into the balloon mouthpiece. The increase in gas in the balloon induces a change in pressure, which is recorded by the smartphone to create a pressure-time curve.

2. Pressure-to-volume conversion : To measure FVC, FEV1 and FEV1/FVC, Section 5.4 introduces BandS-Spi's methods for converting the pressure-time curve produced by the smartphone into a volume-time curve.
3. Virtual coach : Even with careful guidelines, users can perform invalid spirometry maneuvers, especially since BandS-Spi is aimed at spirometry without the supervision of a trained technician. To avoid computing lung function parameters from invalid maneuvers, Section 5.5 introduces BandS-Spi's virtual coach. It introduces methods for the automatic detection of the most common sources of invalid maneuvers.

5.4 Pressure to volume conversion

The output of a smartphone-and-balloon spirometry session is a Pressure-Time curve of the expiration. In this section, we show how BandS-Spi transforms it into a Volume-Time curve, allowing to measure FVC, FEV1 and FEV1/FVC.

5.4.1 High-level approach

During a smartphone-and-balloon spirometry test, the user blows out into the balloon after full inspiration, increasing the internal pressure and causing the balloon to expand.

The smartphone's barometer sensors record pressure readings allowing us to generate a pressure-time curve. To transform the pressure-time curve into a volume-time curve necessary for computing FVC, FEV1 and FEV1/FVC, BandS-Spi follows a two-step process. First, in Section 5.4.2 it transforms an internal pressure reading into the volume of the balloon the moment the reading is collected. This step presents the hardest challenge as the volume of the balloon depends not only on the air blown into it but also on the initial size of the balloon and non-spirometry factors, including balloon fatigue and temperature. The first step is not sufficient, however, as the volume of the balloon is not the same as the volume of the air blown into it due to the effect of the rubber's restoring force. Therefore, in the second step in Section 5.4.5 BandS-Spi addresses the challenge of transforming the volume of the balloon into the volume of the air exhaled by the user.

5.4.2 Computing the balloon volume

Let P denote the pressure inside the balloon and α its relative extension during the test. The latter refers to the ratio between the balloon's inflated, r, and uninflated radius r_0. Our objective is to establish a relationship between P, which BandS-Spi can measure using the smartphone barometer, and α, allowing to compute the balloon volume. To address this challenge, we leverage the pressure-relative extension relation. It can be written [192]

$$P = P_0 + K(\frac{1}{\alpha} - \frac{1}{\alpha^7}), \tag{5.1}$$

where $\alpha = \frac{r}{r_0}$, P_0 is the atmospheric pressure and K is a constant that depends on the balloon and the temperature (see Section 5.4.3). We can solve Eq. (5.1) by minimizing the objective function

$$\arg\min_{\alpha}(P - P_0 - K(\frac{1}{\alpha} - \frac{1}{\alpha^7}))^2$$

in order to get α as funtion of P. Finally, BandS-Spi computes the volume of the inflated balloon as

$$V = \frac{4\pi(\alpha * r_0)^3}{3}. \tag{5.2}$$

Nevertheless, Eq. (5.1) requires knowledge of K while Eq. (5.2) requires knowledge of r_0, the balloon's uninflated radius. We address these challenges in the next two sections.

5.4.3 The balloon K-parameter estimation

The K-parameter in Eq. (5.1) depends on the balloon manufacturing process, temperature and radius of the balloon. It can be written [192]

$$K = \frac{2N_c d_0 kT}{r_0} \tag{5.3}$$

where N_c is the number of polymer chains per unit volume, k is Boltzmann's constant, T is the absolute temperature and d_0 is the thickness of the rubber in the unstretched state.

In Eq. (5.3), N_c and d_0 depend on the balloon manufacturing process, making it infea-

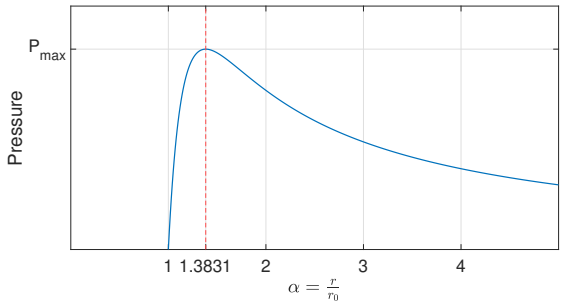

FIGURE 5.4 – $P = f(\alpha)$

sible for BandS-Spi to obtain a universal value for K. Furthermore, even if somehow all the balloons were made following the exact same manufacturing process, K may differ between spirometry maneuvers due to stress softening [193]. Stress softening, also known as the Mullins effect [194], occurs when virgin rubber material is subjected to cyclic loading.

To address this dual challenge, BandS-Spi introduces an approach to dynamically compute K in every spirometry maneuve. We start by re-writing Eq. (5.1) :

$$K = \frac{(P - P_0)}{(\frac{1}{\alpha} - \frac{1}{\alpha^7})} \tag{5.4}$$

While BandS-Spi can measure P using the smartphone barometer, it needs K to compute α. To unpack the interdependency between K and α, we solve $\frac{dP}{d\alpha} = 0$, that is, finding α_m that maximizes P. We have :

$$\frac{dP}{d\alpha}(\alpha_m) = 0 \implies K(\frac{7}{\alpha_m^8} - \frac{1}{\alpha_m^2}) = 0 \implies \alpha_m = 7^{\frac{1}{6}} \tag{5.5}$$

Fig. 5.4 illustrates the finding of Eq. (5.5) and shows that P reaches its maximum value for $\alpha_m = 7^{\frac{1}{6}} = 1.3831$. Eq. (5.5) paves the way for BandS-Spi's method of computing K. During a spirometry maneuver, BandS-Spi keeps track of the pressure inside the balloon and identifies the maximum value of P. Since maximum P is reached for $\alpha_m = 7^{\frac{1}{6}}$, the value of K for the specific maneuver can be computed using Eq.(5.4).

5.4.4 The balloon r_0-parameter estimation

To estimate the balloon's uninflated radius, r_0, BandS-Spi introduces an approach needing a single measurement from the user the first time a balloon is used. The user is asked to spread out the balloon on a surface and measure its greatest horizontal width, l, as shown in Fig. 5.5. Observing that $2 \times l$ is a reasonable estimate of the balloon's uninflated circumference, r_0 is computed as follows :

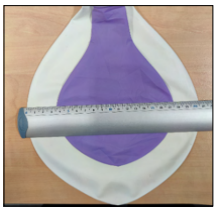

FIGURE 5.5 – r_0 empirical estimation.

$$2 \times \pi r_0 = 2 \times l \implies r_0 = \frac{l}{\pi}$$

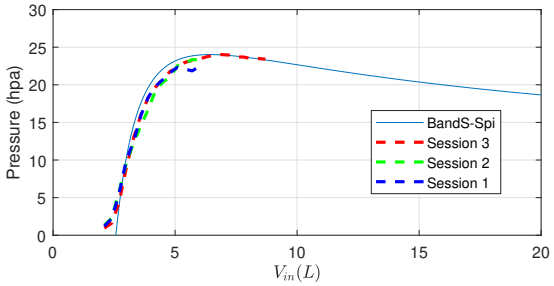

FIGURE 5.6 – The $P = f(V_{in})$ curve as computed by BandS-Spi and directly in three measurement sessions.

5.4.5 Balloon volume to FVC and FEV1

Note that the volume of an inflated balloon V is not the same as the volume of the gas blown into it. According to the Boyle-Mariotte Law [184] (and assuming zero heat exchange), the gas blown from the lungs – with a pressure equal to the atmospheric pressure P_0 at the end of inspiration – into the balloon is compressed under the effect of the rubber's restoring force until it reaches a final pressure P at equilibrium. Therefore, BandS-Spi computes, $V_{exhaled}$, the volume of the exhaled air as follows :

$$V_{exhaled} = V \times \frac{P}{P_0} \tag{5.6}$$

Once the pressure-time curve is converted into a volume-time curve, BandS-Spi can compute the forced vital capacity (FVC), Forced Expiratory Volume in one second (FEV1) and their ratio.

5.4.6 Validation

In this section, we evaluate BandS-Spi's capability to convert pressure readings collected from a smartphone into the volume of the air inside the balloon. To establish a ground truth, we use a syringe to inject a known volume of air into a balloon while a smartphone collects the internal pressure. We repeat the syringe-based experiment three times to create measurement-based pressure-volume curves. In parallel, BandS-Spi runs on the smartphone to estimate the volume and create its own pressure-volume curve. The curves are plotted in Fig. 5.6 and show that BandS-Spi's method for converting pressure readings into air volume is accurate.

5.5 A virtual coach for at-home quality assurance

In this section, we introduce BandS-Spi's virtual coach aimed at helping users perform quality spirometry testing without the help of a trained technician.

In Section 5.5.1, we perform a quantitative analysis of the major reasons leading to errors during a spirometry maneuver, especially when using the balloon-and-smartphone

FIGURE 5.7 – BandS-Spi setup and experimental protocol.

setup. In Section 5.5.2, we introduce how BandS-Spi's virtual coach addresses the problem.

5.5.1 Spirometry Maneuver Quality : a quantitative analysis

In this section, we perform a quantities analysis with the help of 15 volunteers aimed at understanding the major reasons leading to spirometry maneuver errors.

Experimental setup : The experimental setup is shown in Fig. 5.7 and includes a smartphone running the BandS-Spi application inserted in a rubber balloon. A cardboard mouthpiece is inserted into the balloon's inflation outlet. The participants are asked to hold the system by the contact surface between the mouthpiece and the balloon, without any contact with the lower part of the balloon to avoid impacting the inflation.

Spirometry maneuvers : We follow the ATS guidelines [185] for coaching the participants to perform a proper spirometry maneuver. A user takes the deepest breath they can and then exhales into the balloon via the mouthpiece as hard as possible, for as long as possible. At the end of the expiration, the user moves the mouthpiece to the side to expel the air from the balloon, marking the end of the maneuver. In the meantime, we observe and annotate the maneuver, noting the mistakes made and providing corrective instructions. We then ask the user to repeat the maneuver, until a valid one is produced. We collect a total of 64 spirometry maneuvers.

Problem 1 – Hesitant start : In 13 out of the 64 maneuvers the data shows an initial hesitation in blowing out. Sometimes users seem surprised by the pressure inside the ball. Unlike in the classic spirometer, when blowing into a balloon the internal pressure increases, making it more difficult to sustain the effort. If the user does not put enough force into the initial blast they are caught flat-footed by the balloon pushback, resulting in a drop in airflow. The data shows the flow rising again, due to a second effort by the user to reach the end of the expiration. A maneuver showing this error cannot be used for measuring the PEF (Peak Expiratory Flow). Figure 5.8b shows a typical example of the volume curve obtained from a maneuver with a hesitant start while Fig. 5.8a shows an example without hesitation.

Problem 2 – Early termination : In 23 out of the 64 maneuvers the data shows an early termination. Exhalation lasted barely three seconds, when according to the ATS [185] it should last at least six. A maneuver showing this error cannot be used for measuring FVC (Forced Vital Capacity). Early termination occurs even when using standard devices but the balloon pressure adds an additional problem as illustrated in Fig. 5.8c. In this particular maneuver, the end of expiration is reached around 5 s. However, the data shows that the balloon volume, if it is kept inflated, continues to increase. This can be explained by the fact that the rubber balloon takes extra time to find equilibrium after the flow of air is stopped. As Fig. 5.8c shows, stopping the maneuver at the end of expiration and letting the balloon deflate immediately will lead to sub-par precision. Holding the balloon inflated for a few extra seconds reduces the error in FVC computation from 5% to 0.7%.

Problem 3 – Early Glottis Closure : Closing the vocal cords (glottis closure) before the lungs have been completely emptied is a characteristic event of a poor spirometry maneuver and needs to be detected by the technician overseeing the test according to the ATS [185]. It poses a greater challenge to BandS-Spi due to its using a balloon. Our data shows that glottis closure occurred in 9 out of the 64 maneuvers, abruptly stopping the airflow, as illustrated in Fig. 5.8d. As a result, the FVC is underestimated while the FEV_1/FVC ratio is overestimated, potentially leading to an erroneous diagnosis.

5.5.2 Virtual coaching for maneuver quality assurance

In this section, we describe the methods and algorithms BandS-Spi's virtual coach uses for detecting invalid maneuvers in conditions where users do not have access to a trained technician. Users are notified in the case of invalid spirometry maneuvers and provided with the appropriate instructions to avoid making the same mistakes.

5.5.2.1 Detecting hesitant start

A valid spirometry maneuver produces a monotonically increasing flow up to the point of peak expiratory flow (PEF). Therefore, to detect a hesitant start BandS-Spi's approach involves analyzing the smoothness of the initial part of the flow-time curve. The straightforward approach of evaluating signal smoothness usually involves a frequency domain analysis. However, the PEF normally occurs at most 300 ms after the beginning of the exhalation [182], meaning we are dealing with a signal of 300 ms sampled 25 times per second. With a signal of this size, frequency analysis is unhelpful.

Therefore, BandS-Spi introduces an approach based on a novel metric, Q_{hes}, quantifying the smoothness of the initial flow-time signal relative to a reference signal.

Let $F = f_{i\,i=1\ldots n}$ denote the set of instantaneous flow values until they reach the PEF, where f_n is the maximum flow value measured. This set is obtained by the discrete derivation of the volume curve. A hesitation-free maneuver start should produce a linear set F. To quantify the linearity of the measured flow values, we utilize Pearson's linear

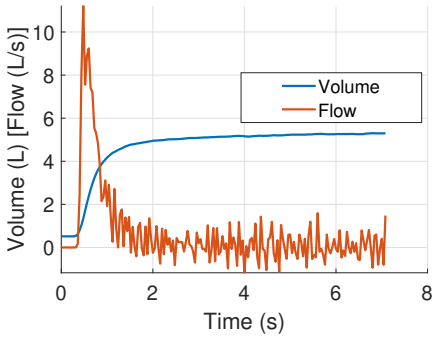

(a) Example of a good Spirometry maneuver.

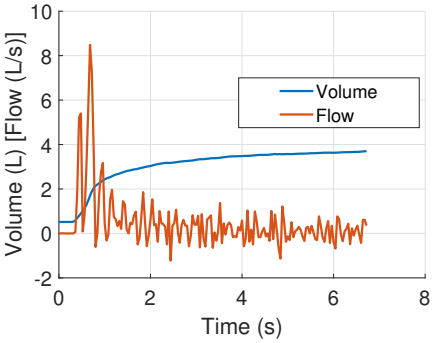

(b) Example of a maneuver with a hesitant start.

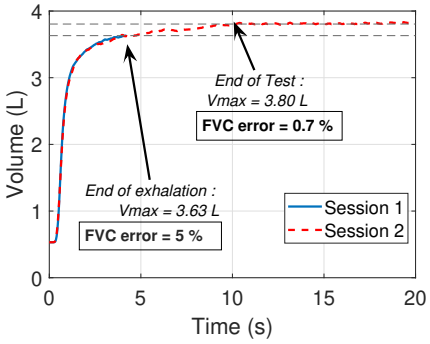

(c) Example of a maneuver with an early stop.

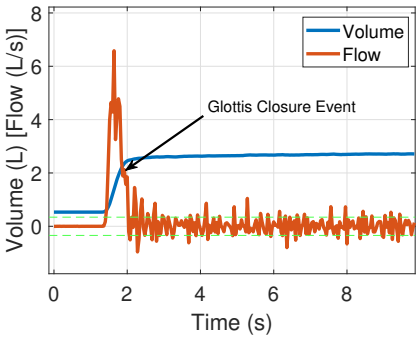

(d) Example of a maneuver with a glottis closure.

FIGURE 5.8 – Illustration of data obtained from perfect maneuver vs hesitant start maneuver, early stop and early glottis closure maneuvers.

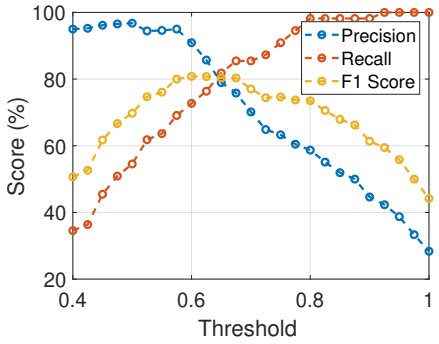

FIGURE 5.9 – Hesitant start classification quality for different values of the decision threshold, Q_{hes}^{thresh}.

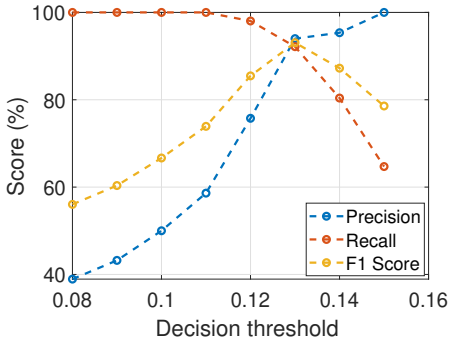

FIGURE 5.10 – Glottis closure detection classification quality for different values of the decision threshold, Q_{gc}^{thresh}.

coefficient of determination, defined as

$$R^2 = 1 - \frac{\sum_{i=1}^{n}(fi - \hat{f}_i)^2}{\sum_{i=1}^{n}(fi - \bar{f})^2} \tag{5.7}$$

where $\hat{f}_i$ is the prediction of the $i-th$ instantaneous flow by the linear regressor fitted to the set of observations F and $\bar{f}$ is the average value of F. Drawing on Eq. (5.7), we introduce BandS-Spi's no-hesitation metric, Q_{hes} :

Definition 3 (No-hesitation metric) *Let $F = f_{i\,i=1\ldots n}$ denote the set of instantaneous flow values until the PEF and F_{ref} the reference set. F_{ref} is obtained by averaging the F vectors of valid spirometry maneuvers in the data set of Section 5.5.1. The no-hesitation metric, Q_{hes}, is defined as :*

$$Q_{hes} = \frac{R^2(F)}{R^2(F_{ref})} \tag{5.8}$$

A spirometry maneuver with Q_{hes} below a given decision threshold is classified by BandS-Spi's virtual coach as having a hesitant start and therefore invalid. Fig. 5.9 shows BandS-Spi's classification quality of the maneuvers in the data set of Section 5.5.1 for different values of the decision threshold. Based on this data, $Q_{hes}^{thresh} = 0.65$, leading to an F1 score of 80%, is adopted as the default value.

5.5.2.2 Detecting early termination

To detect the end of a maneuver, BandS-Spi relies on the ATS recommendations [185] stating that a volume change of less than 25 mL in one second can be used as a sign of the end of the expiration. The virtual coach is programmed to consider a maneuver valid if the user holds the breath, to keep the balloon inflated, for a few seconds after expiration. Otherwise, the maneuver is considered invalid and the proper instructions are provided to the user.

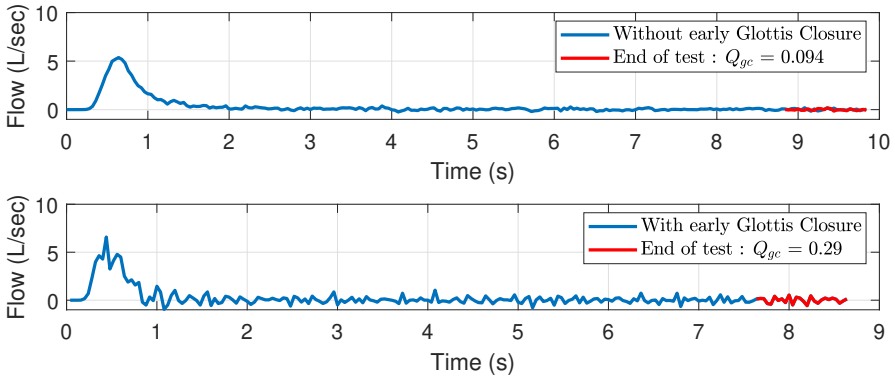

FIGURE 5.11 – Difference in the flow curves of an early glottis closure maneuver a normal maneuver.

5.5.2.3 Detecting early glottis closure

To detect an early glottis closure, we start with a careful analysis of the flow-time curve. As the data in Fig. 5.11 shows, there are differences in the flow-time curves of maneuvers with and without early glottis closure. The end of the maneuver in both cases is characterized by a high-frequency flow variation due to the small movement of air between the mouth and the balloon. This is induced by the oscillating contraction of the glottis, kept under tension and closed at the end of the maneuver. However, in the case of early glottis closure, there is more available air in the lungs, leading to higher amplitude oscillations.

Therefore, BandS-Spi's approach to detecting early glottis closure involves introducing a new metric, Q_{gc}, for quantifying the amplitude of the flow oscillations at the end of the maneuver and using it for classifying the maneuver.

Definition 4 (No-early-gc metric) *Let F_{end} denote the set of the flow values measured over the last second of the maneuver. The no-early-gc metric, Q_{gc} is defined as*

$$Q_{gc} = std(F_{end}) = \sqrt{\frac{1}{N}\sum_{t=1}^{N}(f_t - \bar{f}_t)^2},$$

where $f_t \in F_{end}$ and N is the size of F_{end}.

A spirometry maneuver with Q_{gc} below a given decision threshold, Q_{gc}^{thresh}, is classified by BandS-Spi's virtual coach as having an early glottis closure and therefore invalid. Fig. 5.10 shows BandS-Spi's classification quality of the maneuvers in the data set of Section 5.5.1 for different values of the decision threshold. Based on this data, $Q_{gc}^{thresh} = 0.13$, leading to an F1 score of 90%, is adopted as the default value.

5.6 Evaluation

In this section, we evaluate BandS-Spi's performance, focusing on its capability to deliver spirometry results comparable to medical spirometers and the state of the art, the impact of the virtual coach, sensitivity to the hardware used, and the user perception of its practicality.

5.6.1 Implementation

We implemented BandS-Spi as an android application. For the pressure-to-volume conversion, we use jcobyla [195], an open-source non-linear optimization library. It implements Cobyla [196, 197], a nonlinear derivative–free constrained optimization algorithm.

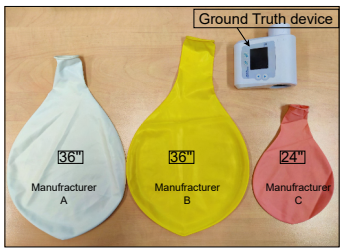

FIGURE 5.12 – Balloons used for evaluating BandS-Spi.

Number of participants	78
Males (n, %)	51 (65%)
Age (yrs) (mean, range)	26 (18 - 60)
Height (cm) (mean, range)	174 (155 - 194)
Reported lung ailments (n,%)	Mild Asthma : 7 (9%) Chronic Bronchitis : 12 (15%)
FVC (Liters) (mean, range) **PEF (Liters/sec) (Mean, range)**	4.48 (2.46 - 6.82) 9.17 (4.46 - 12.77)

TABLE 5.1 – Participant demographics

5.6.2 Evaluation setup

To evaluate BandS-Spi, we recruited 78 volunteers [1] in different age groups, including healthy people, asthmatics, and people with seasonal respiratory infections, such as bronchitis. Table 5.1 summarizes the demographic information of the volunteers.

The experimental protocol is as in Section 5.5.1. To acquire the ground truth we use an off-the-shelf hand-held spirometer [198]. Note that, it is impossible to simultaneously collect data from the spirometer device and BandS-Spi so explicit ground truth is unknown. We conduct our experiments using balloons of different sizes and from different manufacturers (See Fig. 5.12). In total, we recorded 355 spirometry maneuvers.

5.6.3 Overall spirometry performance

In this section, we evaluate BandS-Spi's performance in measuring the most clinically-reported spirometry parameters [10] : the Forced Vital Capacity (FVC), Forced Expiratory Volume in one second (FEV1) and the FEV1/FVC ratio.

Figure 5.13 shows BandS-Spi's overall performance when measuring the key lung function parameters. To put the performance into context, we add the average performance of handheld spirometers as reported in the literature [199]. The data shows that the average error is 3.97%, 4.94%, and 3.34% for FVC, FEV1, and FEV1/FVC, respectively.

1. Our experiments are in agreement with the ethics defined in the Helsinki Declaration [162].

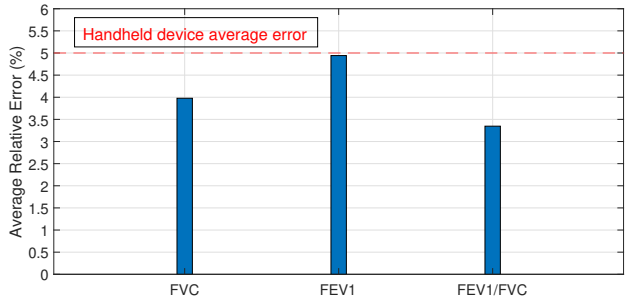

FIGURE 5.13 – BandS-Spi's overall spirometry performance.

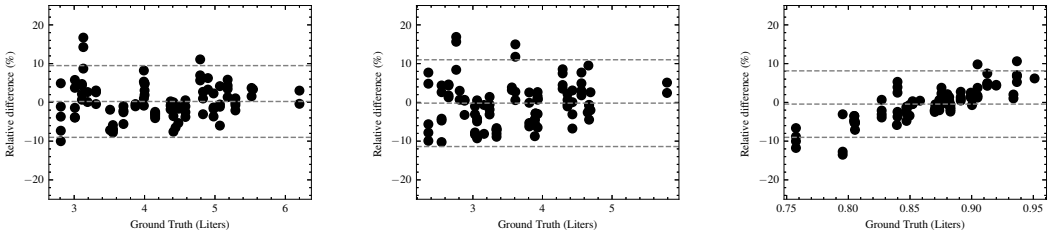

(a) FVC (b) FEV1 (c) FEV1/FVC

FIGURE 5.14 – Modified Bland-Altman plots. The x-axis is the ground truth while the y-axis is the relative difference in percentage between BandS-Spi and the ground truth.

More important, BandS-Spi's performance is similar to or better than that of handheld spirometers.

Figure. 5.14 shows modified Bland-Altman plots [200] of each lung function parameter. The x-axis is the ground truth while the y-axis is the relative difference in percentage between BandS-Spi and the ground truth. The data shows that BandS-Spi's relative error is normally distributed, independently of the ground truth. In all cases, we observe an error of 8% with a limit of agreement of 95%.

5.6.4 BandS-Spi vs. State of the art

In this section, we aim at contextualizing the performance of BandS-Spi by comparing it to the performance of state-of-the-art smartphone-based solutions, as that is reported in the respective papers. Table 5.2 shows the reported average errors for the lung function parameters of SpiroSonic [27], Exhalesense [182], and SpiroSmart [10], as well as those of BandS-Spi. The data shows that BandS-Spi offers the best overall performance.

TABLE 5.2 – BandS-Spi vs State-of-the-art solutions.

	FVC (%)	FEV1 (%)	FEV1/FVC (%)
SpiroSmart [10]	5.2	4.8	4.0
ExhaleSense [182]	N/A	N/A	7.57
SpiroSonic [27]	12.52	9.06	7.69
BandS-Spi	**3.97**	**4.94**	**3.34**

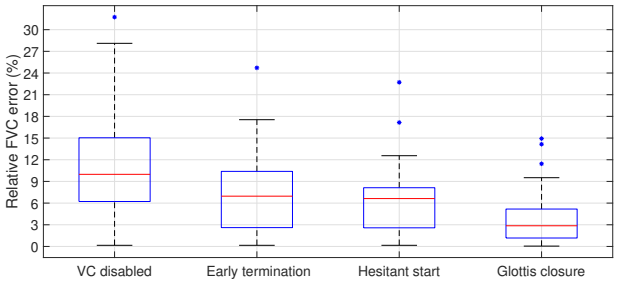

FIGURE 5.15 – Impact of BandS-Spi's virtual coach.

5.6.5 Impact of the virtual coach

In this section, we evaluate the impact of BandS-Spi's virtual coach on the FVC measurement accuracy. Towards this, we compare 4 versions of BandS-Spi : Virtual coach (VC) disabled, only early termination detection enabled (Early termination), early termination + hesitant start detection enabled (Hesitant start), and full virtual coach enabled (which includes the previous plus glottis closure detection). When part of or the entire virtual coach is enabled, the errors are computed only on the maneuvers it considers valid.

Figure 5.15 shows the boxplot of the relative FVC measurement error for the four versions of BandS-Spi. The data highlights the importance of the virtual coach. The median FVC measurement error drops from 10% when the virtual coach is disabled to 2.89% when it is fully enabled.

5.6.6 Sensitivity to balloon size and manufacturer

In this section, we evaluate BandS-Spi's sensitivity to the type of balloon it uses. Towards this, we use balloons from two different manufacturers as well as balloons of two different sizes : 24 and 36 inches. We run a new set of experiments with the help of 15 volunteers using the setup described in Section 5.5.1 with 15 volunteers. Every volunteer performs spirometry maneuvers with all the balloons, taking a break of 15 min when switching them.

Figure 5.16 shows that BandS-Spi's performance when measuring FVC is largely insensitive to the balloon size and manufacturer. The average FVC measurement error is 3.97% and 4.45% (Fig. 5.16a) with the 24 and 36-inch balloon, respectively – remaining under the symbolic bar of 5% in both cases. A similar conclusion can be drawn when BandS-Spi uses balloons of different manufacturers. As Fig. 5.16b shows, the difference in average error is less than 0.5%.

5.6.7 Resource utilization

We evaluate BandS-Spi's utilization of CPU, memory, and energy by using Android Profiler [168] and report the results in Table 5.3. The intrinsic multiprocessing nature of the mobile phone operating systems makes it very challenging to measure the exact

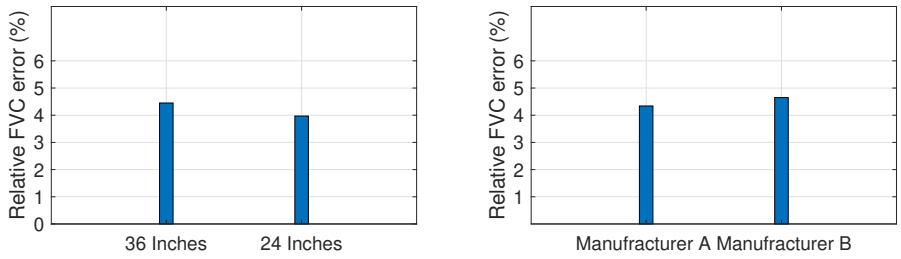

(a) Different balloon sizes.

(b) Different manufacturers.

FIGURE 5.16 – BandS-Spi's performance with different balloons.

TABLE 5.3 – BandS-Spi's resource utilization.

Device	CPU (%)	Memory (MB)	Energy (% of time) [L/M/H]
Samsumg Galaxy S8	15	158.3	87/13/0
Google pixel 4a	13	150	84/16/0

energy consumption of a given application. Thus, we show the percentage of time Android Profiler reports BandS-Spi's energy consumption as being Light (L), Medium (M), or Heavy (H). The data shows that BandS-Spi's utilization of resources is limited, especially in terms of energy consumption.

5.6.8 Participant Feedback

Finally, we conducted a survey to evaluate the participants' perception of BandS-Spi's usability. 45% of the participants declared they preferred BandS-Spi to the medical spirometer, a higher percentage than initially expected. The main reason cited for preferring BandS-Spi was the fact that the balloon pressure helps one to focus on blowing out through the end of the expiration. The spirometer, on the other hand, provides no feedback, making it difficult for some to blow out hard and/or keep blowing out through the end of the expiration. The 55% who preferred the medical spirometer cited the fact that BandS-Spi requires additional effort during the maneuver due to the balloon's internal pressure.

5.7 Discussions and conclusion

Limitations and future work

There are several ways in which this system can be improved. While BandS-Spi introduces a virtual coach, it currently focuses only on the quality of expiration. However, the quality of the expiration is inextricably linked to that of the inspiration preceding it. For example, Fig. 5.15 in Section 5.6.5 shows that the standard deviation of the FVC measurement error remains non-negligible (around 3%). Although this can be addressed by averaging the results of multiple maneuvers for the same user, we think that this error is

mainly related to the amplitude of the inspiration. Thus, one improvement of BandS-Spi's virtual coach is to add the automatic assessment of the inhalation quality, which can be approached by leveraging other sensors like the accelerometer.

Finally, a large-scale clinical study would solidify the conclusions of this work regarding BandS-Spi's spirometry performance.

Conclusion

We presented BandS-Spi, a solution for home spirometry that uses a smartphone and a balloon. BandS-Spi's key novelty is that it is the first smartphone-based solution to explicitly measure the exhaled air during a spirometry maneuver. Drawing on Boyle's law, we introduce a method for transforming the pressure-time curve produced with the help of the smartphone pressure sensor into a volume-time curve, enabling the computation of FVC, FEV1 and FEV1/FVC. To accommodate for the lack of coaching by a trained technician, BandS-Spi introduces a virtual coach capable of detecting with high accuracy invalid spirometry maneuvers. Results from 78 volunteers showed that BandS-Spi can perform a spirometry test with accuracy similar to or better than that of commercial handheld spirometers.

There is however, room for improvement for this work. Some users had difficulty inflating the balloons, resulting in unreliable spirometry data. We believe this is due to the impact of feedback pressure. It would be interesting to study the impact of the force required to inflate the balloon on the data quality. This information could be used to adjust the model accordingly. This also raises the interest in exploring a similar system for testing respiratory muscle strength, in order to detect some conditions like COPD or Neuromuscular Disorders [201].

Chapter 6

Single-Drop Liquid Testing Beyond the Laboratory

To showcase the capability of our smartphone-based method for enabling medical examinations beyond the laboratory, in this chapter we present Droplets, the first liquid testing solution that utilizes the most prevalent smartphone sensors, namely the camera and gyroscope, while requiring only a single liquid drop. The key innovation of Droplets lies in its capacity to discern liquids by leveraging their contact angle and capillary length, even from imperfect images – making it accessible to untrained individuals in non-laboratory settings. Building upon the Young-Laplace equation, we introduce a methodology for fitting the theoretical model of an imperfect drop profile measured from the image of the drop captured by the smartphone camera. To address the challenges posed by the non-laboratory setting, Droplets is designed to assist users in capturing high-quality images of the drop. Results from an Android implementation of Droplets demonstrate its ability to classify liquids with an accuracy of 84%. What is more, the experiments show that Droplets can be utilized to track protein levels in urine, indicating shifts from healthy to unhealthy levels.

6.1 Introduction

In recent years, there has been a growing interest in liquid testing, leading to the development of affordable and practical solutions suitable for non-laboratory environments [202-204]. The potential applications for large-scale liquid testing are diverse and encompass safety inspections in public transportation, cost-effective detection of water contamination, identification of counterfeit perfumes and liquors, medical examinations, monitoring of daily nutritional beverage intake, and more. While significant progress has been made to improve the accessibility of liquid testing, early solutions often relied on specialized hardware, such as RFID readers [203, 205], photodiodes [204], ultra-wideband (UWB) units [206], or piezoelectric sensors [207], which were not widely available to the general public.

Recognizing these limitations, CapCam [23] introduced a solution that utilized a commonly accessible equipment – the smartphone. CapCam measures the capillary waves generated by the smartphone's vibromotor when placed over a cup containing the liquid, enabling the determination of the liquid's surface tension. This concept sparked further research in smartphone-based liquid testing. Vi-Liquid [41] measures the liquid's viscosity using the smartphone's built-in vibromotor and accelerometer, while Viscocam [25] analyzes the decay of the liquid's sloshing motion to determine viscosity. [71] uses the smart-

phone's speaker to transmit acoustic signals and the microphone to receive the reflected signal, enabling the identification of different types of liquids. Although these solutions have made significant advancements by leveraging smartphones and easily obtainable accessories like water cups, they still face a common limitation – the cup typically requires a volume of approximately 400 ml. Collecting such a volume of fluid for testing purposes can be challenging, especially for individuals with conditions like oligoanuria [1]. Blood testing is another example where collecting such a volume would be impractical.

Identifying this limitation in the state of the art, [22] introduced the first solution that only requires a minimal amount of liquid — just a single drop. It utilizes the LiDAR sensor in smartphones to classify liquids based on the laser speckle patterns they produce. Unfortunately, smartphone manufacturers are progressively phasing out LiDAR sensors [208].

The review of the state of the art shows that, to date, there is no approach for analyzing limited volume of liquid –a single drop– with a sensor present in most smartphones. Hence, we formulate the objective of our system as follow :

Objective : *Measure reliably **drops of liquid** discriminant properties with a standard smartphone.*

To build our system, we first look for the sensors that will enable us to collect data from the object, in this case a drop of liquid. Although the most common approach in previous work has been to use the camera and computer vision techniques, these do not satisfy the constraints of our objective, which is to be able to test a single drop of the liquid. We propose to investigate a new approach, albeit keeping the same sensor. Specifically, the intuitive way we humans distinguish between two drops of liquid is by their shape. Thus, our intuition for the model is the relationship between the shape of a drop and its intrinsic properties, namely the surface tension and capillary length, defined by Young-Laplace's equation [31].

Contribution and plan

In this chapter, we introduce Droplets, the first liquid testing solution that leverages the ubiquitous smartphone sensors, namely the camera and gyroscope, and only requires a single liquid drop. The system captures images of the droplet and analyzes its shape to determine the properties of the liquid. We exploit the relationship between the shape of a sessile drop on a surface and the intrinsic properties of the liquid, namely its surface tension and capillary length [209, 210]. Fig. 6.1 illustrates the underlying principle of Droplets. Water, with its higher surface tension compared to ethanol, forms droplets with higher contact angles – the angle between the solid surface and the tangent line at the point where the liquid and solid interface meet. Ethanol, on the other hand, has a smaller capillary

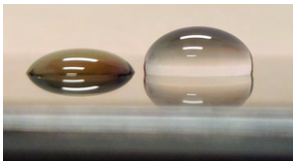

FIGURE 6.1 – Ethanol (left) and water droplets, exhibiting varying shapes.

1. A condition where less than 100 ml of urine is produced per day.

length, causing the droplet to flatten at a smaller volume. Hence, by extracting the contact angle and capillary length from the drop's image – a method known as the sessile drop technique [211] – Droplets can successfully identify different liquids.

While the sessile drop technique is supported by a solid mathematical foundation, its current system implementations require high-quality and consistent images of liquid droplets. Previous solutions have employed complex and specialized setups involving tripods or stands for camera stability, controlled lighting sources, and more [211-218]. The objective of Droplets is to offer a smartphone-based solution that is easily accessible to untrained individuals in non-laboratory environments – leading to a distinct set of system challenges.

First, in uncontrolled settings, the camera's alignment may not be parallel to the droplet's plane, distorting its apparent shape due to perspective effects. Second, the sessile drop technique relies on images with a clear and accurate contour of the droplet, particularly around the contact points. However, identifying these contact points can be challenging due to uncontrollable factors like illumination variations and liquid light absorption. Third, in an uncontrolled setting, it is impractical to determine the absolute capillary length from an image due to the absence of a reliable distance scale. As a result, the capillary length can only be measured in pixels whose size is affected by factors like the camera, zoom level, and distance to the droplet. Therefore, Droplets must find a solution to remove the dependence on pixel size. Finally, which (readily available) surface should be utilized for capturing images of droplets ? For a robust liquid testing system based on contact angle, the surface needs to be physically and chemically inert, smooth, homogeneous, rigid, and must exhibit sufficient hydrophobicity to ensure most liquid contact angles are visible.

To address these challenges, Droplets introduces multiple innovations :

— **Image acquisition with virtual assistance :** Droplets introduces a virtual assistant that helps users capture images without perspective effects by utilizing the gyroscope. It also provides guidance for optimal framing of the drops and suggests the appropriate background color based on the tested liquid's color (Section 6.5). However, even with the virtual assistant, images obtained in non-laboratory settings may still be imperfect, which leads to the next contributions

— **Contact points from imperfect images :** Building upon two key insights, Droplets introduce a new algorithm capable of identifying contact points even in imperfect images (Section 6.6).

— **Drop profile from imperfect images :** Droplets introduces a method that combines the Bashforth-Adams equations [219] with RANSAC (Random Sample Consensus) [220] to robustly compute the drop profile, even from imperfect images (Section 6.7).

— **Relaxing dependency on pixel size :** To eliminate reliance on pixel size, Droplets switches from absolute to relative computation of the capillary length. This is achieved by using a second liquid drop (water by default) as a reference in every image. The capillary length of the tested liquid is then computed as a percentage relative to the reference liquid (Section 6.7.3).

— **Which surface :** After testing various surfaces, we found that the smartphone screen surface was the best choice. Composed of tempered glass, the smartphone screen offers

a hydrophobic surface well-suited for measuring contact angles (Section 6.4).

We have developed Droplets as a standalone Android application (Section 6.8) and conducted a two-part performance evaluation (Section 6.9). The first part shows that Droplets achieves a median accuracy of 2 degrees in contact angle estimation and can classify 9 different liquids with an average accuracy of 84.5% on test data.

In the second part of the evaluation, we examine two specific use cases for liquid testing to cast a light on the practical potential of Droplets : counterfeit liquor detection and urine testing. The results show that that Droplets a) successfully distinguishes between authentic and counterfeit liquors, and b) tracks changes in protein levels in urine, indicating shifts from healthy to unhealthy levels.

Before delving into the design details of Droplet in Section 6.3, we provide an overview of the theory behind the Droplet model in Section 6.2. Specifically, we explain how the contact angle and capillary length can be utilized to distinguish between different liquids (Section 6.2.1 and 6.2.2). We then elaborate on the mathematical relationship between these features and the shape of a droplet in Section 6.2.3, followed by a discussion of the challenges associated with designing a robust solution based on this concept in Section 6.2.4. Finally, we discuss related work in Section 6.10, and conclude the chapter in Section 6.11.

6.2 Identifying liquids : From theory to system issues

In this section, we introduce the two features – contact angle (Section 6.2.1) and capillary length (Section 6.2.2) – used for identifying liquids, the theoretical framework for computing them from the image of a single drop (Section 6.2.3), along with the challenges that arise when implementing it on a smartphone in an out-of-laboratory environment (Section 6.2.4).

6.2.1 *Why contact angle can be used to identify liquids ?*

Liquids can be distinguished based on their wettability, which refers to their ability to spread and form a uniform film on a surface. This characteristic is determined by the surface tensions and polarities of different liquids [209, 210]. For instance, water, a liquid with high surface tension, tends to form beads on hydrophobic surfaces like wax or oil. Conversely, alcohol, having lower surface tension, readily wets hydrophobic surfaces.

The contact angle serves as an indicator of wettability, facilitating the identification of liquids. It represents the angle formed between the solid surface and the tangent line at the point where the liquid and solid interface meet. In Fig. 6.1, we can observe that a liquid with higher surface tension exhibits a higher contact angle compared to a liquid with lower surface tension. Young's equation [221] establishes a relationship between the contact angle and the interfacial tension of the system, given by

$$cos(\theta) = \frac{\gamma_{SV} - \gamma_{SL}}{\gamma_{LV}}, \tag{6.1}$$

where γ_{SV}, γ_{SL}, and γ_{LV} represent the surface tensions between the solid-vapor, solid-liquid, and liquid-vapor interfaces, respectively. By fixing the vapor as air and using the same solid each time, the contact angle becomes a direct indicator of the liquid's surface tension γ_{LV}. For simplicity, we will refer to surface tension as γ hereafter.

6.2.2 *Why Capillary length can be used to identify liquids ?*

The capillary length or capillary constant is a length scaling factor that relates gravity and surface tension. It is a fundamental physical property that governs the behavior of menisci and is found when body forces (gravity) and surface forces (Laplace pressure) are in equilibrium. For a liquid, a small capillary length indicates that a small drop volume is required for gravity forces to outweigh capillary forces, resulting in a flattened shape of the drop. Conversely, a large capillary length implies that a larger drop volume is needed before the drop deviates from a spherical cap shape and becomes flattened. Mathematically, it is defined as [222] :

$$a = \sqrt{\frac{\gamma}{\rho g}} \tag{6.2}$$

where γ is the surface tension of the liquid, ρ denotes the density of the liquid, and g corresponds to the acceleration due to gravity.

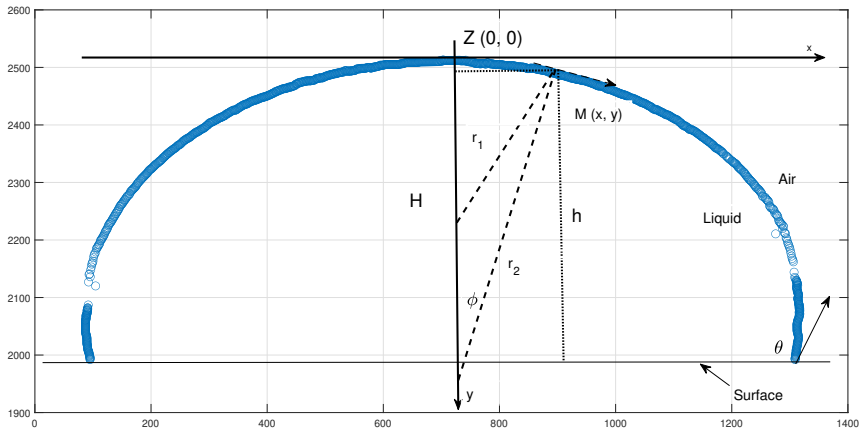

FIGURE 6.2 – Schematic of an axisymmetric drop on a nonwetting surface. For a point, M(x, y) on the projected drop profile, x represents the horizontal position, y represents the vertical position, r_1 and r_2 the two principal radii of curvature, ϕ represents the angle formed between the normal at point M and the axis of rotation, H is the overall height of the droplet, and $\theta = max(\phi)$ denotes the maximum contact angle of the liquid droplet at the contact line.

Therefore, the capillary length provides additional information about the liquid beyond surface tension.

6.2.3 *Sessile drop shape analysis*

In this section, we describe the process of extracting the capillary length and contact angle based on the drop's shape.

6.2.3.1 Theoretical foundation

Let us consider an axisymmetric liquid drop positioned on a surface, as depicted in Fig. 6.2. According to the Laplace equation, the pressure difference, ΔP, across a particular point, M, on the liquid-air interface can be expressed as a function of the liquid surface tension, γ, and the radii of curvature (r_1 and r_2) of the drop at M, as described by [31] :

$$\Delta P = \gamma(\frac{1}{r_1} + \frac{1}{r_2}). \tag{6.3}$$

While the measurement of r_1 and r_2 from the profile is potentially feasible, it is a non-trivial task. At the apex of the drop, however, since the drop is axis-symmetric, r_1 and r_2 are equal. Denoting by b the radius of curvature at the apex, we can re-write Eq. 6.3 as $\Delta P_0 = \frac{2\gamma}{b}$.

Within a droplet that is symmetric about the central vertical axis, the pressure difference, ΔP, varies linearly with elevation [31]. Hence, considering O in Fig. 6.2 as the

origin point, we can express ΔP at any point below as a function of gravity as well as the disparity in density between the droplet and the surrounding medium. Let $\Delta\rho$ represent the difference in densities, g denote the acceleration due to gravity, and y represent the distance from the origin point. We have

$$\Delta P = \frac{2\gamma}{b} + \Delta\rho g y \tag{6.4}$$

Combining Eq. 6.3 and Eq. 6.4 leads to the well known Laplace-Young equation :

$$\Delta\rho g y + \frac{2\gamma}{b} = \gamma(\frac{1}{r_1} + \frac{1}{r_2}) \tag{6.5}$$

Expressing the radii of curvatures r_1 and r_2 in X-Y coordinates (where the height H is in the y direction) leads to the Bashforth-Adams Equation [32]

$$\gamma(\frac{y''}{(1+y'^2)^{3/2}} + \frac{y'}{x(1+y'^2)^{1/2}}) = \frac{2\gamma}{b} + \Delta\rho g y \tag{6.6}$$

where $y' = dy/dx$ and $y'' = dy^2/dx^2$. This differential equation describes the behavior of $y(x)$ but has no analytical solution. A simpler approach is obtained by introducing the substitution $y'(x) = \tan(\phi)$ [214]. This substitution helps avoid complex manipulations due to y not being a single-valued function of x. By parameterizing with the tangent angle ϕ and introducing the capillary length expressed in Eq. 6.2, a set of equations can be derived that solely involve the Cartesian coordinates y and x, along with the two parameters a and b :

$$\begin{cases} \frac{dx}{d\phi} = \frac{bxcos(\phi)}{a^2bxy+2x-bsin(\phi)} \\ \frac{dy}{d\phi} = \frac{bxsin(\phi)}{a^2bxy+2x-bsin(\phi)} \end{cases} \tag{6.7}$$

The shape of the sessile drop is determined by the set of points $x(\phi), y(\phi)$ that satisfy Eq. 6.7 as well as the contact angle θ between the sessile drop and the surface. To obtain the theoretical profile of a drop for a specific (a, b) combination, we can numerically integrate this equation from the baseline (y=0) to the height of the drop (y=H) using the backward differential formula (BDF) solution method [223].

6.2.3.2 Numerical approach

From an image of the sessile drop, we can extract the drop profile's edge, which forms a set of points $\{[x_i, y_i]\}^i_{picture}$. Our goal is to find the best-fitting parameters a and b for Eq. 6.7. This is achieved by minimizing the expression given by :

$$a^*, b^* = \arg\min_{a,b} \sum_{i=1}^{n} min_j \| \begin{bmatrix} x_i \\ y_i \end{bmatrix} - \begin{bmatrix} x'_j \\ y'_j \end{bmatrix} (a, b) \|^2. \tag{6.8}$$

Here, x'_j, y'_j represents the profile point generated using Eq. 6.7 with the parameters a and b. The value of a^* corresponds to the best-fit capillary length for the droplet, measured in pixels. The parameter b represents the radii of curvature at the apex O and is related to

the volume of the drop. The contact angle θ is defined as the parametric angle ϕ at which the vertical position equals the measured droplet height, i.e., $\theta / y(\theta) = H$, as depicted in Fig. 6.2.

6.2.4 System challenges

The theoretical framework presented in the previous section necessitates high-quality and consistent images of liquid drops. Previous solutions have utilized intricate and specialized setups, incorporating tripods or stands to stabilize the camera, controlled lighting sources, and so forth [32, 211, 213-215, 217]. However, Droplets aims to provide a smartphone-based solution that is accessible to untrained individuals in non-laboratory settings. As a result, several distinct challenges and questions emerge :

1. In uncontrolled settings, it is highly probable that the camera is not parallel to the plane of the drop. In such cases, perspective effects can distort the apparent shape of the drop.
2. The theoretical framework relies on images with a clear and accurate contour of the drop, especially in the vicinity of the contact points. However, the identification of contact points may pose challenges due to uncontrollable factors such as illumination variations and the light absorption properties of the liquid.
3. The contact line, Fig. 6.2, becomes visible in the image when the camera is precisely aligned with both the surface and the drop. However, achieving such perfect alignment between the smartphone, drop, and the center of the camera sensor without a fixed setup poses a significant challenge.
4. Which surface should be used for acquiring images of drops ? To align with the objective of Droplets, the surface should be easily accessible.

In the following sections, we present the design and implementation of Droplets, which carefully addresses all these challenges.

6.3 Droplets system overview

Figure 6.3 shows a high-level depiction of Droplets' architecture. It comprises 4 modules :

1. *Image acquisition :* Droplets' process begins when the user puts a drop on the smartphone screen (Section 6.4), which is positioned on a table. The Image Acquisition module, which is described in Section 6.5, is specifically designed to allow an untrained user to capture a high-quality front-view image of the drop. Subsequently, the image acquired from this module is transferred to the drop profile extraction module.
2. *Drop profile extraction :* Droplets utilizes the Canny filter [99] on the image converted to grayscale in order to extract the drop's edges. These edges are subsequently transformed into a collection of pixel points that represent the drop profile, denoted as $Profile = \{M(x, y)\}$.
3. *Contact line detection :* In Section 6.6, we outline the challenges associated with reliable contact line detection from the drop profile. Additionally, we present our algorithm designed to address these challenges. We also elaborate on our methodology for detecting

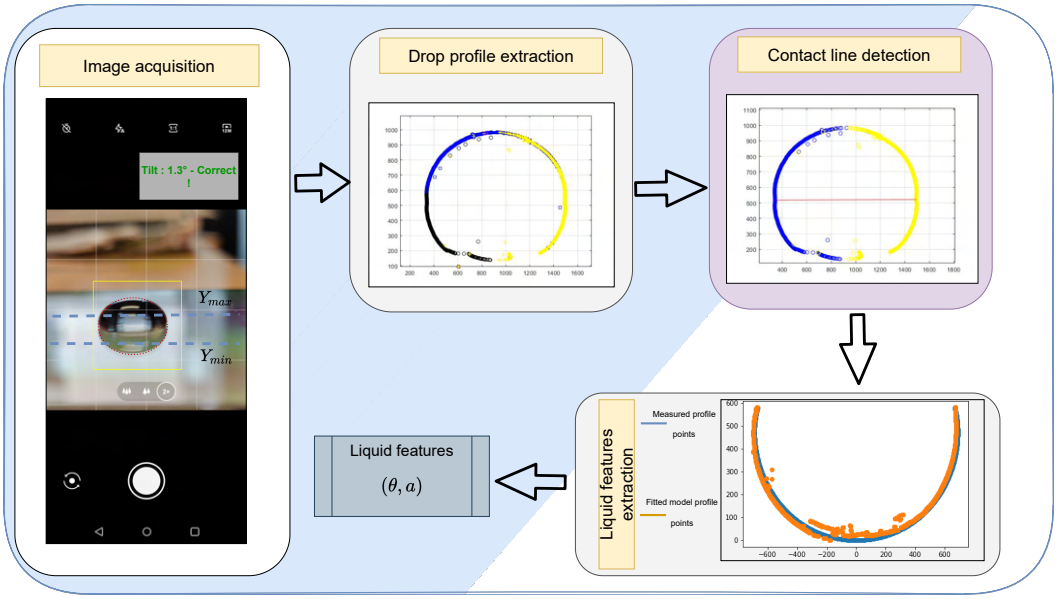

FIGURE 6.3 – The system architecture of Droplets.

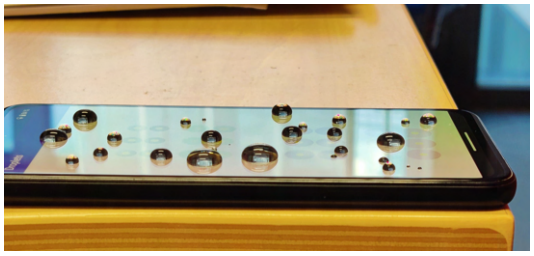

FIGURE 6.4 – Liquid droplets on the screen of a smartphone.

difficult liquid testing conditions, as well as how we notify the user through the user interface (UI) to guide them towards an improved setting.

4. *Liquid feature extraction :* It takes as input the drop profile and contact line and computes the liquid features : contact angle and capillary length values. The features are transformed so as to remove the impact of outside factors, including zoom, distance between camera and the drop, etc. Section 6.7 describes the challenges this module faces as well as the algorithm for addressing them.
5. *Liquid classification :* The final step involves solving a classification problem based on the computed liquid features. It does not present any distinct challenges compared to the extensive research on the subject. Therefore, Droplets utilizes the classic KNN algorithm.

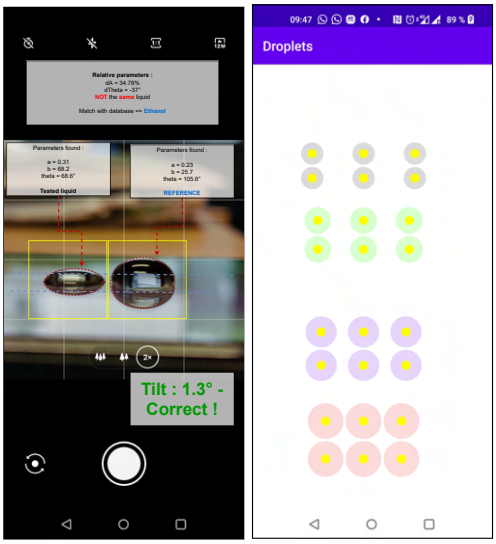

(a) Scan mode. (b) Surface mode.

FIGURE 6.5 – Droplets' virtual assistant interface.

6.4 *Which surface for ubiquitous drop shape analysis?*

For a robust liquid testing system based on contact angle, certain conditions must be met for the surface on which the drop is placed. These conditions include being physically and chemically inert, smooth, homogeneous, and rigid [224-226]. If the surface is rough, measurements of the drop's contact angles for the same liquid may vary. Additionally, the presence of dirt on a chemically unclean surface can affect the contact angle. Therefore, it is crucial for the surface to be smooth and easily cleanable. Another requirement is that the surface should be widely available, aligning with Droplets' objective of providing ubiquitous liquid testing. Finally, the surface must exhibit sufficient hydrophobicity to ensure most liquid contact angles are visible, i.e., greater than zero.

After testing several different surfaces such as glass, plastic, cardboard, wood, and others, we determined that the surface of a smartphone screen was the best choice. The screen of a smartphone is composed of tempered glass, providing a hydrophobic surface that is well-suited for measuring contact angles. It is readily available and can be easily cleaned. Moreover, its smooth and hydrophobic nature ensures that the contact angles obtained are relatively high and can be measured reliably. While it is recognized that the volume of the drop may influence the contact angle [227], this effect is minimized when using a smooth surface such as the smartphone screen. Figure 6.4 depicts water and ethanol drops on a smartphone screen.

6.5 Image Acquisition with Virtual Assistance

A key challenge for Droplets is enabling untrained individuals in an uncontrolled setting to capture sessile drop images for reliable liquid testing on a smartphone. This chal-

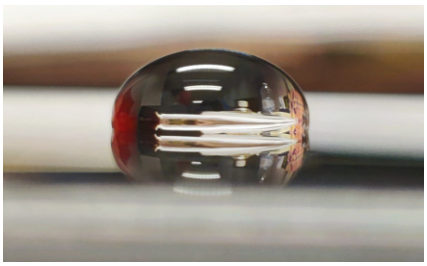

(a) Water with a standard background

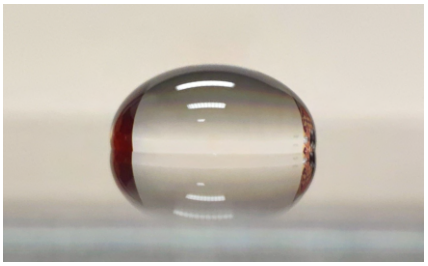

(b) A drop of water with white background

FIGURE 6.6 – Changing the background can clarify the edges

lenge is twofold. First, maintaining a parallel camera position to the drop's plane during image capture is crucial to avoid perspective effects that may distort the apparent shape of the drop. However, users are not expected to possess specialized equipment to meet this requirement. Second, achieving sufficient contrast clarity between the drop's contour and surrounding contact points is essential. Depending on the illumination and light absorption properties of the liquid, the algorithm described in Section 6.6 may face difficulties in identifying contact points. Therefore, Droplets must provide users with feedback on image quality to assist them in identifying the optimal measurement conditions.

To overcome this challenge, Droplets introduces a virtual assistant, as depicted in Fig. 6.5. In scan mode, as shown in Fig. 6.5a, it incorporates three mechanisms. First, to aid users in capturing images without perspective effects, the virtual assistant utilizes the smartphone's gyroscope sensor. It measures and displays real-time roll and azimuth angles, providing immediate orientation feedback. Second, two horizontal lines (represented as y_{min} and y_{max} in Fig. 6.3) delineate the contact zone, guiding users to position the drop's contact points within it for improved detection. The contact line extraction module, Section 6.6, focuses only on the specified y-range. If the contact line is undetected, the virtual assistant alerts the user and suggests modifying the setup. Finally, the virtual assistant directs users to adjust the orientation relative to the light source or place an object with a white or darker color in the background. It provides users with the optimal background color selection based on the color of the tested liquid. Fig. 6.6 illustrates the impact of changing the background color, with the contact line more visible against a white background.

6.6 Contact line extraction

The contact line, a straight line visible in the image when the camera aligns perfectly with the surface and the drop, has been the focus of previous works in controlled settings [211-218]. However, in our case, achieving perfect alignment between the smartphone, drop, and camera sensor center without a fixed setup is challenging, even with the Virtual Assistant introduced in Section 6.5. Additionally, the smartphone's thick edge causes blurriness in the camera image. As a result, previous approaches have relied on expli-

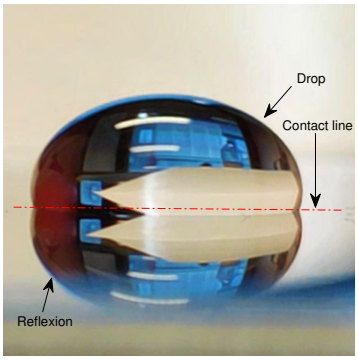

FIGURE 6.7 – A drop of water on a smartphone screen and the contact line.

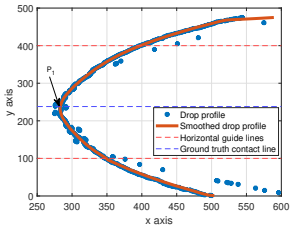

(a) Cognac (contact angle of 76°)

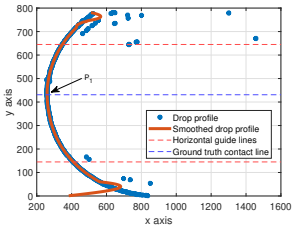

(b) Wine (contact angle of 91°)

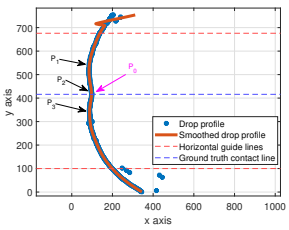

(c) Water (contact angle of 107°)

FIGURE 6.8 – Illustration of the efficiency of contact point detection algorithm.

cit user intervention to locate contact points [211], such as drawing a horizontal line or manually selecting contact points in an image editor.

However, Droplets aims for minimal user involvement. To detect the contact line, Droplets utilizes the reflection of the drop on the surface. As depicted in Fig. 6.7, the meeting points of the actual and reflected drop profiles represent the contact points. By connecting these meeting points, the line formed becomes the contact line. The following provides a detailed explanation of our contact line extraction method.

6.6.1 Contact point extraction algorithm

In this section, we present Droplets' algorithm (sketched in Algorithm 2) for detecting the contact line. Its design is based on two insights. First, we note that the screen of a smartphone is highly reflective. Specifically, the edges of the droplet and its reflection intersect at the contact points, which are the endpoints of the contact line (see Fig. 6.7). By treating the lateral sections of the profile as a function, we observe a change in the slope sign at the contact point. Second, the change in direction is approximately the same when transitioning from the droplet contour to its reflection. Hence, in order to determine the contact point, we seek the position where the slopes at the top and bottom of this curve

Algorithm 2 Contact point extraction algorithm

Input : Side of the drop profile $P_L = \{[x_i, y_i]\}_1^M$, the amount of neighbooring point to consider N

Output : The estimated contact point P_0 or nothing if impossible

```
7  candidateP = []
   for n := N to M do
8      Left = {[x_i, y_i]_{i=n-N+1}^{n-1}}
       Right = {[x_i, y_i]_{i=n+1}^{n+N-1}}
       slopeLeft = slope(LinearFit(Left)) /*Compute the slope of the linear fit of the data
       points Left*/
       slopeRight = slope(LinearFit(Right)) /*Compute the slope of the linear fit of the data
       points Right*/
       slopeDiff = slopeLeft-slopeRight
       if slopeDiff = 0 then
9          /*We may find the contact point.*/
           candidateP = candidateP.append([x_n, y_n])
10 if size(candidateP) = 1 then
11     return candidateP(1)
12 if size(candidateP) = 3 then
13     return candidateP(2)
14 return []
```

cancel each other out.

The algorithm searches for the index n where the points $n-N$ and $n+N$, representing one point per pixel, are fitted to two lines. These lines should have equal-magnitude slopes but opposite signs. Let us focus on the left side of the droplet and its reflection, which we denote as P_L. For y values within the range $[y_{min}, y_{max}]$, we define $P_L(y)$ as x_y. First, we apply a Savitzky-Golay filter to smoothen P_L and eliminate small irregularities. Then, for each point, the algorithm calculates the top and bottom slopes of P_L by fitting lines through N points above and below the selected point (lines 5, 6, Algorithm 2). We measure the difference between these two slopes, expecting it to be close to zero at the contact point (line 8).

We repeat this process for both sides of the profile and determine the contact line by connecting the two contact points.

In Fig. 6.8, we illustrate three different configurations for the contact points, representing cases where the contact angle is above, below, or approximately 90°. We also depict the corresponding possible contact points that have been identified. When the contact angle is below 90°, as shown in Fig. 6.8a, there is only one candidate for the contact point (line 11). However, when the contact angle exceeds 90°, as shown in Fig. 6.8c, there are three potential candidates. In this scenario, the contact point is determined to be the candidate that lies between the other two (line 14).

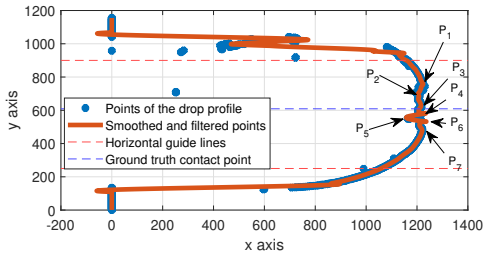

FIGURE 6.9 – A case where it is difficult to detect the contact points from drop profile points.

6.6.2 Interaction with the Virtual Assistant

Recall that the Virtual Assistant's role (Section 6.5) is crucial in enabling liquid testing in uncontrolled settings. The contact line extraction algorithm, introduced in the previous section, assists the virtual assistant by indicating when the picture quality is inadequate for reliable contact point detection. To achieve this, we count the number of candidate contact points for each side, i.e., the number of points where the left and right slopes are equal. We encounter three cases :

1. Algorithm 2 finds only one candidate contact point (line 11), denoted as P_1 in Fig. 6.8a and Fig. 6.8b. In this situation, P_1 is selected as the contact point, representing a liquid with a contact angle between 0 and 90°.
2. Algorithm 2 identifies three candidates : P_1, P_2, and P_3, listed in decreasing order of their y coordinates. In this case, the algorithm returns P_2 (line 14). The rationale behind this decision is that the first and last slopes detected correspond to the outermost portions of the droplet when dealing with a liquid with a contact angle greater than 90°, as depicted in Fig. 6.8c.
3. In the final case, we may have either two, four, or more candidate contact points, indicating the presence of challenging edge points near the contact points. Selecting the correct contact point becomes difficult in such instances, as shown in Fig. 6.9. Consequently, the algorithm notifies the Virtual Assistant (line 15) that the picture lacks sufficient quality. The Virtual Assistant then engages with the user to rectify the situation.

6.7 Liquid feature extractor

In this section, we describe Droplets' methodology for computing the two liquid features : capillary length, a (Section 6.2.2), and contact angle, θ (Section 6.2.1).

6.7.1 Approach overview and challenges

The overall approach is based on the theoretical framework introduced in Section 6.2.3. To compute the capillary length and contact angle, we take as input the drop profile points and the contact line. By utilizing the contact line, we measure the drop

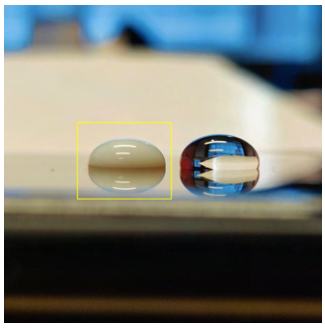

(a) Drops of milk and water.

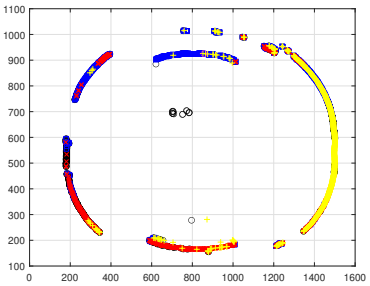

(b) Milk profile points extracted.

FIGURE 6.10 – The presence of reflections on the top of the drop (top figure) makes it challenging to accurately determine the drop's height from this image. Additionally, another reflection introduces spurious data points in the extracted profile (bottom figure).

height H and search for the parameters (a,b) that best fit the profile point generated by the used model. Specifically, for each pair of parameters (a,b), we integrate Eq. 6.7 from $y = 0$ to H and generate a set of *Generated profile points* (x'_i, y'_i). We then compare these *Generated profile points* with the measured profile points and keep the liquid features that show the closest match, as determined by Eq. 6.8.

However, this approach faces several challenges when applied using a smartphone in an uncontrolled setting. First, as shown in Fig. 6.10, the apex of the drop can be inaccurate due to uncontrolled lighting conditions, especially in the case where it is obscured by a reflection. This can lead to significant errors in computing the drop height, H, as shown in Fig. 6.11a.

Second, spurious data points may be generated by the edge detection algorithm due to the image quality, as shown in Fig. 6.11b, leading to contact angle computation errors.

Finally, the computation of the capillary length is dependent on the pixel size, which itself is influenced by various uncontrollable factors such as the camera, zoom level, and distance to the drop, among others.

In the following, we describe how Droplets addresses these challenges.

6.7.2 Dealing with noisy profile points

In this section, we will describe how Droplets tackles the challenges arising from inaccuracies in the computation of the drop height, H, and the presence of spurious data points in the drop profile.

To address the first challenge, we redefine the optimization problem presented in Eq.6.8 to incorporate the coordinates of O (Fig.6.2), the apex point. By introducing $O(x_o, y_o)$, we get :

$$a^*, b^*, x_o^*, y_o^* = \underset{a,b,x_o,y_o}{\arg\min} \sum_{i=1}^{n} min_j \begin{bmatrix} x_i \\ y_i \end{bmatrix} - \begin{bmatrix} x_o \\ y_o \end{bmatrix} - \begin{bmatrix} x'_j \\ y'_j \end{bmatrix} (a,b) \tag{6.9}$$

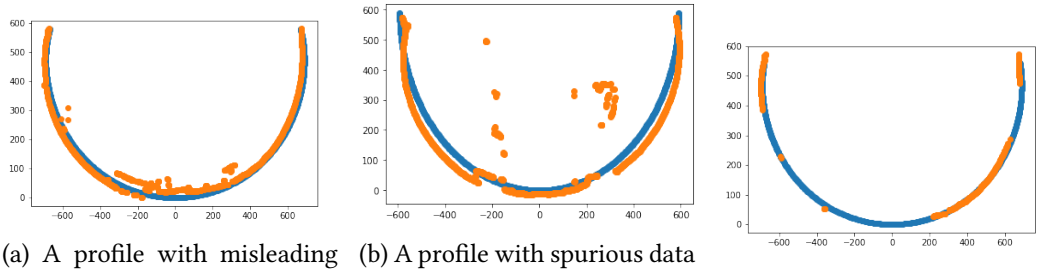

(a) A profile with misleading apex O point, leading to an error of 5.54°.

(b) A profile with spurious data points, leading to an error of 12.33°.

(c) Droplets achieves a good fit, reducing the error to 0.05°.

FIGURE 6.11 – The impact of spurious data points and the misleading apex point O on the measurement of the contact angle of a water droplet both with and without the utilization of Droplets. In orange the profile points obtained from the image, while in blue the profile points generated using the best-fitted model.

Through the solution of Eq. 6.9, we estimate the liquid features a and b, and robustly determine the most probable drop height using y_0.

To address the challenge posed by spurious data points, we incorporate into our design RANSAC [220] (Random Sample Consensus), a state-of-the-art algorithm for fitting a model with noisy points. The set of profile points is randomly subsampled, and Eq. 6.9 is utilized to obtain potential features. The points that closely adhere to the model within a defined error threshold are selected as potential inliers. This process is repeated with different subsets, and the subset with the maximum number of inliers is chosen to generate the final liquid features. As Fig. 6.11c shows, this method leads to a good fit.

6.7.3 Camera-independent liquid features

The computation of the capillary length, as discussed in the preceding section, produces a value in pixels, whose size depends on the measurement setting, limiting its practical utility. To maintain consistency with the goals of Droplets, it is necessary to derive a capillary length value that solely depends on the liquid being tested.

To achieve this, we employ a second liquid drop as a reference. Let L denote the liquid being tested, and ref represent the reference liquid, in this instance, water. The relative capillary length of the tested liquid, expressed as a percentage, is computed by Droplets as $a' = 100 * |a_L - a_{ref}|/a_{ref}$.

6.8 Implementation and evaluation setup

6.8.1 Implementation

The optimization component (Eq. 6.9, Section 6.7.2) is implemented using Nelder-Mead optimization [228], a heuristic numerical method designed to minimize continuous functions in multidimensional spaces. The software offers two operational modes, depicted in Fig. 6.5 : scan mode, which employs the camera to measure drop characteristics,

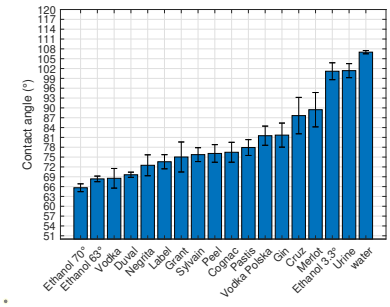

(a) Contact angle of various liquid products.

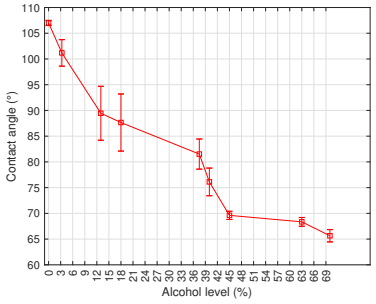

(b) The contact angle of various alcohol-level beverages.

FIGURE 6.12 – Contact angle measurement results.

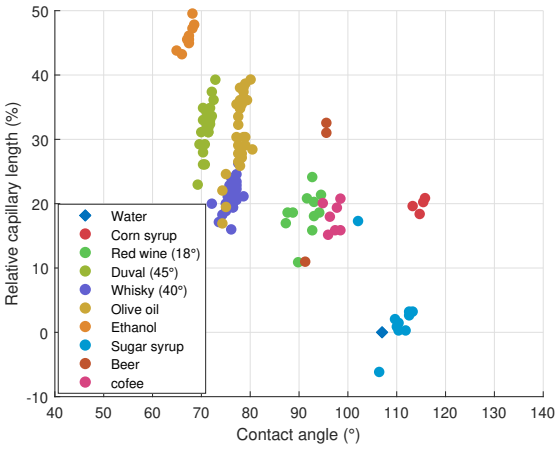

FIGURE 6.13 – Scatter plot of the features measured by Droplets for several liquids.

and surface mode, which displays circular shapes on the screen to guide the user in positioning a drop of a predetermined size. In surface mode, there are four available sizes : 50, 60, 70, and 80 px radius, corresponding to approximately 50 μL to 160 μL. For the scan mode, the camera settings are configured to a resolution of 1080*1080 with an aspect ratio of 1.

6.8.2 Testing setup

In our experiments, we employ a OnePlus 8t as the scanner and a Google Pixel 4 as the surface. To test a liquid, we utilize a syringe to place a drop of the liquid on the left circle and a drop of the reference liquid on the right circle, both with standardized sizes. The surface phone is positioned horizontally on a table. Using the scanner phone, we employ Droplets to scan both drops within a single image and execute the test. Following each measurement, we clean the surface phone screen using water and ethanol and allow it to air dry.

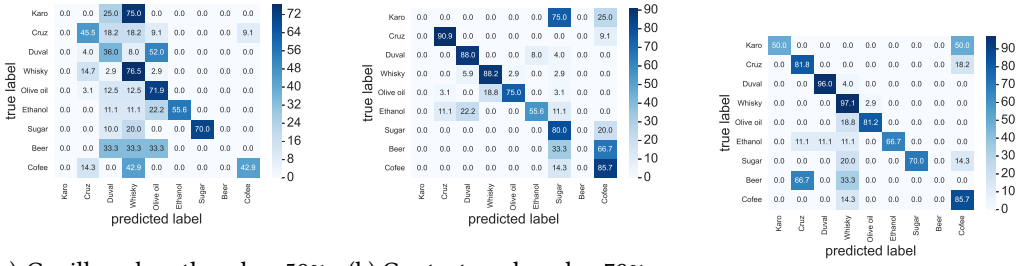

(a) Capillary length only : 58% accuracy.

(b) Contact angle only : 78% accuracy.

(c) Droplets : 84% accuracy.

FIGURE 6.14 – Liquid classification.

6.8.3 Evaluation setup

The performance evaluation is divided into two parts. The first part focuses on assessing the overall performance of Droplets. In the second part, we examine two specific use cases for liquid testing to cast a light on the practical potential of Droplets.

6.8.3.1 Part 1 : Overall Performance

We start by evaluating the overall performance of Droplets in liquid testing. Specifically, we focus on the following aspects :

Accuracy : To gauge the overall performance of Droplets in measuring contact angles, we conducted several experiments with ten different liquids, encompassing contact angles ranging from 68 to 114°. Since we do not have a ground truth contact angle for comparison, we evaluate the accuracy of Droplets by using the standard deviation of the measurements as the error metric. The results are discussed in Section 6.9.1.

Feature Quality : To evaluate the significance of each individual feature in liquid classification, we present classification results in Section 6.9.2, utilizing both features to differentiate between liquids.

System Robustness : Finally, we evaluate SmartPhOx's robustness by assessing its capacity to accurately measure the contact angle of liquids in various setups. The results are discussed in Section 6.9.3.

6.8.3.2 Part 2 : Use cases

To explore the practical potential of Droplets, we examine two use cases : counterfeit liquor detection and urine testing.

Counterfeit Alcohol Detection : We conducted an examination of Droplets's ability to distinguish between authentic liqueur and a counterfeit version containing 30% water. The findings of this analysis are discussed in Section 6.9.4.

Urine Testing : One potential application of Droplets is to simplify the monitoring of urine albumin levels for patients with diabetes by acting as an early-warning system. The findings of our analysis are presented in Section 6.9.5.

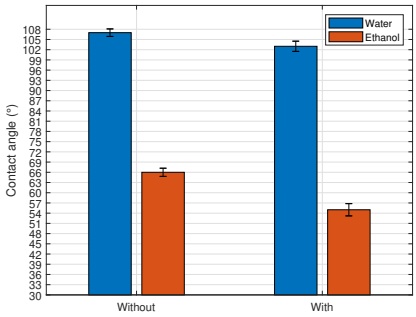

(a) Contact angle measurements with and without the presence of a screen protector.

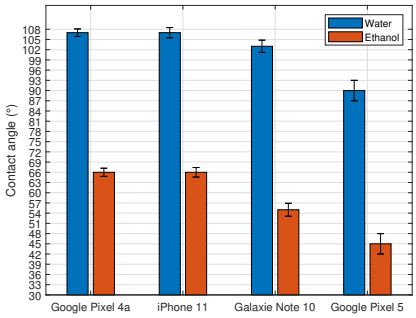

(b) Contact angle measurements on various phone models.

FIGURE 6.15 – Contact angle measurements of water and ethanol.

6.9 Evaluation results

6.9.1 Droplets' accuracy

In this section, we present the performance of Droplets in measuring contact angles for various liquids, including Cognac, red wine Cruz, Ethanol, Gin, Red label, red wine Merlot, Whisky, Duval, William peel scotch, Rhum Negrita, Label scotch, Calvados busnel (Sylvain), Vodka, Vodka Poliakov, urine, and water. We conduct multiple tests and report the average measured contact angles along with the error range in Fig. 6.12a. The contact angle error is generally below 2 degrees, except for Cruz and Merlot, where it reaches 4°. This discrepancy can be attributed to their contact angles being around 90°, making it challenging to accurately identify the contact line. Even a slight error in contact line identification results in a significant error in the estimated contact angle at $\theta \approx 90°$. Additionally, we observed that distinguishing between Negrita, Label, Peel, Grant, and Sylvain is difficult since they have similar contact angles around 75°, attributed to their identical alcohol content of 40%. However, we can clearly differentiate them from Vodka Poliakov, Duval, and Gin, as their alcohol levels vary (37.5° for Vodka Poliakov and Gin, and 45° for Duval). In Fig. 6.12b, we illustrate the relationship between contact angle and alcohol level in the beverage, demonstrating Droplets' ability to accurately track alcohol content. Notably, Droplets exhibits sensitivity in distinguishing between water (0°) and a 3.3° ethanol solution.

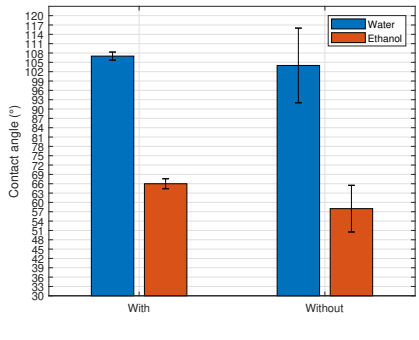

FIGURE 6.16 – Contact angle measurements with and without the virtual assistant.

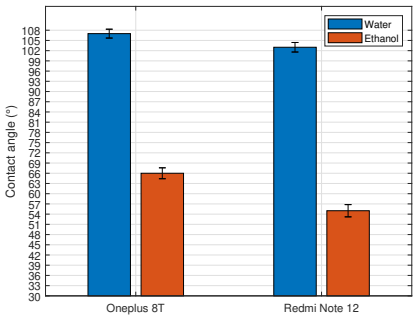

FIGURE 6.17 – Contact angle with different cameras.

6.9.2 Liquid classification

Fig. 6.13 depicts a scatter plot showcasing the features of 10 liquids. The data shows that distinguishing between olive oil and Whiskey based solely on contact angle is challenging, as the measured contact angle ranges between 75-80 degrees for both liquids. However, by incorporating the capillary length (Y-axis), we can easily distinguish the two liquids. This observation is further supported by the confusion matrices presented in Fig. 6.14. By utilizing the estimated contact angle and capillary length as features, and the corresponding liquid as labels, we can employ a simple K-Nearest Neighbors algorithm (K=3) to differentiate between these liquids. The resulting confusion matrices demonstrate an average classification accuracy of 58%, 78%, and 84%, respectively, when using only capillary length, contact angle, and both features for the nine types of liquids. In Figure 6.14c, it can be observed that Droplets encounters difficulties in identifying beer. This issue is likely attributed to the presence of gas within the liquid. When a small drop of beer is placed on a surface, the carbon dioxide (CO2) trapped within the drop begins to release in the form of small bubbles. This process leads to changes in the shape of the drop over time, thereby posing challenges in obtaining precise measurements.

6.9.3 System robustness

In this section, we assess SmartPhOx' robustness by evaluating its performance across various real-world configurations. As SmartPhOx' proper functionality hinges on three core elements — surface, camera, and lighting — the evaluation is structured to measure its performance when these elements are modified.

SmartPhOx on different surfaces : Two factors may influence the surface where the drop is positioned : the presence of a screen protector and the smartphone model.

Fig. 6.15a depicts the contact angles of ten different water and ethanol drops on a Google Pixel 5 screen, with and without a screen protector. The data shows a marginal error shift from 1.2 to 1.8 degrees. This minor influence on SmartPhOx' performance can

be attributed to the fact that modern screen protectors are composed of tempered glass, providing a high-quality hydrophobic surface [229].

Fig. 6.15b depicts contact angle measurements for four popular smartphone models : Google Pixel 4a, iPhone 11, Galaxy Note 10, and Google Pixel 5. The average contact angle errors are 1.2, 1.5, 1.8, and 3 degrees, respectively. Differences, especially among the first three models, are minimal. This can be attributed to the dominance of a handful of companies in the smartphone screen market [2]. Some variations are observed, particularly in the Google Pixel 5, possibly due to manufacturing differences. We note that a 2% margin of error in contact angle measurements is a threshold value for the urine testing use case discussed in Section 6.9.5.

SmartPhOx under different lighting conditions : Another significant factor affecting SmartPhOx is external conditions that influence picture quality, primarily illumination. To address this challenge, we introduced the virtual assistant in Section 6.5. To evaluate its performance, we conducted experiments using drops of water and ethanol under various lighting conditions. To adjust the lighting, we modified the indoor ambient lighting and carried out experiments at different times of the day outdoors.

Results : Fig. 6.16 depicts the contact angle measurements with and without the virtual assistant. We observe that without the virtual assistant, the average error is significant, approximately 12 degrees. However, when the virtual assistant is enabled, the error drops to around 1.3 degrees, underscoring its role in enhancing the robustness of SmartPhOx.

SmartPhOx with different cameras : To evaluate the influence of the camera SmartPhOx employs for image acquisition, we utilized two Android-based smartphones : the OnePlus 8, equipped with a Sony IMX586 camera, and the Redmi Note 12, featuring a Samsung ISOCELL HM2 camera. We performed contact angle measurements with water and ethanol, following the same procedures as in the previous scenarios, using a Google Pixel 4a as the surface. Fig. 6.17 reveals no significant difference in SmartPhOx's performance when using both cameras. This can be attributed to the fact that even relatively affordable off-the-shelf models incorporate fairly advanced camera technology.

6.9.4 Use case 1 : Counterfeit liquor detection

The prevalence of counterfeit liquid food products has become a significant social issue. According to the World Health Organization (WHO), it is estimated that 25% of all alcohol consumed worldwide is counterfeit [230]. There are numerous reports of counterfeit liquid food products, including milk [231], alcoholic beverages [232], and honey [233]. Alcoholic beverages are commonly adulterated by being mixed with substances that can alter its content, such as water or cheap alcohol [234].

To evaluate SmartPhOx' ability to differentiate between authentic alcoholic beverages and counterfeit versions, we conduct two sets of experiments. In the first set, we assess SmartPhOx' performance in what would typically be regarded as the most common counterfeiting scenario. In the second set, we evaluate SmartPhOx' robustness against varying quantities of the counterfeit substance.

2. Corning, known for Gorilla Glass, is the primary manufacturer for screens in most smartphones [229].

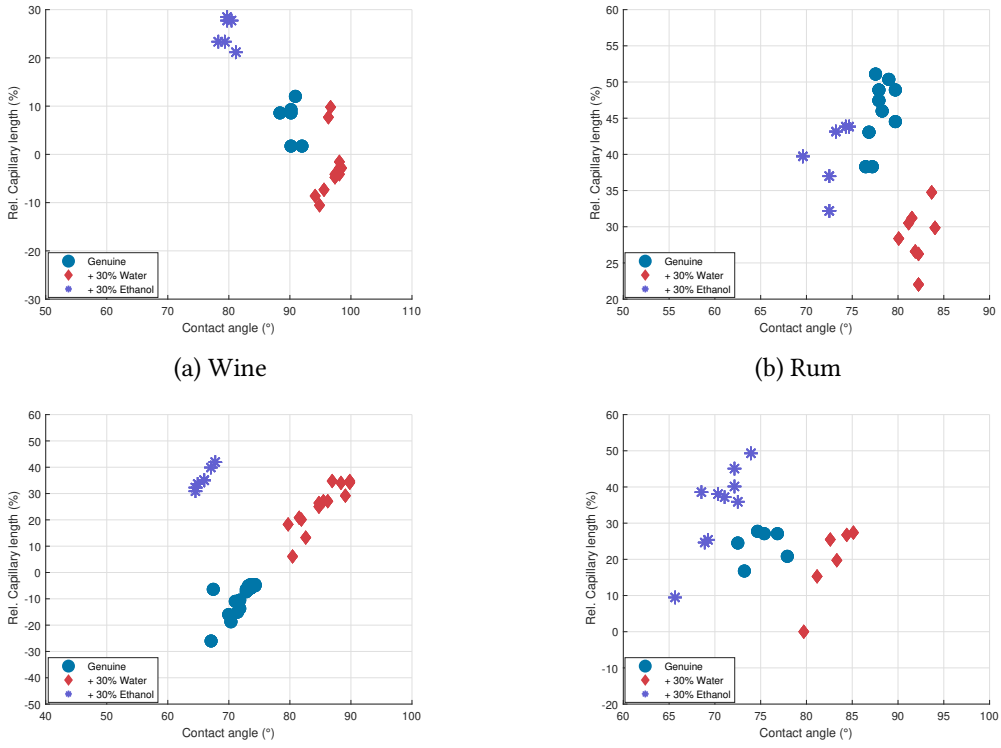

(a) Wine (b) Rum

(c) Whisky (d) Vodka

FIGURE 6.18 – Contact angle and capillary length measurements for four alcoholic beverages adulterated with 30% of water and ethanol.

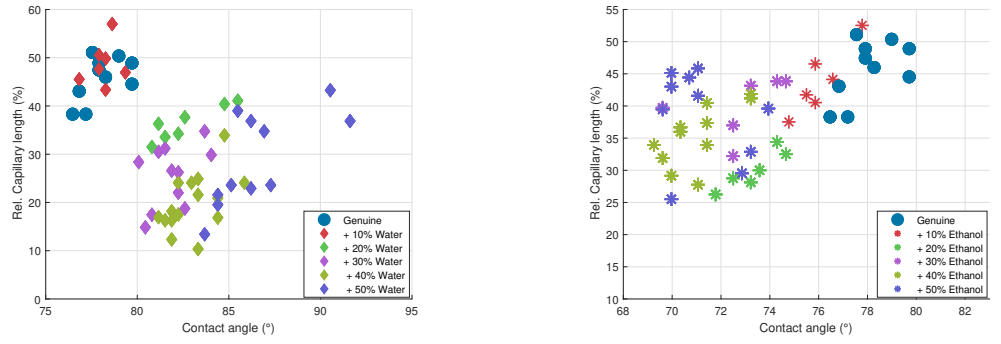

(a) Rum diluted with water. (b) Rum diluted with ethanol.

FIGURE 6.19 – Contact angle and capillary length measurements for rum adulterated with varying percentages of water and ethanol.

Scenario 1 : The typical counterfeiting scenario is rooted in the common practice among counterfeiters, where they dilute authentic products with a minimum of 30% water or cheaper alcohol for economic reasons [24]. Therefore, we perform experiments by diluting four common alcoholic beverages – wine, whisky, rum, and vodka – with either 30% water or 30% ethanol.
Results : Fig. 6.18 depicts the contact angle and capillary length values measured by SmartPhOx for both the authentic and counterfeit versions. The data shows that, as expected, utilizing alcohol (ethanol) as a counterfeiting substance poses a greater challenge for SmartPhOx compared to using water. Nevertheless, the combination of capillary length and contact angle enables the detection of counterfeit alcoholic beverages in both cases.

6.9.5 Use case 2 : Urine testing

Kidney disease is more prevalent among individuals with diabetes or high blood pressure. When a kidney is damaged, certain substances that should not be present in urine begin to excrete. Many of these substances decrease the surface tension of urine. For instance, proteinuria, which occurs when the kidney leaks albumin into the urine, is a concern for individuals with diabetes [235, 236]. One potential application of Droplets is to simplify the monitoring of urine albumin levels for patients with diabetes by acting as an early-warning system. If the test indicates that the albumin level exceeds a safe threshold, the patient can contact their primary care provider for a more comprehensive analysis. In this application, users would use a dedicated testing surface instead of a second smartphone.

To assess the feasibility of Droplets for such a use case, we introduce different levels of egg albumin to samples of healthy human urine and measure their features at various albumin concentrations. Fig. 6.20a illustrates the contact angle of urine solutions with varying levels of albumin. The data demonstrates that Droplets can monitor urine albumin levels by measuring the contact angle of a drop. What is more, Fig. 6.20b shows that by utilizing these two features, we can effectively differentiate between regular urine and urine with an albumin concentration of as little as 44 mg/L. Note, however, that the contact angle difference between urine samples containing 44, 100, and 150 mg/L of protein is approximately 2 degrees. As the data in Section 6.9.3 (Fig. 6.15b) suggests, the current implementation of SmartPhOx can achieve this level of accuracy, but not on all smartphone surfaces.

6.10 Related work

6.10.1 Smartphone based liquid testing

Liquid testing in non-laboratory settings has gained considerable attention in recent years. Some of the early work leverage the interaction between liquid content and radio waves [203, 237-244]. However, these approaches necessitate specialized equipment and setups, including large antennas that are not easily portable. Another body of work leverages commonly available devices like smartphones to analyze liquid properties such

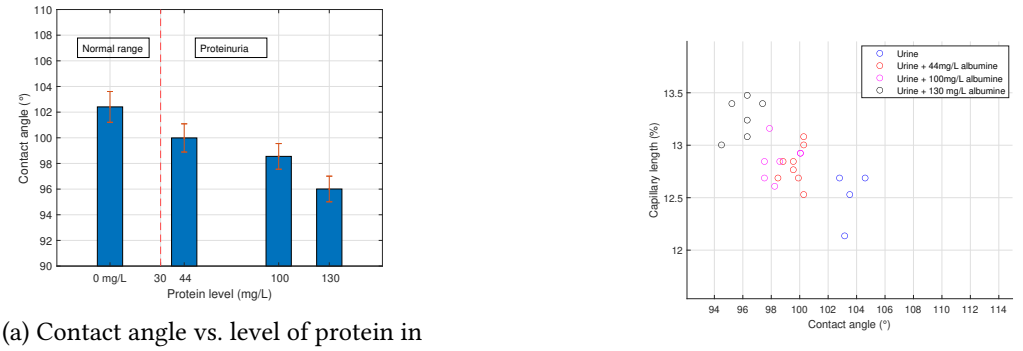

(a) Contact angle vs. level of protein in urine.

(b) Utilizing both features.

FIGURE 6.20 – Urine testing.

as surface tension and viscosity [23, 25, 41, 71, 245-247]. CapCam [23] employs a smartphone camera to estimate liquid surface tension by capturing capillary waves induced by vibrations. However, it requires a paper or plastic cup to produce the intended capillary waves, along with a precise liquid volume. Collecting such a quantity of liquid can restrict its applications, particularly in healthcare scenarios. For example, individuals with anuria typically excrete less than 100 ml of urine daily, making it infeasible to use CapCam. Similarly, Vi-Liquid [41] utilizes a smartphone's vibro-motor and accelerometer to induce and detect vibrations in liquids for viscosity estimation. Viscocam [25] analyzes the sloshing motion of liquid in a cup to estimate its viscosity, while Atke [71] relies on the acoustic permittivity of the liquid, utilizing the microphone and speaker of the phone. LiquidHash [24] detects and tracks the shape and movement of air bubbles inside bottles to identify counterfeit alcohol without requiring them to be opened. Nonetheless, it can only analyze bottles and liquid contents that are semi or fully transparent. It cannot analyze, for instance, red wine or any other liquids contained in non-transparent containers. To the best of our knowledge, [22] is the only work that presents a liquid testing solution based on drops. It utilizes the LiDAR sensor in smartphones to establish a laser speckle system. However, smartphone manufacturers are progressively phasing out LiDAR sensors [208].

System	Sensors	Availability of the sensors	Volume needed	Measured properties	Container-independent	Work on liquid no matter the opacity	Run on smartphone	Contactless	Classification	Fake liquors detection	Urine testing
***Capcam** [23]*	Camera, Flashlight vibro motor	Most of the smartphones	a cup	Surface tension	No	No	Yes	Yes	Yes	Yes	Yes
***Vi-Liquid** [41]*	Accelero-meter, vibro motor	Most of the smartphones	a cup	Viscosity	No	Yes	Yes	No	Yes	No	Yes
***Liquidhash** [24]*	Camera	Most of the smartphones	a cup	Capillary length, Viscosity, Surface tension	No	No	Yes	Yes	No	Yes	No
***Viscocam** [25]*	Camera	Most of the smartphones	a cup	Viscosity	No	No	No	Yes	Yes	No	
***LiDar** [22]*	Lidar	Few brands high end smartphones	a droplet	Viscosity	No container	Yes	Yes	Yes	Yes	No	No
Droplets	***Camera***	***Most of the smartphones***	***a droplet***	***Capillary length, Contact angle***	**No container**	**Yes**	**Yes**	***Yes***	***Yes***	***Yes***	***Yes***

TABLE 6.1 – Comparison of related works.

6.10.2 Sessile drop shape analysis

There is a considerable body of literature on measuring the contact angle of a droplet [211-215, 217, 218]. The typical approach involves analyzing the droplet's profile, identifying the baseline, and calculating the contact angle either through polynomial fitting [211, 212, 214, 218, 248] or by solving the Young-Laplace equation [32, 211, 213-215, 217]. However, these methodologies rely on complex and specialized setups that are not suitable for out-of-laboratory use. None of them are designed to handle images taken under uncontrolled conditions, which often leads to the presence of erroneous data points and, in some cases, the inability to locate the top of the droplet. Droplets' contribution is to introduce solutions to these challenges.

6.11 Conclusion

We presented Droplets, a smartphone-based solution for ubiquitous liquid testing, that utilizes a single drop and relies on a standard camera and gyroscope. The primary innovation of Droplets lies in its ability to differentiate liquids based on their contact angle and capillary length. Drawing on the Young-Laplace equation, we have introduced a method to fit a theoretical model to imperfect drop profiles obtained from smartphone camera images, thereby facilitating the computation of contact angle and capillary length. To account for the challenges posed by uncontrolled experimental environments, Droplets incorporates a virtual assistant designed to assist users in capturing high-quality images of the droplets. Results obtained from testing nine different liquids demonstrate that Droplets achieves an accuracy of 84% in liquid classification. Additionally, our experiments have revealed the potential of Droplets in detecting counterfeit liquors and tracking protein levels in urine.

The current implementation of Droplets has its limitations. Liquid testing is based solely on the shape of the drop but other features like the color could help improve accuracy. Furthermore, in this golden age of artificial intelligence it may be interesting to explore AI approaches for complementing Droplets' algorithms for extracting the contact angle and capillary length from imperfect images and making the virtual assistant more powerful.

Conclusion and Future Work

Conclusion

The smartphone has become an omnipresent tool in our daily lives. It is a device that an increasingly large majority of the population owns, and its features and services have led to the democratization of processing power, information, and telecommunications. In line with this continuity, this thesis focuses on leveraging the smartphone to democratize healthcare.

Throughout the manuscript, we present a methodology for developing health-related sensing systems working on a smartphone. Specifically, we start with a well-defined objective to identify the object of interest and the potentially usable smartphone sensors. We then review literature for relevant existing sensing approach related to the sensor and the object, and after comparison, we decide on the course of action, as demonstrated by our three uses case illustrations :

1. **To measure blood oxygen saturation**, we initially explore the use of finger photoplethysmography (presented in Chapter 2.4.3), a commonly employed sensing technique in previous research. Through experiments conducted in Chapter 4.4, we identify the limitations of the conventional RR method. This leads us to devise an alternative approach based on the RR map, which is introduced in Chapter 4.6.2. We develop a more reliable RR extraction method and demonstrate its effectiveness in accurately estimating SpO2, meeting the FDA's accuracy standards (Chapter 4.9.1).
2. **To measure lung functions**, we do not identify any approaches that meet our user behavior related constraints (user movements) and environmental constraints (ambient noise), prompting us to pursue a new approach. We propose using the pressure sensor to measure lung content when exhaled into an inflatable balloon. We design a setup and algorithms to transform this idea into a complete system (Chapter 5.3), achieving accuracy comparable to clinical spirometer.
3. **To test a single drop of liquid**, We could not find a satisfactory sensing approach using standard smartphone sensors, so we decided to explore an alternative method. We chose vision as it allows us to distinguish between liquid droplets based on their shape (Chapter 6.2). Utilizing the Young-Laplace equation, we developed a model (Chapter 6.2.3.2) and a complete setup (Chapter 6.3) to measure the characteristics of a liquid droplet's shape, such as the contact angle and capillary length. With this approach, we successfully detected differences in protein levels in urine droplets (Chapter 6.9.5).

Overall, the solutions we propose enable smartphone users, regardless of their training or environment, to access and benefit from medical technologies related to the addressed problems. This represents a significant step towards our vision of democratizing healthcare and empowering users to enhance the starting point of their healthcare journey, as discussed in the introduction (Chapter 1.1).

Firstly, SmartPhOx enables smartphone users, under the recommendation of their

healthcare provider, to frequently measure their SpO2, thereby detecting any timely deterioration in their health, especially for individuals with chronic lung or cardiac diseases.

Secondly, with BandS-Spi, smartphone users can perform reliable spirometry tests using a cheap inflatable balloon, without the presence of a clinician, relying solely on the guidance provided by the tool.

Lastly, with Droplets, smartphone users can test different liquids, such as urine, to detect abnormally high protein levels, prompting them to seek medical attention. They can also check the suitability or verify the authenticity of various beverages.

Future work

In addition to the individual-centered approach we advocate for in democratizing and continuous healthcare, the future of mHealth holds promise on a broader scale. With the widespread ownership of smartphones, the healthcare system could be organized nationally around this technology. Centralizing health-related data from each individual could lead to improved traceability of disease progression and significant benefits for research, especially in public health. For instance, early disease detection, real-time pandemic monitoring, and understanding the impact of demographic and hereditary data on different illnesses could be achieved. Furthermore, investigating why certain populations with similar early signs may not develop diseases could uncover better health practices hidden in lifestyle habits.

While this crowd healthcare perspective offers societal promise, it also poses various scientific and ethical challenges. Ethically, privacy must be a top priority when implementing such policies. Anonymizing data, obtaining informed consent, and ensuring data cannot be linked to identities are critical.

Scientifically, several challenges arise :

— Handling the massive amount of data necessitates robust and efficient infrastructure.

— Establishing links between historical health related data and future diseases is complex.

— Developing appropriate models to detect diseases years in advance is not straightforward.

To achieve this vision, cloud computing, IT security, and artificial intelligence are key research areas. Cloud computing is crucial for managing and storing vast amounts of data, ensuring scalability and accessibility for millions of smartphone users.

IT security is essential to safeguard sensitive medical information stored in the cloud, using encryption and access controls to protect individual identities.

Artificial intelligence plays a pivotal role in analyzing extensive healthcare data, identifying patterns, and forecasting health conditions, enabling timely interventions for better disease management and prevention.

Advancing research in these areas has the potential to revolutionize public healthcare and improve medical outcomes, while responsible handling of ethical concerns, data privacy, and governance ensures societal benefit.

Publications

Published

— F. Kateu, G. Jakllari and E. Chaput, "SmartPhOx : Smartphone-Based Pulse Oximetry Using a Meta-Region Of Interest," *IEEE International Conference on Pervasive Computing and Communications (PerCom)*, Pisa, Italy, 2022, pp. 130-140, doi:10.1109/PerCom53586.2022.9762399. **Best paper candidate.**

— Firmin Kateu, Gentian Jakllari, Emmanuel Chaput, "Unobstrusive smartphone-based oxygen saturation measurement using a Meta-Region of interest", *Pervasive and Mobile Computing*, Volume 88, 2023, 101741, ISSN 1574-1192, doi:https://doi.org/10.1016/j.pmcj.2022.101741.

Under review

— F. Kateu, E. Chaput and G. Jakllari, "BandS-SPI : Person with Balloon and Smartphone Estimating their Lung Function", *Proceedings of the ACM on Interactive, Mobile, Wearable and Ubiquitous Technologies (IMWUT)*, 2023 — Major revisions

— F. Kateu, G. Jakllari and E. Chaput, "Droplets : Smartphone-Based Single-Drop Liquid Testing Beyond the Laboratory", *ACM International Conference on Embedded Networked Sensor Systems (SenSys)*, 2023 — Submitted.

Acronyms

ARDS Acute Respiratory Distress Syndrome. 62

CNN Convolution Neural Network. 32, 33
COPD Chronic Obstructive Pulmonary Disease. 20, 81
CSI Channel State Information. 22, 23
CWT Continuous Wavelet Transform. 26

DNN Deep Neural Network. 32

GPS Global Positioning System. 11
GPUs Graphics Processing Units. 11
GRU Gated Recurrent Unit. 34

LOG Laplacian of Gaussian. 30
LSTM Long Short-Term Memory. 33

NFC Near Field Communication. 11

PCA Principal component Analysis. 32
PPG Photoplethysmogram. 17, 22, 26, 28, 46, 61
PSD Power Spectral Density. 26, 27

RFID Radio Frequency Identification. 11, 12
RNN Recurrent Neural Network. 33
RSSI Signal Received Strengh Indicator. 23

SARS-CoV-2 Coronavirus. 20
SNR Signal to Noise Ratio. 19, 61
SVM Support Vector Machines. 31

TOI Transdermal optical imaging. 16, 22

Bibliography

[1] Tatum S Simonson et al. “Silent hypoxaemia in COVID-19 patients”. In : *The Journal of physiology* 599.4 (2021), p. 1057-1065 (cf. p. 1).

[2] Maria Tereza da Costa Oliveira, Maria do Rosario Dias de Oliveira Latorre et Dirceu Bartolomeu Greco. “The impact of late diagnosis on the survival of patients following their first AIDS-related hospitalization in Belo Horizonte, Brazil”. en. In : *AIDS Care* 24.5 (2012), p. 635-641 (cf. p. 2).

[3] Adrian Gheorghe et al. “Economic impact of avoidable cancer deaths caused by diagnostic delay during the COVID-19 pandemic: A national population-based modelling study in England, UK”. In : *European Journal of Cancer* 152 (2021), p. 233-242. issn : 0959-8049. doi : https://doi.org/10.1016/j.ejca.2021.04.019. url : https://www.sciencedirect.com/science/article/pii/S0959804921002501 (cf. p. 2).

[4] Luke Eckersley et al. “Timing of diagnosis affects mortality in critical congenital heart disease”. In : *Archives of disease in childhood* 101.6 (2016), p. 516-520 (cf. p. 2).

[5] Lucienne TQ Cardoso et al. “Impact of delayed admission to intensive care units on mortality of critically ill patients: a cohort study”. In : *Critical care* 15.1 (2011), p. 1-8 (cf. p. 2).

[6] *Baromètre du numérique 2019*. https://www.credoc.fr/publications/barometre-du-numerique-2019. Accessed: 2023-03-20 (cf. p. 2-5).

[7] Blackberry. *https://www.blackberry.com/us/en/products/devices*. 2023. url : https://www.blackberry.com/us/en/products/devices (visité le 03/05/2023) (cf. p. 2).

[8] *L’adoption du smartphone en Afrique*. https://www.pwc.fr/fr/decryptages/transformation/mobile-toujours-cle-du-digital-en-afrique.html. Accessed: 2023-03-20 (cf. p. 3, 4).

[9] Nam Bui et al. “PhO2: Smartphone Based Blood Oxygen Level Measurement Systems Using Near-IR and RED Wave-Guided Light”. In : *Proceedings of the 15th ACM Conference on Embedded Network Sensor Systems*. SenSys ’17. Delft, Netherlands : Association for Computing Machinery, 2017. isbn : 9781450354592. doi : 10.1145/3131672.3131696. url : https://doi.org/10.1145/3131672.3131696 (cf. p. 3-5, 13, 16, 17, 22, 35).

[10] Eric C. Larson et al. “SpiroSmart: Using a Microphone to Measure Lung Function on a Mobile Phone”. In : *Proceedings of the 2012 ACM Conference on Ubiquitous Computing*. UbiComp ’12. Pittsburgh, Pennsylvania : Association for Computing Machinery, 2012, 280–289. isbn : 9781450312240. doi : 10.1145/2370216.2370261. url : https://doi.org/10.1145/2370216.2370261 (cf. p. 3, 12, 13, 20, 63, 67, 77, 78).

[11] Edward Jay Wang et al. “HemaApp: Noninvasive Blood Screening of Hemoglobin Using Smartphone Cameras”. In : *Proceedings of the 2016 ACM International Joint Conference on Pervasive and Ubiquitous Computing*. UbiComp ’16. Heidelberg, Germany : ACM, 2016, p. 593-604. ISBN : 978-1-4503-4461-6. DOI : 10.1145/2971648.2971653. URL : http://doi.acm.org/10.1145/2971648.2971653 (cf. p. 3, 4, 16, 17).

[12] Sumit Majumder et M. Jamal Deen. “Smartphone Sensors for Health Monitoring and Diagnosis”. In : *Sensors* 19.9 (2019), p. 2164. ISSN : 1424-8220. DOI : 10.3390/s19092164. URL : http://dx.doi.org/10.3390/s19092164 (cf. p. 3, 18).

[13] Lorenz Frey, Carlo Menon et Mohamed Elgendi. “Blood pressure measurement using only a smartphone”. In : *npj Digital Medicine* 5.1 (2022), p. 86. ISSN : 2398-6352. DOI : 10.1038/s41746-022-00629-2. URL : https://doi.org/10.1038/s41746-022-00629-2 (cf. p. 3, 4).

[14] Jonathan Mayes et al. “How smartphone technology is changing healthcare in developing countries”. In : *The Columbia University Journal of Global Health* 6.2 (2016), p. 36-38 (cf. p. 4).

[15] Kevin Jiokeng, Gentian Jakllari et André-Luc Beylot. “HandRate: Heart Rate Monitoring While Simply Holding a Smartphone”. In : *2021 IEEE International Conference on Pervasive Computing and Communications (PerCom)*. 2021, p. 1-11. DOI : 10.1109/PERCOM50583.2021.9439134 (cf. p. 4, 16, 19, 28, 34).

[16] Gaobo Zhang et al. “A Noninvasive Blood Glucose Monitoring System Based on Smartphone PPG Signal Processing and Machine Learning”. In : *IEEE Transactions on Industrial Informatics* 16.11 (2020), p. 7209-7218. DOI : 10.1109/TII.2020.2975222 (cf. p. 4).

[17] Hiroshi Nakano et al. “Monitoring sound to quantify snoring and sleep apnea severity using a smartphone: proof of concept”. In : *Journal of Clinical Sleep Medicine* 10.1 (2014), p. 73-78 (cf. p. 4).

[18] Olli Lahdenoja et al. “Atrial fibrillation detection via accelerometer and gyroscope of a smartphone”. In : *IEEE Journal of Biomedical and Health Informatics* 22.1 (2017), p. 108-118 (cf. p. 4).

[19] Nasser F BinDhim et al. “Depression screening via a smartphone app: cross-country user characteristics and feasibility”. In : *Journal of the American Medical Informatics Association* 22.1 (oct. 2014), p. 29-34. ISSN : 1067-5027. DOI : 10.1136/amiajnl-2014-002840. eprint : https://academic.oup.com/jamia/article-pdf/22/1/29/34145252/amiajnl-2013-002840.pdf. URL : https://doi.org/10.1136/amiajnl-2014-002840 (cf. p. 4, 18).

[20] Alex Mariakakis et al. “PupilScreen: using smartphones to assess traumatic brain injury”. In : *Proceedings of the ACM on Interactive, Mobile, Wearable and Ubiquitous Technologies* 1.3 (2017), p. 1-27 (cf. p. 4).

[21] Andong Zhan et al. “Using Smartphones and Machine Learning to Quantify Parkinson Disease Severity: The Mobile Parkinson Disease Score”. In : *JAMA Neurology* 75.7 (juill. 2018), p. 876-880. ISSN : 2168-6149. DOI : 10.1001/jamaneurol.2018.0809. eprint : https://jamanetwork.com/journals/jamaneurology/articlepdf/2676504/jamaneurology_zhan_2018_br_180003.pdf. URL : https://doi.org/10.1001/jamaneurol.2018.0809 (cf. p. 4).

[22] Justin Chan et al. “Testing a Drop of Liquid Using Smartphone LiDAR”. In : *Proc. ACM Interact. Mob. Wearable Ubiquitous Technol.* 6.1 (2022). DOI : 10.1145/3517256. URL : https://doi.org/10.1145/3517256 (cf. p. 4, 16, 18, 35, 83, 105).

[23] Shichao Yue et Dina Katabi. “Liquid Testing with Your Smartphone”. In : *Proceedings of the 17th Annual International Conference on Mobile Systems, Applications, and Services*. MobiSys ’19. Seoul, Republic of Korea : Association for Computing Machinery, 2019, 275–286. ISBN : 9781450366618. DOI : 10.1145/3307334.3326078. URL : https://doi.org/10.1145/3307334.3326078 (cf. p. 4, 9, 15, 16, 21, 82, 105).

[24] Bangjie Sun et al. “Detecting Counterfeit Liquid Food Products in a Sealed Bottle Using a Smartphone Camera”. In : *Proceedings of the 20th Annual International Conference on Mobile Systems, Applications and Services*. MobiSys ’22. Portland, Oregon : Association for Computing Machinery, 2022, 42–55. ISBN : 9781450391856. DOI : 10.1145/3498361.3539776. URL : https://doi.org/10.1145/3498361.3539776 (cf. p. 4, 104, 105).

[25] Kecheng An, Qian Zhang et Elaine Kwong. “ViscoCam: Smartphone-Based Drink Viscosity Control Assistant for Dysphagia Patients”. In : *Proc. ACM Interact. Mob. Wearable Ubiquitous Technol.* 5.1 (2021). DOI : 10.1145/3448109. URL : https://doi.org/10.1145/3448109 (cf. p. 4, 16, 18, 19, 82, 105).

[26] Md Asif Ahamed, Md Kamrul Hasan et Md Shahabul Alam. “Design and implementation of low cost ECG monitoring system for the patient using smartphone”. In : *2015 International Conference on Electrical & Electronic Engineering (ICEEE)*. IEEE. 2015, p. 261-264 (cf. p. 5).

[27] Xingzhe Song et al. “SpiroSonic: Monitoring Human Lung Function via Acoustic Sensing on Commodity Smartphones”. In : *Proceedings of the 26th Annual International Conference on Mobile Computing and Networking*. MobiCom ’20. London, United Kingdom : Association for Computing Machinery, 2020. ISBN : 9781450370851. DOI : 10.1145/3372224.3419209. URL : https://doi.org/10.1145/3372224.3419209 (cf. p. 5, 15, 16, 20, 21, 63, 67, 78).

[28] Jishnu Dey, Aman Gaurav et Vijay N. Tiwari. “InstaBP: Cuff-less Blood Pressure Monitoring on Smartphone using Single PPG Sensor”. In : *2018 40th Annual International Conference of the IEEE Engineering in Medicine and Biology Society (EMBC)*. 2018, p. 5002-5005. DOI : 10.1109/EMBC.2018.8513189 (cf. p. 5, 16, 28).

[29] D. F. Swinehart. "The Beer-Lambert Law". In : *Journal of Chemical Education* 39.7 (1962), p. 333. issn : 0021-9584. doi : 10.1021/ed039p333. url : https://doi.org/10.1021/ed039p333 (cf. p. 6, 17, 37).

[30] U.S FOOD & DRUG ADMINISTRATION. *Pulse Oximeters - Premarket Notification Submissions [510(k)s]: Guidance for Industry and Food and Drug Administration Staff*. 2013. url : https://www.fda.gov/regulatory-information/search-fda-guidance-documents/pulse-oximeters-premarket-notification-submissions-510ks-guidance-industry-and-food-and-drug (visité le 28/05/2021) (cf. p. 6, 42, 43, 57).

[31] Aurélien F. Stalder et al. "Low-bond axisymmetric drop shape analysis for surface tension and contact angle measurements of sessile drops". In : *Colloids and Surfaces A: Physicochemical and Engineering Aspects* 364.1 (2010), p. 72-81. issn : 0927-7757. doi : https://doi.org/10.1016/j.colsurfa.2010.04.040. url : https://www.sciencedirect.com/science/article/pii/S0927775710002761 (cf. p. 7, 83, 87).

[32] Siddarth Srinivasan, Gareth McKinley et Robert Cohen. "Assessing the Accuracy of Contact Angle Measurements for Sessile Drops on Liquid-Repellent Surfaces". In : *Langmuir : the ACS journal of surfaces and colloids* 27 (sept. 2011), p. 13582-9. doi : 10.1021/la2031208 (cf. p. 7, 88, 89, 106).

[33] Anand Chandrasekhar et al. "An iPhone Application for Blood Pressure Monitoring via the Oscillometric Finger Pressing Method". In : *Scientific Reports* 8.1 (2018), p. 13136. issn : 2045-2322. doi : 10.1038/s41598-018-31632-x. url : https://doi.org/10.1038/s41598-018-31632-x (cf. p. 9, 18).

[34] YOHANN POIRON. *Le Google Pixel 8 Pro inclura un thermomètre pour mesurer la température corporelle*. 2023. url : https://www.blog-nouvelles-technologies.fr/261992/google-pixel-8-pro-inclura-un-thermometre/ (visité le 28/05/2021) (cf. p. 10).

[35] *Qu'est-ce que Samsung DeX et comment le connecter à un appareil?* https://www.samsung.com/fr/support/mobile-devices/qu-est-ce-que-samsung-dex-et-comment-le-connecter-a-un-appareil/. Accessed: 2023-03-20 (cf. p. 11).

[36] Fen Miao et al. "A Wearable Context-Aware ECG Monitoring System Integrated with Built-in Kinematic Sensors of the Smartphone". In : *Sensors* 15.5 (2015), p. 11465-11484. issn : 1424-8220. doi : 10.3390/s150511465. url : https://www.mdpi.com/1424-8220/15/5/11465 (cf. p. 12, 16, 18, 35).

[37] Mayank Goel et al. "SpiroCall: Measuring Lung Function over a Phone Call". In : *Proceedings of the 2016 CHI Conference on Human Factors in Computing Systems*. CHI '16. San Jose, California, USA : Association for Computing Machinery, 2016, 5675–5685. isbn : 9781450333627. doi : 10.1145/2858036.2858401. url : https://doi.org/10.1145/2858036.2858401 (cf. p. 12).

[38] Chandrasekhar A et al. “Formulas to Explain Popular Oscillometric Blood Pressure Estimation Algorithms”. In : (2019), p. 1-10. DOI : 10.3389/fphys.2019.01415 (cf. p. 13).

[39] Varun VISWANATH, Jake GARRISON et Shwetak N. PATEL. “SpiroConfidence: Determining the Validity of Smartphone Based Spirometry Using Machine Learning”. In : *2018 40th Annual International Conference of the IEEE Engineering in Medicine and Biology Society (EMBC)* (2018), p. 5499-5502 (cf. p. 13, 63, 67).

[40] Shubham Pratap SINGH et al. “Contactless and hassle free real time heart rate measurement with facial video”. In : *Journal of Cardiac Critical Care TSS* 1.01 (2017), p. 024-029 (cf. p. 13).

[41] Yongzhi HUANG et al. “Vi-Liquid: Unknown Liquid Identification with Your Smartphone Vibration”. In : *Proceedings of the 27th Annual International Conference on Mobile Computing and Networking*. MobiCom ’21. New Orleans, Louisiana : Association for Computing Machinery, 2021, 174–187. ISBN : 9781450383424. DOI : 10.1145/3447993.3448621. URL : https://doi.org/10.1145/3447993.3448621 (cf. p. 14, 19, 82, 105).

[42] Leysan NURGALIEVA, David O’CALLAGHAN et Gavin DOHERTY. “Security and Privacy of mHealth Applications: A Scoping Review”. In : *IEEE Access* 8 (2020), p. 104247-104268. DOI : 10.1109/ACCESS.2020.2999934 (cf. p. 14).

[43] Miles E SMID et Dennis K BRANSTAD. “Data encryption standard: past and future”. In : *Proceedings of the IEEE* 76.5 (1988), p. 550-559 (cf. p. 14).

[44] Edward Jay WANG et al. “Seismo: Blood Pressure Monitoring Using Built-in Smartphone Accelerometer and Camera”. In : *Proceedings of the 2018 CHI Conference on Human Factors in Computing Systems*. CHI ’18. Montreal QC, Canada : Association for Computing Machinery, 2018, 1–9. ISBN : 9781450356206. DOI : 10.1145/3173574.3173999. URL : https://doi.org/10.1145/3173574.3173999 (cf. p. 15-18).

[45] Justin CHAN et al. “Micro-mechanical blood clot testing using smartphones”. In : *Nature Communications* 13.1 (2022), p. 831. DOI : 10.1038/s41467-022-28499-y. URL : https://doi.org/10.1038/s41467-022-28499-y (cf. p. 15).

[46] Amtul Haq AYESHA, Donghao QIAO et Farhana ZULKERNINE. “Heart Rate Monitoring Using PPG With Smartphone Camera”. In : *2021 IEEE International Conference on Bioinformatics and Biomedicine (BIBM)*. IEEE. 2021, p. 2985-2991 (cf. p. 16, 17, 22).

[47] Xin LIU et al. “MobilePhys”. In : *Proceedings of the ACM on Interactive, Mobile, Wearable and Ubiquitous Technologies* 6.1 (2022), p. 1-23. DOI : 10.1145/3517225. URL : https://doi.org/10.1145%2F3517225 (cf. p. 16).

[48] Donghao Qiao et al. "Measuring Heart Rate and Heart Rate Variability with Smartphone Camera". In : *2021 22nd IEEE International Conference on Mobile Data Management (MDM)*. 2021, p. 248-249. DOI : 10.1109/MDM52706.2021.00049 (cf. p. 17).

[49] Gaobo Zhang et al. "A noninvasive blood glucose monitoring system based on smartphone PPG signal processing and machine learning". In : *IEEE Transactions on Industrial Informatics* 16.11 (2020), p. 7209-7218 (cf. p. 17, 22).

[50] Andrea Nemcova et al. "Monitoring of heart rate, blood oxygen saturation, and blood pressure using a smartphone". In : *Biomedical Signal Processing and Control* 59 (2020), p. 101928 (cf. p. 17).

[51] Aman Gaurav et al. "Cuff-less PPG based continuous blood pressure monitoring—A smartphone based approach". In : *2016 38th annual international conference of the IEEE engineering in medicine and biology society (EMBC)*. IEEE. 2016, p. 607-610 (cf. p. 17, 22, 28).

[52] Andrea Nemcova et al. "Monitoring of heart rate, blood oxygen saturation, and blood pressure using a smartphone". In : *Biomedical Signal Processing and Control* 59 (2020), p. 101928 (cf. p. 17, 22).

[53] Takehiro Yamakoshi, Peter Rolfe et Ken-ichi Yamakoshi. "Cuffless blood pressure estimation based on haemodynamic principles: progress towards mobile healthcare". In : *PeerJ* 9 (2021), e11479 (cf. p. 17, 28).

[54] Lilian De Greef et al. "Bilicam: using mobile phones to monitor newborn jaundice". In : *Proceedings of the 2014 ACM International Joint Conference on Pervasive and Ubiquitous Computing*. 2014, p. 331-342 (cf. p. 18).

[55] Jack W O'Sullivan et al. "Accuracy of smartphone camera applications for detecting atrial fibrillation: a systematic review and meta-analysis". In : *JAMA network open* 3.4 (2020), e202064-e202064 (cf. p. 18).

[56] Cédric Rat et al. "Use of smartphones for early detection of melanoma: systematic review". In : *Journal of medical Internet research* 20.4 (2018), e135 (cf. p. 18).

[57] Elizabeth Chao, Chelsea K Meenan et Laura K Ferris. "Smartphone-based applications for skin monitoring and melanoma detection". In : *Dermatologic clinics* 35.4 (2017), p. 551-557 (cf. p. 18).

[58] Mojtaba Jafari Tadi et al. "Seismocardiography: Toward heart rate variability (HRV) estimation". In : *2015 IEEE International Symposium on Medical Measurements and Applications (MeMeA) Proceedings*. 2015, p. 261-266. DOI : 10.1109/MeMeA.2015.7145210 (cf. p. 19).

[59] Bernardo Silva et Rui Neto Marinheiro. "Non-invasive monitoring with Ballistocardiographic sensors for sleep management". In : *2021 Telecoms Conference (ConfTELE)*. IEEE. 2021, p. 1-6 (cf. p. 19).

[60] Javier Hernandez, Daniel J. McDuff et Rosalind W. Picard. "Biophone: Physiology monitoring from peripheral smartphone motions". In : *2015 37th Annual International Conference of the IEEE Engineering in Medicine and Biology Society (EMBC)*. 2015, p. 7180-7183. doi : 10.1109/EMBC.2015.7320048 (cf. p. 19).

[61] Wafaa Aljbawi, Sami Simmons et Visara Urovi. *Developing a multi-variate prediction model for the detection of COVID-19 from Crowd-sourced Respiratory Voice Data*. Sept. 2022. doi : 10.48550/arXiv.2209.03727 (cf. p. 20).

[62] Hanbin Zhang et al. "PDVocal: Towards Privacy-preserving Parkinson's Disease Detection using Non-speech Body Sounds". In : nov. 2019 (cf. p. 20).

[63] Amir Amiri et al. "Mobile Phonocardiogram Diagnosis in Newborns Using Support Vector Machine". In : *Healthcare* 5.1 (2017), p. 16. issn : 2227-9032. doi : 10.3390/healthcare5010016. url : http://dx.doi.org/10.3390/healthcare5010016 (cf. p. 20).

[64] Amir Mohammad Amiri et al. "PhonoSys: Mobile Phonocardiography Diagnostic System for Newborns". In : *EAI Endorsed Transactions on Mobile Communications and Applications* 3.10 (juin 2017). doi : 10.4108/eai.14-10-2015.2261614 (cf. p. 20).

[65] Gábor Fodor et al. "Screening for congenital heart diseases by murmurs using telemedical phonocardiography". In : *2012 Annual International Conference of the IEEE Engineering in Medicine and Biology Society*. 2012, p. 6100-6103. doi : 10.1109/EMBC.2012.6347385 (cf. p. 20).

[66] Ayşe Arslan et Oktay Yildiz. "Automated Auscultative Diagnosis System for Evaluation of Phonocardiogram Signals Associated with Heart Murmur Diseases". In : *Gazi University Journal of Science* 31 (mars 2018) (cf. p. 20).

[67] Rajalakshmi Nandakumar et al. "FingerIO: Using Active Sonar for Fine-Grained Finger Tracking". In : *Proceedings of the 2016 CHI Conference on Human Factors in Computing Systems*. CHI '16. San Jose, California, USA : Association for Computing Machinery, 2016, 1515–1525. isbn : 9781450333627. doi : 10.1145/2858036.2858580. url : https://doi.org/10.1145/2858036.2858580 (cf. p. 20).

[68] Ke Sun et al. "VSkin: Sensing Touch Gestures on Surfaces of Mobile Devices Using Acoustic Signals". In : *Proceedings of the 24th Annual International Conference on Mobile Computing and Networking*. MobiCom '18. New Delhi, India : Association for Computing Machinery, 2018, 591–605. isbn : 9781450359030. doi : 10.1145/3241539.3241568. url : https://doi.org/10.1145/3241539.3241568 (cf. p. 20).

[69] Zhenyu Chen et al. "Unobtrusive sleep monitoring using smartphones". In : *2013 7th International Conference on Pervasive Computing Technologies for Healthcare and Workshops*. 2013, p. 145-152 (cf. p. 20).

[70] Tian Hao, Guoliang Xing et Gang Zhou. "ISleep: Unobtrusive Sleep Quality Monitoring Using Smartphones". In : *Proceedings of the 11th ACM Conference on Embedded Networked Sensor Systems*. SenSys '13. Roma, Italy : Association for Computing Machinery, 2013. ISBN : 9781450320276. DOI : 10.1145/2517351.2517359. URL : https://doi.org/10.1145/2517351.2517359 (cf. p. 20).

[71] Xue Sun et al. "Akte-Liquid: Acoustic-Based Liquid Identification with Smartphones". In : *ACM Trans. Sen. Netw.* 19.1 (2023). ISSN : 1550-4859. DOI : 10.1145/3551640. URL : https://doi.org/10.1145/3551640 (cf. p. 21, 82, 105).

[72] Bo Peng et al. "A smartphone-based colorimetry after dispersive liquid–liquid microextraction for rapid quantification of calcium in water and food samples". In : *Microchemical Journal* 149 (2019), p. 104072 (cf. p. 21).

[73] Firmin Kateu, Gentian Jakllari et Emmanuel Chaput. "Smartphox: Smartphone-based pulse oximetry using a meta-region of interest". In : *2022 IEEE International Conference on Pervasive Computing and Communications (PerCom)*. IEEE. 2022, p. 130-140 (cf. p. 22).

[74] Francesco Lamonaca et al. "Application of the artificial neural network for blood pressure evaluation with smartphones". In : *2013 IEEE 7th International Conference on Intelligent Data Acquisition and Advanced Computing Systems (IDAACS)*. T. 1. IEEE. 2013, p. 408-412 (cf. p. 22).

[75] Ahsen Tahir et al. "WiFreeze: Multiresolution Scalograms for Freezing of Gait Detection in Parkinson's Leveraging 5G Spectrum with Deep Learning". In : *Electronics* 8.12 (2019), p. 1433. ISSN : 2079-9292. DOI : 10.3390/electronics8121433. URL : http://dx.doi.org/10.3390/electronics8121433 (cf. p. 23).

[76] Shih-Yuan Chen et Chi-Lun Lin. "Subtle Motion Detection Using Wi-Fi for Hand Rest Tremor in Parkinson's Disease". In : *2022 44th Annual International Conference of the IEEE Engineering in Medicine & Biology Society (EMBC)*. IEEE. 2022, p. 1774-1777 (cf. p. 23).

[77] Yuqing Yin et al. "Ubiquitous Smartphone-Based Respiration Sensing With Wi-Fi Signal". In : *IEEE Internet of Things Journal* 9.2 (2022), p. 1479-1490. DOI : 10.1109/JIOT.2021.3088338 (cf. p. 23).

[78] Steven M. Hernandez et Eyuphan Bulut. "Performing WiFi Sensing with Off-the-shelf Smartphones". In : *2020 IEEE International Conference on Pervasive Computing and Communications Workshops (PerCom Workshops)*. 2020, p. 1-3. DOI : 10.1109/PerComWorkshops48775.2020.9156194 (cf. p. 23).

[79] Alexander Tataraidze, Roman Olesyuk et Mikhail Pikhletsky. "Can we monitor breathing during sleep via Wi-Fi on smartphone?" In : *2019 41st Annual International Conference of the IEEE Engineering in Medicine and Biology Society (EMBC)*. IEEE. 2019, p. 6710-6713 (cf. p. 23).

[80] Daqing Zhang et al. “Anti-fall: A non-intrusive and real-time fall detector leveraging CSI from commodity WiFi devices”. In : *Inclusive Smart Cities and e-Health: 13th International Conference on Smart Homes and Health Telematics, ICOST 2015, Geneva, Switzerland, June 10-12, 2015, Proceedings 13*. Springer. 2015, p. 181-193 (cf. p. 23).

[81] Xuefeng Liu et al. “Wi-sleep: Contactless sleep monitoring via wifi signals”. In : *2014 IEEE Real-Time Systems Symposium*. IEEE. 2014, p. 346-355 (cf. p. 23).

[82] William H Press et Saul A Teukolsky. “Savitzky-Golay smoothing filters”. In : *Computers in Physics* 4.6 (1990), p. 669-672 (cf. p. 24).

[83] Lawrence J Christiano et Terry J Fitzgerald. “The band pass filter”. In : *international economic review* 44.2 (2003), p. 435-465 (cf. p. 25).

[84] Walter Karlen et al. “Photoplethysmogram signal quality estimation using repeated Gaussian filters and cross-correlation”. In : *Physiological measurement* 33.10 (2012), p. 1617 (cf. p. 25).

[85] Rudolph Emil Kalman. “A New Approach to Linear Filtering and Prediction Problems”. In : *Transactions of the ASME–Journal of Basic Engineering* 82.Series D (1960), p. 35-45 (cf. p. 25).

[86] Salomon Bochner et Komaravolu Chandrasekharan. “Fourier transforms”. 19. Princeton University Press, 1949 (cf. p. 26).

[87] Richard N Youngworth, Benjamin B Gallagher et Brian L Stamper. “An overview of power spectral density (PSD) calculations”. In : *Optical manufacturing and testing VI* 5869 (2005), p. 206-216 (cf. p. 26).

[88] Luís Aguiar-Conraria et Maria Joana Soares. “The continuous wavelet transform: A primer”. Rapp. tech. NIPE-Universidade do Minho, 2011 (cf. p. 26).

[89] Vairavan Srinivasan et al. “Artificial neural network based epileptic detection using time-domain and frequency-domain features”. In : *Journal of Medical Systems* 29 (2005), p. 647-660 (cf. p. 28).

[90] Xiaorong Ding et al. “Pulse transit time based continuous cuffless blood pressure estimation: A new extension and a comprehensive evaluation”. In : *Scientific reports* 7.1 (2017), p. 11554 (cf. p. 28).

[91] Ramakrishna Mukkamala et al. “Toward Ubiquitous Blood Pressure Monitoring via Pulse Transit Time: Theory and Practice”. In : *IEEE Transactions on Biomedical Engineering* 62.8 (2015), p. 1879-1901. doi : 10.1109/TBME.2015.2441951 (cf. p. 28).

[92] Manuja Sharma et al. “Cuff-Less and Continuous Blood Pressure Monitoring: A Methodological Review”. In : *Technologies* 5.2 (2017). issn : 2227-7080. doi : 10.3390/technologies5020021. url : https://www.mdpi.com/2227-7080/5/2/21 (cf. p. 28).

[93] Mohammed Diykh, Yan Li et Peng Wen. "EEG sleep stages classification based on time domain features and structural graph similarity". In : *IEEE Transactions on Neural Systems and Rehabilitation Engineering* 24.11 (2016), p. 1159-1168 (cf. p. 28).

[94] Lina Li et al. "Classification of heart sound signals with BP neural network and logistic regression". In : *2017 Chinese Automation Congress (CAC)*. IEEE. 2017, p. 7380-7383 (cf. p. 28).

[95] Alle Meije Wink et Jos BTM Roerdink. "Denoising functional MR images: a comparison of wavelet denoising and Gaussian smoothing". In : *IEEE transactions on medical imaging* 23.3 (2004), p. 374-387 (cf. p. 29).

[96] Chin-Chen Chang, Ju-Yuan Hsiao et Chih-Ping Hsieh. "An adaptive median filter for image denoising". In : *2008 Second international symposium on intelligent information technology application*. T. 2. IEEE. 2008, p. 346-350 (cf. p. 29).

[97] Devanand Bhonsle, Vivek Chandra et GR Sinha. "Medical image denoising using bilateral filter". In : *International Journal of Image, Graphics and Signal Processing* 4.6 (2012), p. 36 (cf. p. 29).

[98] Ioannis Pitas et A Venetsanopoulos. "Nonlinear mean filters in image processing". In : *IEEE transactions on acoustics, speech, and signal processing* 34.3 (1986), p. 573-584 (cf. p. 29).

[99] John Canny. "A Computational Approach to Edge Detection". In : *IEEE Transactions on Pattern Analysis and Machine Intelligence* PAMI-8.6 (1986), p. 679-698. doi : 10.1109/TPAMI.1986.4767851 (cf. p. 29, 89).

[100] Suzhen Yuan et al. "Fast Laplacian of Gaussian Edge Detection Algorithm for Quantum Images". In : *2019 IEEE International Conferences on Ubiquitous Computing & Communications (IUCC) and Data Science and Computational Intelligence (DSCI) and Smart Computing, Networking and Services (SmartCNS)*. 2019, p. 798-802. doi : 10.1109/IUCC/DSCI/SmartCNS.2019.00162 (cf. p. 30).

[101] N. Kanopoulos, N. Vasanthavada et R.L. Baker. "Design of an image edge detection filter using the Sobel operator". In : *IEEE Journal of Solid-State Circuits* 23.2 (1988), p. 358-367. doi : 10.1109/4.996 (cf. p. 30).

[102] Shou-Ming Hou et al. "A review of the edge detection technology". In : *Sparklinglight Transactions on Artificial Intelligence and Quantum Computing (STAIQC)* 1.2 (2021), p. 26-37 (cf. p. 30).

[103] Zhiding Yu et al. "Casenet: Deep category-aware semantic edge detection". In : *Proceedings of the IEEE conference on computer vision and pattern recognition*. 2017, p. 5964-5973 (cf. p. 30).

[104] Sun-Chong Wang et Sun-Chong Wang. "Artificial neural network". In : *Interdisciplinary computing in java programming* (2003), p. 81-100 (cf. p. 31).

[105] Lior Rokach et Oded Maimon. "Decision trees". In : *Data mining and knowledge discovery handbook* (2005), p. 165-192 (cf. p. 31).

[106] Alessia Mammone, Marco Turchi et Nello Cristianini. “Support vector machines”. In : *Wiley Interdisciplinary Reviews: Computational Statistics* 1.3 (2009), p. 283-289 (cf. p. 31).

[107] Steven J Rigatti. “Random forest”. In : *Journal of Insurance Medicine* 47.1 (2017), p. 31-39 (cf. p. 31).

[108] Kristina P Sinaga et Miin-Shen Yang. “Unsupervised K-means clustering algorithm”. In : *IEEE access* 8 (2020), p. 80716-80727 (cf. p. 32).

[109] Rui Xu et Donald Wunsch. “Survey of clustering algorithms”. In : *IEEE Transactions on neural networks* 16.3 (2005), p. 645-678 (cf. p. 32).

[110] Hervé Abdi et Lynne J Williams. “Principal component analysis”. In : *Wiley interdisciplinary reviews: computational statistics* 2.4 (2010), p. 433-459 (cf. p. 32).

[111] Yehuda Koren, Robert Bell et Chris Volinsky. “Matrix factorization techniques for recommender systems”. In : *Computer* 42.8 (2009), p. 30-37 (cf. p. 32).

[112] Jiuxiang Gu et al. “Recent advances in convolutional neural networks”. In : *Pattern recognition* 77 (2018), p. 354-377 (cf. p. 32).

[113] Haibo Wang et al. “Mitosis detection in breast cancer pathology images by combining handcrafted and convolutional neural network features”. In : *Journal of Medical Imaging* 1 (déc. 2014), p. 1-8. doi : 10.1117/1.JMI.1.3.034003 (cf. p. 33).

[114] Adnan Rafique et al. “CNN Based Multi-Object Segmentation and Feature Fusion for Scene Recognition”. In : *Computers, Materials and Continua* 73 (juill. 2022). doi : 10.32604/cmc.2022.027720 (cf. p. 33).

[115] Hanbin Zhang et al. “Deepvoice: A voiceprint-based mobile health framework for parkinson’s disease identification”. In : *2018 IEEE EMBS International Conference on Biomedical & Health Informatics (BHI)*. IEEE. 2018, p. 214-217 (cf. p. 33).

[116] Hojjat Salehinejad et al. “Recent advances in recurrent neural networks”. In : *arXiv preprint arXiv:1801.01078* (2017) (cf. p. 33).

[117] Andreas Triantafyllidis et al. “Deep learning in mHealth for cardiovascular disease, diabetes, and cancer: systematic review”. In : *JMIR mHealth and uHealth* 10.4 (2022), e32344 (cf. p. 33).

[118] Sepp Hochreiter. “The vanishing gradient problem during learning recurrent neural nets and problem solutions”. In : *International Journal of Uncertainty, Fuzziness and Knowledge-Based Systems* 6.02 (1998), p. 107-116 (cf. p. 33).

[119] Sepp Hochreiter et Jürgen Schmidhuber. “Long Short-term Memory”. In : *Neural computation* 9 (déc. 1997), p. 1735-80. doi : 10.1162/neco.1997.9.8.1735 (cf. p. 34).

[120] Rahul Dey et Fathi M. Salem. “Gate-variants of Gated Recurrent Unit (GRU) neural networks”. In : *2017 IEEE 60th International Midwest Symposium on Circuits and Systems (MWSCAS)*. 2017, p. 1597-1600. doi : 10.1109/MWSCAS.2017.8053243 (cf. p. 34).

[121] Anand Chandrasekhar et al. “Smartphone-based blood pressure monitoring via the oscillometric finger-pressing method”. In : *Science Translational Medicine* 10.431 (2018), eaap8674. doi : 10.1126/scitranslmed.aap8674. eprint : https://www.science.org/doi/pdf/10.1126/scitranslmed.aap8674. url : https://www.science.org/doi/abs/10.1126/scitranslmed.aap8674 (cf. p. 35).

[122] Peyman Azad-Khaneghah et al. “Mobile health app usability and quality rating scales: a systematic review”. In : *Disability and Rehabilitation: Assistive Technology* 16.7 (2021). PMID: 31910687, p. 712-721. doi : 10.1080/17483107.2019.1701103. eprint : https://doi.org/10.1080/17483107.2019.1701103. url : https://doi.org/10.1080/17483107.2019.1701103 (cf. p. 35).

[123] Belén Zapata et al. “Empirical Studies on Usability of mHealth Apps: A Systematic Literature Review”. In : *Journal of medical systems* 39 (fév. 2015), p. 182. doi : 10.1007/s10916-014-0182-2 (cf. p. 35).

[124] Martin J Tobin, Franco Laghi et Amal Jubran. “Why COVID-19 Silent Hypoxemia Is Baffling to Physicians”. In : *American journal of respiratory and critical care medicine* 202.3 (août 2020), p. 356-360 (cf. p. 42).

[125] K. Matthes. “Untersuchungen über die Sauerstoffsättigung des menschlichen Arterienblutes”. In : *Naunyn-Schmiedebergs Archiv für experimentelle Pathologie und Pharmakologie* 179 (2005), p. 698-711 (cf. p. 42, 44).

[126] Mark van Gastel, Sander Stuijk et Gerard Haan. “New principle for measuring arterial blood oxygenation, enabling motion-robust remote monitoring”. In : *Scientific Reports* 6 (déc. 2016), p. 38609. doi : 10.1038/srep38609 (cf. p. 42).

[127] J. Severinghaus et Y. Honda. “History of blood gas analysis. VII. Pulse oximetry”. In : *Journal of Clinical Monitoring* 3 (2004), p. 135-138 (cf. p. 42, 44).

[128] CMS-50E OLED Fingertip Pulse Oximeter. *https://www.pulseoximeter.org/cms50e.html*. 2021. url : https://www.pulseoximeter.org/cms50e.html (visité le 03/06/2021) (cf. p. 42, 44, 47, 55).

[129] PM10N 2021 Nellcor™ Portable SpO Patient Monitoring System. *https://www.medtronic.com/covidien/en-us/products/pulse-oximetry/nellcor-portable-spo2-patient-monitoring-system.html*. 2021. url : https://www.medtronic.com/covidien/en-us/products/pulse-oximetry/nellcor-portable-spo2-patient-monitoring-system.html (visité le 03/06/2021) (cf. p. 42, 44).

[130] Pronto Pulse CO-Oximeter. *https://www.masimo.com/products/monitors/spot-check/pronto/*. 2021. url : https://www.masimo.com/products/monitors/spot-check/pronto/ (visité le 03/06/2021) (cf. p. 42, 44).

[131] Jeffrey Haynes. “The ear as an alternative site for a pulse oximeter finger clip sensor”. In : *Respiratory care* 52 (juill. 2007), p. 727-9 (cf. p. 42, 44).

[132] Geeta Agashe, Joseph Coakley et Paul Mannheimer. “Forehead Pulse Oximetry: Headband Use Helps Alleviate False Low Readings Likely Related to Venous Pulsation Artifact”. In : *Anesthesiology* 105 (jan. 2007), p. 1111-6. doi : 10.1097/00000542-200612000-00010 (cf. p. 42, 44).

[133] Tamara Vagg, Barry J. Plant et Sabin Tabirca. “A General MHealth Design Pipeline”. In : *ACM MoMM'16*. Singapore, 2016, 190–194 (cf. p. 42).

[134] Nico Bruining, Enrico Caiani et al. “Acquisition and analysis of cardiovascular signals on smartphones: potential, pitfalls and perspectives: By the Task Force of the e-Cardiology Working Group of European Society of Cardiology”. In : *European Journal of Preventive Cardiology* (2014) (cf. p. 42, 44).

[135] Takahiro Hashizume, Takuya Arizono et Koji Yatani. “Auth ‘n’ Scan: Opportunistic Photoplethysmography in Mobile Fingerprint Authentication”. In : *ACM IMWUT* (2018). doi : 10.1145/3161189 (cf. p. 42, 44).

[136] Sinh Huynh, Rajesh Krishna Balan et al. “VitaMon: Measuring Heart Rate Variability Using Smartphone Front Camera”. In : *ACM SenSys'19*. 2019. doi : 10.1145/3356250.3360036 (cf. p. 42, 44).

[137] Christopher Scully et al. “Physiological Parameter Monitoring from Optical Recordings With a Mobile Phone”. In : *IEEE transactions on bio-medical engineering* 59 (juill. 2011), p. 303-6. doi : 10.1109/TBME.2011.2163157 (cf. p. 42-46, 48, 49, 51, 56).

[138] Nam Bui et al. “PhO2: Smartphone Based Blood Oxygen Level Measurement Systems Using Near-IR and RED Wave-Guided Light”. In : *Proceedings of the 15th ACM Conference on Embedded Network Sensor Systems*. SenSys '17. New York, NY, USA : Association for Computing Machinery, 2017. isbn : 9781450354592. doi : 10.1145/3131672.3131696. url : https://doi.org/10.1145/3131672.3131696 (cf. p. 42, 44, 46, 48, 56, 58).

[139] Domenico Carnì et al. “Setting-up of PPG scaling factors for SpO2% evaluation by smartphone”. In : mai 2016, p. 1-5. doi : 10.1109/MeMeA.2016.7533775 (cf. p. 42-44, 46, 48, 56).

[140] Francesco Lamonaca et al. “Blood oxygen saturation measurement by smartphone camera”. In : *2015 IEEE International Symposium on Medical Measurements and Applications, MeMeA 2015 - Proceedings* (juin 2015), p. 359-364. doi : 10.1109/MeMeA.2015.7145228 (cf. p. 42-44, 48, 56).

[141] Huawei watch GT 2e. *https://consumer.huawei.com/fr/wearables/watch-gt-2e/buy/*. 2020. url : https://consumer.huawei.com/fr/wearables/watch-gt-2e/buy/ (visité le 03/06/2021) (cf. p. 42, 44).

[142] Galaxy Note 4. *https://www.samsung.com/fr/smartphones/galaxy-note/galaxy-note-4-black-32gb-sm-n910fzkexef/*. 2014. url : https://www.samsung.com/fr/smartphones/galaxy-note/galaxy-note-4-black-32gb-sm-n910fzkexef/ (visité le 03/06/2021) (cf. p. 42, 44).

[143] Andrea Němcová et al. “Monitoring of heart rate, blood oxygen saturation, and blood pressure using a smartphone”. In : *Biomedical Signal Processing and Control* 59 (mai 2020), p. 101928. DOI : 10.1016/j.bspc.2020.101928 (cf. p. 43, 48, 56).

[144] Xinyi Ding, Damoun Nassehi et Eric Larson. “Measuring Oxygen Saturation With Smartphone Cameras Using Convolutional Neural Networks”. In : *IEEE Journal of Biomedical and Health Informatics* PP (déc. 2018), p. 1-1. DOI : 10.1109/JBHI.2018.2887209 (cf. p. 43, 44, 46, 48, 49, 56).

[145] Nonin. *NONIN 8000Q2 EAR CLIP SENSOR 3 FOOT/1 METER*. 2021. URL : https://www.turnermedical.com/NONIN_8000Q2_p/nonin_8000q2.htm (visité le 03/06/2021) (cf. p. 44).

[146] John Berkenbosch et Joseph Tobias. “Comparison of a new forehead reflectance pulse oximeter sensor with a conventional digit sensor in pediatric patients”. In : *Respiratory care* 51 (août 2006), p. 726-31 (cf. p. 44).

[147] Marco Fernandez et al. “Evaluation of a New Pulse Oximeter Sensor”. In : *American journal of critical care : an official publication, American Association of Critical-Care Nurses* 16 (avr. 2007), p. 146-52. DOI : 10.4037/ajcc2007.16.2.146 (cf. p. 44).

[148] J Brimacombe, C Keller et J Margreiter. “A Pilot Study of Left Tracheal Pulse Oximetry”. In : *Anesthesia and analgesia* 91 (nov. 2000), p. 1003-6. DOI : 10.1097/00000539-200010000-00043 (cf. p. 44).

[149] Cheng-Yang Huang et al. “Novel Wearable and Wireless Ring-Type Pulse Oximeter with Multi-Detectors”. In : *Sensors (Basel, Switzerland)* 14 (sept. 2014), p. 17586-17599. DOI : 10.3390/s140917586 (cf. p. 44).

[150] Samsung. *Samsung Galaxy Watch3*. 2020. URL : https://www.samsung.com/fr/watches/galaxy-watch/galaxy-watch3-41mm-mystic-bronze-sm-r850nzdaeub/buy/ (visité le 03/06/2021) (cf. p. 44).

[151] Apple Watch Serie 6. *https://www.apple.com/fr/apple-watch-series-6/*. 2020. URL : https://www.apple.com/fr/apple-watch-series-6/ (visité le 03/06/2021) (cf. p. 44).

[152] Samsung Galaxy S7 | S7 edge. *https://www.samsung.com/fr/smartphones/galaxy-s7/overview/*. 2016. URL : https://www.samsung.com/fr/smartphones/galaxy-s7/overview/ (visité le 03/06/2021) (cf. p. 44).

[153] Samsung Galaxy S6 | S6 edge. *https://www.samsung.com/fr/smartphones/galaxy-s6/s6/*. 2015. URL : https://www.samsung.com/fr/smartphones/galaxy-s6/s6/ (visité le 03/06/2021) (cf. p. 44).

[154] Nam Bui et al. “Smartphone-Based SpO2 Measurement by Exploiting Wavelengths Separation and Chromophore Compensation”. In : *ACM Transactions on Sensor Networks (TOSN)* 16 (2020), p. 1 -30 (cf. p. 44).

[155] Yitzhak Mendelson. “Pulse oximetry: theory and applications for noninvasive monitoring.” In : *Clinical chemistry* 38 9 (1992), p. 1601-7 (cf. p. 45).

[156] Reham Mohamed et Moustafa Youssef. “HeartSense: Ubiquitous Accurate Multi-Modal Fusion-Based Heart Rate Estimation Using Smartphones”. In : *Proc. ACM Interact. Mob. Wearable Ubiquitous Technol.* 1.3 (sept. 2017). doi : 10.1145/3132028. url : https://doi.org/10.1145/3132028 (cf. p. 48).

[157] Ufuk Bal. “Non-contact estimation of heart rate and oxygen saturation using ambient light”. In : *Biomedical optics express* 6 (fév. 2015), p. 86-97. doi : 10.1364/BOE.6.000086 (cf. p. 51).

[158] J. Max. “Quantizing for minimum distortion”. In : *IRE Transactions on Information Theory* 6.1 (1960), p. 7-12. doi : 10.1109/TIT.1960.1057548 (cf. p. 52).

[159] David L. Davies et Donald W. Bouldin. “A Cluster Separation Measure”. In : *IEEE Transactions on Pattern Analysis and Machine Intelligence* PAMI-1.2 (1979), p. 224-227. doi : 10.1109/TPAMI.1979.4766909 (cf. p. 53).

[160] N. Kaoungku et al. “The silhouette width criterion for clustering and association mining to select image features”. In : *International Journal of Machine Learning and Computing* 8 (fév. 2018), p. 69-73. doi : 10.18178/ijmlc.2018.8.1.665 (cf. p. 53, 54).

[161] Bernd Porr. *An IIR filter library written in JAVA*. 2016. url : https://www.berndporr.me.uk/iir/site/ (visité le 28/05/2021) (cf. p. 54).

[162] Helsinki Declaration. *Ethical principles for medical research involving human subjects*. 2013 (cf. p. 55, 77).

[163] R Krzyminiewski et al. “High Signal Resolution Pulse Wave–Hope for a Fast and Cheap Home Care Monitoring Patients with Cardiac Diseases”. In : *Mede-Tel Conference Proceedings*. 2011, p. 252-56 (cf. p. 55).

[164] Takahiro Hashizume, Takuya Arizono et Koji Yatani. “Auth ‘N’ Scan: Opportunistic Photoplethysmography in Mobile Fingerprint Authentication”. In : *Proc. ACM Interact. Mob. Wearable Ubiquitous Technol.* 1.4 (jan. 2018). doi : 10.1145/3161189. url : https://doi.org/10.1145/3161189 (cf. p. 55).

[165] Michael W. Sjoding et al. “Racial Bias in Pulse Oximetry Measurement”. In : *New England Journal of Medicine* 383.25 (2020). PMID: 33326721, p. 2477-2478. doi : 10.1056/NEJMc2029240. eprint : https://doi.org/10.1056/NEJMc2029240. url : https://doi.org/10.1056/NEJMc2029240 (cf. p. 56).

[166] T. Fitzpatrick. “The validity and practicality of sun-reactive skin types I through VI.” In : *Archives of dermatology* 124 6 (1988), p. 869-71 (cf. p. 56).

[167] Lomaliza Kombozi et Hanhoon Park. “A highly efficient and reliable heart rate monitoring system using smartphone cameras”. In : *Multimedia Tools and Applications* 76 (oct. 2017). doi : 10.1007/s11042-016-4010-1 (cf. p. 57).

[168] A. Developers. *Measure app performance with android profiler. Google.* 2022. URL : Available : https : / / developer . android . com / studio / profile/cpu-profiler (cf. p. 60, 79).

[169] Luke Howard et al. "Chamber for controlling end-tidal gas tensions over sustained periods in humans". In : *Journal of applied physiology (Bethesda, Md. : 1985)* 78 (avr. 1995), p. 1088-91. DOI : 10.1152/jappl.1995.78.3.1088 (cf. p. 61).

[170] Alessandro Guazzi et al. "Non-contact measurement of oxygen saturation with an RGB camera". In : *Biomedical optics express* 6 (sept. 2015), p. 3320-38. DOI : 10.1364/BOE.6.003320 (cf. p. 61).

[171] Frédéric Bousefsaf et al. "iPPG2cPPG: Reconstructing contact from imaging photoplethysmographic signals using U-Net architectures". In : *Computers in Biology and Medicine* 138 (2021), p. 104860. ISSN : 0010-4825. DOI : https : / / doi . org / 10 . 1016 / j . compbiomed . 2021 . 104860. URL : https://www.sciencedirect.com/science/article/pii/S0010482521006545 (cf. p. 61).

[172] Katayoun Bahadori et al. *Economic burden of asthma: a systematic review.* 2009. DOI : http://dx.doi.org/10.14288/1.0223779. URL : http://dx.doi.org/10.14288/1.0223779 (cf. p. 62).

[173] World Health Organization. *The top 10 causes of death.* 2020. URL : Available : https : / / www . who . int / news - room / fact - sheets / detail / the - top - 10 - causes - of - death (visité le 02/01/2022) (cf. p. 62).

[174] Vestbo et al. "Global strategy for the diagnosis, management, and prevention of chronic obstructive pulmonary disease: GOLD executive summary." eng. In : *Am J Respir Crit Care Med* 187.4 (2013), p. 347-365. ISSN : 1535-4970 (Electronic); 1073-449X (Linking). DOI : 10.1164/rccm.201204-0596PP (cf. p. 62).

[175] Michael Mcgeachie et al. "Patterns of Growth and Decline in Lung Function in Persistent Childhood Asthma". In : *The New England journal of medicine* 374 (mai 2016), p. 1842-1852. DOI : 10.1056/NEJMoa1513737 (cf. p. 62).

[176] Robert Langan et Andrew Goodbred. "Office Spirometry: Indications and Interpretation". In : *American family physician* 101 (mars 2020), p. 362-368 (cf. p. 62, 66).

[177] Martin R Miller et al. "Standardisation of spirometry". In : *European respiratory journal* 26.2 (2005), p. 319-338 (cf. p. 62, 66).

[178] Gray D Masekela R Zurba L. "Dealing with Access to Spirometry in Africa: A Commentary on Challenges and Solutions." In : *International Journal of Environmental Research and Public Health* (2018), p. 16-62 (cf. p. 62).

[179] C.H. Richardson et al. “Initiating home spirometry for children during the COVID-19 pandemic – A practical guide”. In : *Paediatric Respiratory Reviews* 42 (2022), p. 43-48. ISSN : 1526-0542. DOI : https://doi.org/10.1016/j.prrv.2021.02.001. URL : https://www.sciencedirect.com/science/article/pii/S152605422100004X (cf. p. 63).

[180] Siddharth Gupta et al. “MobileSpiro: Accurate Mobile Spirometry for Self-Management of Asthma”. In : *Proceedings of the First ACM Workshop on Mobile Systems, Applications, and Services for Healthcare*. mHealthSys ’11. Seattle, Washington : Association for Computing Machinery, 2011. ISBN : 9781450306843. DOI : 10.1145/2064942.2064944. URL : https://doi.org/10.1145/2064942.2064944 (cf. p. 63, 66).

[181] Mayank Goel et al. “SpiroCall: Measuring Lung Function over a Phone Call”. In : *Proceedings of the 2016 CHI Conference on Human Factors in Computing Systems* (2016) (cf. p. 63, 67).

[182] Md. Mahbubur Rahman et al. “ExhaleSense: Detecting High Fidelity Forced Exhalations to Estimate Lung Obstruction on Smartphones”. In : *2020 IEEE International Conference on Pervasive Computing and Communications (PerCom)* (2020), p. 1-10 (cf. p. 63, 67, 73, 78).

[183] Mohsin Y. Ahmed, Md. Mahbubur Rahman et Jilong Kuang. “DeepLung: Smartphone Convolutional Neural Network-Based Inference of Lung Anomalies for Pulmonary Patients”. In : *Interspeech 2019, 20th Annual Conference of the International Speech Communication Association, Graz, Austria, 15-19 September 2019*. ISCA, 2019, p. 2335-2339. DOI : 10.21437/Interspeech.2019-2953. URL : https://doi.org/10.21437/Interspeech.2019-2953 (cf. p. 63, 67).

[184] Jan W. Gooch. « Boyle’s Law ». In : *Encyclopedic Dictionary of Polymers*. Sous la dir. de Jan W. Gooch. New York, NY : Springer New York, 2011, p. 92-92. ISBN : 978-1-4419-6247-8. DOI : 10.1007/978-1-4419-6247-8_1540 (cf. p. 64, 71).

[185] Graham BL et al. “Standardization of Spirometry 2019 Update. An Official American Thoracic Society and European Respiratory Society Technical Statement.” In : *American Journal of Respiratory and Critical Care Medicine* 166 (oct. 2019), p. 571-579. DOI : 10.1164/rccm.201908-1590ST (cf. p. 66, 72, 73, 75).

[186] Jeremy D Johnson et Wesley M Theurer. “A stepwise approach to the interpretation of pulmonary function tests.” In : *American family physician* 89 5 (2014), p. 359-66 (cf. p. 66).

[187] PMA Calverley. “The clinical usefulness of spirometric information”. In : *Breathe* 5.3 (2009), p. 214-220 (cf. p. 66).

[188] Philip H Quanjer et al. *Multi-ethnic reference values for spirometry for the 3–95-yr age range: the global lung function 2012 equations*. 2012 (cf. p. 66).

[189] William D. Carey. “Current Clinical Medicine”. 2e éd. Cleveland Clinic : Saunders, 2010 (cf. p. 66).

[190] Nazir Saleheen et al. “Lung Function Estimation from a Monosyllabic Voice Segment Captured Using Smartphones”. In : *22nd International Conference on Human-Computer Interaction with Mobile Devices and Services*. MobileHCI ’20. Oldenburg, Germany : Association for Computing Machinery, 2020. isbn : 9781450375160. doi : 10.1145/3379503.3403543. url : https://doi.org/10.1145/3379503.3403543 (cf. p. 67).

[191] Alex Mariakakis et al. “Challenges in Realizing Smartphone-Based Health Sensing”. In : *IEEE Pervasive Computing* 18.2 (2019), 76–84. issn : 1536-1268. doi : 10.1109/MPRV.2019.2907007. url : https://doi.org/10.1109/MPRV.2019.2907007 (cf. p. 67).

[192] D. R. Merritt et F. Weinhaus. “The pressure curve for a rubber balloon”. In : *American Journal of Physics* 46.10 (1978), p. 976-977. doi : 10.1119/1.11486. eprint : https://doi.org/10.1119/1.11486. url : https://doi.org/10.1119/1.11486 (cf. p. 69).

[193] Shuolun Wang et Shawn A. Chester. “Experimental characterization and continuum modeling of inelasticity in filled rubber-like materials”. In : *International Journal of Solids and Structures* 136-137 (2018), p. 125-136. issn : 0020-7683. doi : https://doi.org/10.1016/j.ijsolstr.2017.12.010. url : https://www.sciencedirect.com/science/article/pii/S0020768317305474 (cf. p. 70).

[194] Julie Diani, Bruno Fayolle et Pierre Gilormini. “A review on the Mullins effect”. In : *European Polymer Journal* 45.3 (2009), p. 601-612. issn : 0014-3057. doi : https://doi.org/10.1016/j.eurpolymj.2008.11.017. url : https://www.sciencedirect.com/science/article/pii/S0014305708006332 (cf. p. 70).

[195] Cureos AB Anders Gustafsson. *Constrained Optimization BY Linear Approximation in Java*. 2012. url : Available:https://github.com/cureos/jcobyla (cf. p. 77).

[196] M. J. D. Powell. “A View of Algorithms for Optimization without Derivatives 1”. In : 2007 (cf. p. 77).

[197] M. J. D. Powell. “An efficient method for finding the minimum of a function of several variables without calculating derivatives”. In : *The Computer Journal* 7.2 (jan. 1964), p. 155-162. issn : 0010-4620. doi : 10.1093/comjnl/7.2.155. eprint : https://academic.oup.com/comjnl/article-pdf/7/2/155/959784/070155.pdf. url : https://doi.org/10.1093/comjnl/7.2.155 (cf. p. 77).

[198] CONTEC. *SP10 Pulmonary Function Lung*. 2019. url : https://contechealth.com/products/sp10-spirometer (cf. p. 77).

[199] David Rebuck et al. “The Accuracy of a Handheld Portable Spirometer”. In : *Chest* 109 (fév. 1996), p. 152-7. doi : 10.1378/chest.109.1.152 (cf. p. 77).

[200] J. Martin Bland et DouglasG. Altman. “STATISTICAL METHODS FOR ASSESSING AGREEMENT BETWEEN TWO METHODS OF CLINICAL MEASUREMENT”. In : *The Lancet* 327.8476 (1986). Originally published as Volume 1, Issue 8476, p. 307-310. issn : 0140-6736. doi : https://doi.org/10.1016/S0140-6736(86)90837-8. url : https://www.sciencedirect.com/science/article/pii/S0140673686908378 (cf. p. 78).

[201] David Hutchinson et Ken Whyte. “Neuromuscular disease and respiratory failure”. In : *Practical neurology* 8.4 (2008), p. 229-237 (cf. p. 81).

[202] Tauhidur Rahman et al. “Nutrilyzer: A Mobile System for Characterizing Liquid Food with Photoacoustic Effect”. In : *Proceedings of the 14th ACM Conference on Embedded Network Sensor Systems CD-ROM*. SenSys ’16. Stanford, CA, USA : Association for Computing Machinery, 2016, 123–136. isbn : 9781450342636. doi : 10.1145/2994551.2994572. url : https://doi.org/10.1145/2994551.2994572 (cf. p. 82).

[203] Unsoo Ha et al. “Learning Food Quality and Safety from Wireless Stickers”. In : *Proceedings of the 17th ACM Workshop on Hot Topics in Networks*. HotNets ’18. Redmond, WA, USA : Association for Computing Machinery, 2018, 106–112. isbn : 9781450361200. doi : 10.1145/3286062.3286078. url : https://doi.org/10.1145/3286062.3286078 (cf. p. 82, 104).

[204] Qianyi Huang, Zhice Yang et Qian Zhang. “Smart-U: Smart Utensils Know What You Eat”. In : *IEEE INFOCOM 2018 - IEEE Conference on Computer Communications*. Honolulu, HI, USA : IEEE Press, 2018, 1439–1447. doi : 10.1109/INFOCOM.2018.8486266. url : https://doi.org/10.1109/INFOCOM.2018.8486266 (cf. p. 82).

[205] Ju Wang et al. “TagScan: Simultaneous Target Imaging and Material Identification with Commodity RFID Devices”. In : MobiCom ’17. Snowbird, Utah, USA : Association for Computing Machinery, 2017, 288–300. isbn : 9781450349161. doi : 10.1145/3117811.3117830. url : https://doi.org/10.1145/3117811.3117830 (cf. p. 82).

[206] Ashutosh Dhekne et al. “LiquID: A wireless liquid identifier”. English (US). In : *MobiSys 2018 - Proceedings of the 16th ACM International Conference on Mobile Systems, Applications, and Services*. MobiSys 2018 - Proceedings of the 16th ACM International Conference on Mobile Systems, Applications, and Services. Association for Computing Machinery, Inc, juin 2018, p. 442-454. doi : 10.1145/3210240.3210345 (cf. p. 82).

[207] Tauhidur Rahman et al. “Nutrilyzer: A Mobile System for Characterizing Liquid Food with Photoacoustic Effect”. In : *Proceedings of the 14th ACM Conference on Embedded Network Sensor Systems CD-ROM* (2016) (cf. p. 82).

[208] Tyler Lee. *Samsung Could Drop LiDAR Sensor In Future Smartphones*. URL : https://www.ubergizmo.com/2021/04/samsung-no-more-lidar-future-phones/ (visité le 07/02/2023) (cf. p. 83, 105).

[209] D. E. Sullivan. "Surface tension and contact angle of a liquid–solid interface". In : *The Journal of Chemical Physics* 74.4 (fév. 1981), p. 2604-2615. ISSN : 0021-9606. DOI : 10.1063/1.441333. eprint : https://pubs.aip.org/aip/jcp/article-pdf/74/4/2604/11250573/2604_1_online.pdf. URL : https://doi.org/10.1063/1.441333 (cf. p. 83, 86).

[210] Yuehua Yuan et T. Randall Lee. « Contact Angle and Wetting Properties ». In : *Surface Science Techniques*. Sous la dir. de Gianangelo Bracco et Bodil Holst. Berlin, Heidelberg : Springer Berlin Heidelberg, 2013, p. 3-34. ISBN : 978-3-642-34243-1. DOI : 10.1007/978-3-642-34243-1_1. URL : https://doi.org/10.1007/978-3-642-34243-1_1 (cf. p. 83, 86).

[211] H. Chen, Jesus L. Muros-Cobos et A. Amirfazli. "Contact angle measurement with a smartphone". In : *Review of Scientific Instruments* 89.3 (2018), p. 035117. DOI : 10.1063/1.5022370. eprint : https://doi.org/10.1063/1.5022370. URL : https://doi.org/10.1063/1.5022370 (cf. p. 84, 89, 92, 93, 106).

[212] S. Farshid Chini et A. Amirfazli. "A method for measuring contact angle of asymmetric and symmetric drops". In : *Colloids and Surfaces A: Physicochemical and Engineering Aspects* 388.1 (2011), p. 29-37. ISSN : 0927-7757. DOI : https://doi.org/10.1016/j.colsurfa.2011.08.001. URL : https://www.sciencedirect.com/science/article/pii/S0927775711004857 (cf. p. 84, 92, 106).

[213] Feredoon Behroozi et Peter Behroozi. "Reliable determination of contact angle from the height and volume of sessile drops". In : *American Journal of Physics* (2018) (cf. p. 84, 89, 92, 106).

[214] Michael Julian Orella et al. "High-throughput analysis of contact angle goniometry data using DropPy". In : *SoftwareX* 14 (2021), p. 100665. ISSN : 2352-7110. DOI : https://doi.org/10.1016/j.softx.2021.100665. URL : https://www.sciencedirect.com/science/article/pii/S2352711021000108 (cf. p. 84, 88, 89, 92, 106).

[215] Hao Tang et Xianhua Cheng. "Measurement of liquid surface tension by fitting the lying droplet profile". In : *Measurement* 188 (oct. 2021), p. 110379. DOI : 10.1016/j.measurement.2021.110379 (cf. p. 84, 89, 92, 106).

[216] Darren Williams et al. "Contact Angle Measurements Using Cellphone Cameras to Implement the Bikerman Method". In : *Galvanotechnik* 102 (août 2011), p. 1718-1725 (cf. p. 84, 92).

[217] Stéphane Champmartin, A. Ambari et Jean Yves Le Pommellec. "New procedure to measure simultaneously the surface tension and contact angle". In : *Review of Scientific Instruments* 87 (avr. 2016) (cf. p. 84, 89, 92, 106).

[218] Nis Korsgaard Andersen et Rafael Taboryski. “Drop shape analysis for determination of dynamic contact angles by double sided elliptical fitting method”. In : *Measurement Science and Technology* 28.4 (2017), p. 047003. doi : 10.1088/1361-6501/aa5dcf. url : https://dx.doi.org/10.1088/1361-6501/aa5dcf (cf. p. 84, 92, 106).

[219] Francis Bashforth et John Couch Adams. “An attempt to test the theories of capillary action by comparing the theoretical and measured forms of drops of fluid”. University Press, 1883 (cf. p. 84).

[220] Martin A. Fischler et Robert C. Bolles. “Random Sample Consensus: A Paradigm for Model Fitting with Applications to Image Analysis and Automated Cartography”. In : *Commun. ACM* 24.6 (1981), 381–395. issn : 0001-0782. doi : 10.1145/358669.358692. url : https://doi.org/10.1145/358669.358692 (cf. p. 84, 97).

[221] Carel Jan van Oss. « Chapter Two - The Apolar and Polar Properties of Liquid Water and Other Condensed-Phase Materials ». In : *The Properties of Water and their Role in Colloidal and Biological Systems*. Sous la dir. de Carel J. van Oss. T. 16. Interface Science and Technology. Elsevier, 2008, p. 13-30. doi : https://doi.org/10.1016/S1573-4285(08)00202-0. url : https://www.sciencedirect.com/science/article/pii/S1573428508002020 (cf. p. 86).

[222] Jean Berthier. « Chapter 3 - The Physics of Droplets**This chapter was written with the collaboration of Kenneth A. Brakke (Mathematics Department, Susquehanna University, Selinsgrove, PA). » In : *Micro-Drops and Digital Microfluidics (Second Edition)*. Sous la dir. de Jean Berthier. Second Edition. Micro and Nano Technologies. William Andrew Publishing, 2013, p. 75-160. isbn : 978-1-4557-2550-2. doi : https://doi.org/10.1016/B978-1-4557-2550-2.00003-1. url : https://www.sciencedirect.com/science/article/pii/B9781455725502000031 (cf. p. 86).

[223] G. D. Byrne et A. C. Hindmarsh. “A Polyalgorithm for the Numerical Solution of Ordinary Differential Equations”. In : *ACM Trans. Math. Softw.* 1.1 (1975), 71–96. issn : 0098-3500. doi : 10.1145/355626.355636. url : https://doi.org/10.1145/355626.355636 (cf. p. 88).

[224] D.Y. Kwok et A.W. Neumann. “Contact angle measurement and contact angle interpretation”. In : *Advances in Colloid and Interface Science* 81.3 (1999), p. 167-249. issn : 0001-8686. doi : https://doi.org/10.1016/S0001-8686(98)00087-6. url : https://www.sciencedirect.com/science/article/pii/S0001868698000876 (cf. p. 91).

[225] Jonathan M. Schuster, Carlos E. Schvezov et Mario R. Rosenberger. “Influence of Experimental Variables on the Measure of Contact Angle in Metals Using the Sessile Drop Method”. In : *Procedia Materials Science* 8 (2015). International Congress of Science and Technology of Metallurgy and Materials, SAM - CONAMET 2013, p. 742-751. issn : 2211-8128. doi : https://doi.org/10.1016/

j.mspro.2015.04.131. URL : https://www.sciencedirect.com/science/article/pii/S2211812815001327 (cf. p. 91).

[226] Girish KUMAR et K PRABHU. "Review of non-reactive and reactive wetting of liquids on surfaces". In : *Advances in colloid and interface science* 133 (juill. 2007), p. 61-89. DOI : 10.1016/j.cis.2007.04.009 (cf. p. 91).

[227] C. CANSOY. "The effect of drop size on contact angle measurements of superhydrophobic surfaces". In : *RSC Advances* 4 (jan. 2014), p. 1197. DOI : 10.1039/c3ra45947k (cf. p. 91).

[228] John A. NELDER et Roger MEAD. "A Simplex Method for Function Minimization". In : *Comput. J.* 7 (1965), p. 308-313 (cf. p. 97).

[229] Hadlee SIMONS. *Gorilla Glass vs Dragontrail Glass vs Ceramic Shield and beyond.* 2023. URL : https://www.androidauthority.com/gorilla-glass-comparison-886866/ (visité le 15/02/2023) (cf. p. 102).

[230] Haydn SIMPSON. *Food and beverages: fighting counterfeits worldwide.* 2017. URL : https://www.worldtrademarkreview.com/global-guide/anti-counterfeiting-and-online-brand-enforcement/2017/article/food-and-beverages-fighting-counterfeits-worldwide (visité le 07/02/2023) (cf. p. 102).

[231] Dairy REPORTER. *International food fraud operation nets 320 tonnes of dodgy dairy products.* 2020. URL : https://www.dairyreporter.com/Article/2020/07/22/International-food-fraud-operation-nets-320-tonnes-of-dodgy-dairy-products (visité le 07/02/2023) (cf. p. 102).

[232] NEOGEN. *Food fraud: The adulterated alcohol trend.* 2019. URL : https://www.neogen.com/neocenter/blog/food-fraud-the-adulterated-alcohol-trend/ (visité le 07/02/2023) (cf. p. 102).

[233] Cody COPELAND. *Honey is one of the most faked foods in the world, and the US government isn't doing much to fix it.* 2019. URL : https://www.insider.com/fake-honey-problems-how-it-works-2020-9 (visité le 07/02/2023) (cf. p. 102).

[234] Kelly MCLAUGHLIN. *Dominican Republic officials are reportedly investigating whether counterfeit alcohol caused recent tourist deaths — here's what that is.* 2019. URL : https://www.insider.com/counterfeit-alcohol-what-it-is-2019-6 (visité le 07/02/2023) (cf. p. 102).

[235] C. E. MOGENSEN. "Microalbuminuria Predicts Clinical Proteinuria and Early Mortality in Maturity-Onset Diabetes". In : *New England Journal of Medicine* 310.6 (1984). PMID: 6690964, p. 356-360. DOI : 10.1056/NEJM198402093100605. eprint : https://doi.org/10.1056/NEJM198402093100605. URL : https://doi.org/10.1056/NEJM198402093100605 (cf. p. 104).

[236] G.C. Viberti et al. “MICROALBUMINURIA AS A PREDICTOR OF CLINICAL NEPHROPATHY IN INSULIN-DEPENDENT DIABETES MELLITUS”. In : *The Lancet* 319.8287 (1982). Originally published as Volume 1, Issue 8287, p. 1430-1432. ISSN : 0140-6736. DOI : https://doi.org/10.1016/S0140-6736(82)92450-3. URL : https://www.sciencedirect.com/science/article/pii/S0140673682924503 (cf. p. 104).

[237] Ashutosh Dhekne et al. “LiquID: A Wireless Liquid IDentifier”. In : *Proceedings of the 16th Annual International Conference on Mobile Systems, Applications, and Services* (2018) (cf. p. 104).

[238] Unsoo Ha et al. “Food and Liquid Sensing in Practical Environments Using RFIDs”. In : *Proceedings of the 17th Usenix Conference on Networked Systems Design and Implementation*. NSDI’20. Santa Clara, CA, USA : USENIX Association, 2020, 1083–1100. ISBN : 9781939133137 (cf. p. 104).

[239] Ju Wang et al. “TagScan: Simultaneous Target Imaging and Material Identification with Commodity RFID Devices”. In : *Proceedings of the 23rd Annual International Conference on Mobile Computing and Networking* (2017) (cf. p. 104).

[240] Ju Wang et al. “Simultaneous Material Identification and Target Imaging with Commodity RFID Devices”. In : *IEEE Transactions on Mobile Computing* 20.2 (2021), p. 739-753. DOI : 10.1109/TMC.2019.2946072 (cf. p. 104).

[241] Binbin Xie et al. “Tagtag: material sensing with commodity RFID”. In : *Proceedings of the 17th Conference on Embedded Networked Sensor Systems* (2019) (cf. p. 104).

[242] Hui-Shyong Yeo et al. “RadarCat: Radar Categorization for Input amp; Interaction”. In : *Proceedings of the 29th Annual Symposium on User Interface Software and Technology*. UIST ’16. Tokyo, Japan : Association for Computing Machinery, 2016, 833–841. ISBN : 9781450341899. DOI : 10.1145/2984511.2984515. URL : https://doi.org/10.1145/2984511.2984515 (cf. p. 104).

[243] Diana Zhang et al. “On the Feasibility of Wi-Fi Based Material Sensing”. In : *The 25th Annual International Conference on Mobile Computing and Networking*. MobiCom ’19. Los Cabos, Mexico : Association for Computing Machinery, 2019. ISBN : 9781450361699. DOI : 10.1145/3300061.3345442. URL : https://doi.org/10.1145/3300061.3345442 (cf. p. 104).

[244] Yumeng Liang et al. “FG-LiquID: A Contact-Less Fine-Grained Liquid Identifier by Pushing the Limits of Millimeter-Wave Sensing”. In : *Proc. ACM Interact. Mob. Wearable Ubiquitous Technol.* 5.3 (2021). DOI : 10.1145/3478075. URL : https://doi.org/10.1145/3478075 (cf. p. 104).

[245] Nicolas-Alexandre Goy et al. “Surface tension measurements with a smartphone”. In : *The Physics Teacher* 55 (nov. 2017), p. 498-499. DOI : 10.1119/1.5008349 (cf. p. 105).

[246] Yongzhi Huang et al. “Lili: Liquor Quality Monitoring Based on Light Signals”. In : *Proceedings of the 27th Annual International Conference on Mobile Computing and Networking*. MobiCom ’21. New Orleans, Louisiana : Association for Computing Machinery, 2021, 256–268. isbn : 9781450383424. doi : 10.1145/3447993.3483246. url : https://doi.org/10.1145/3447993.3483246 (cf. p. 105).

[247] Mengxi Wei et al. “The study of liquid surface waves with a smartphone camera and an image recognition algorithm”. In : *European Journal of Physics* 36.6 (2015), p. 065026. doi : 10.1088/0143-0807/36/6/065026. url : https://dx.doi.org/10.1088/0143-0807/36/6/065026 (cf. p. 105).

[248] Emőke Albert et al. “Robust Contact Angle Determination for Needle-in-Drop Type Measurements”. In : *ACS Omega* 2019 (oct. 2019). doi : 10.1021/acsomega.9b02990 (cf. p. 106).